[Preparation of Poly(methyl methacrylate)/Diamond Nanoparticle Composites via ATRP]

[Jong-Kwan Lim]

[Interdisciplinary School of Green Energy]
Graduate School of UNIST

[Preparation of Poly(methyl methacrylate)/Diamond Nanoparticle Composites via ATRP]

A thesis
submitted to the Interdisciplinary School of Green Energy
and the Graduate School of UNIST
in partial fulfillment of the
requirements for the degree of
[Master of Science]

[Jong-Kwan Lim]

05.28.2010
Approved by

Major Advisor
[Jong-Beom, Baek]

[Preparation of Poly(methyl methacrylate)/Diamond Nanoparticle Composites via ATRP]

[Jong-Kwan Lim]

This certifies that the thesis of [Jong-Kwan Lim] is approved.

05.28.2010

[signature]

Thesis supervisor: [Jong-Beom, Baek]

[signature]

[Hyun-Kon, Song]

[signature]

[Byeong-Su, Kim]

Abstract

Functionalization of diamond nanoparticales (DNPs) was conducted with 4-ethylbenzoic acid (EBA) in a less-destructive mild polyphosphoric acid (PPA)/phosphorous pentoxide (P_2O_5) medium to afford 4-ethylbenzoyl-functionalized DNPs (EBA-g-DNP). Subsequently, the bromination of EBA-g-DNP using *N*-bromosuccinimide (NBS) yielded α-brominated EBA-g-DNP (BrEBA-g-DNP), which was used as an initiator for methyl methacrylate (MMA) via atom-transfer radical polymerization (ATRP). Poly(methylmetacrylate) grafted DNP (PMMA-g-DNP)was prepared from the reaction between MMA and BrEBA-g-DNP in the presence of copper(I) bromide in anhydrous *N*-Methyl-2-pyrrolidone (NMP). The resultant PMMA-g-DNP was characterized by using FT-IR, TGA, ^{1}H NMR, SEM, TEM and etc.TEM images provided clearvisual evidence for the formation of a core–shell structure-a hard DNP core and a soft PMMA shell.

ULSAN NATIONAL INSTITUTE OF SCIENCE AND TECHNOLOGY
UNIST

Contents

List of figures

List of table

List of Schemes

Nomenclature

ATRP	atom transfer radical polymerization
CNM	carbon nanomaterial
DNP	diamond nanoparticle
EBA	4-ethylbenzoic acid
PPA	polyphosphoric acid
P_2O_5	phosphorous pentoxide
PMMA	Poly(methylmetha acrylate)
THF	Tetra hydrofuran
NBS	N-bromosuccinmide
NMP	N-methyl-2-pyrrolidone
BPO	Benzoyl peroxide
FT-IR	Fourier-transform Infrared
TGA	Thermogravimetric analysis
BPO	Fourier transform spectroscopy
WAXD	Wide-angle x-ray diffraction
SEM	Scanning electron microscopy
TEM	Transmission electron microscopy
BET	Brunauer-Emmett-Teller
UV	Ultravilolet
XPS	X-ray photoelectron spectroscopy
EA	Elemental analyses

ULSAN NATIONAL INSTITUTE OF SCIENCE AND TECHNOLOGY
UNIST

Ⅰ. Introduction

Since their discovery, carbon nanomaterials (CNMs)[1] have attracted great attention due to their unique chemical and physical properties.[2] Carbon is the most versatile element that can be bonded in many ways to construct new structures, such as graphite, diamond, C_{60} and carbon nanotubes that range from three to zero dimensions at the nanoscale (Figure 1). These materials tend to possess several unique chemical, physical, and electronic properties, making them very attractive for a range of advanced technological applications. For instance, crystalline diamond is an ideal material for high frequency, high temperature, and high power electronics and electrochemical applications.[3] Significant progress has been made to synthesize single-crystal diamond for technological purposes, for large-area device fabrication, single-crystal diamond is still cost-prohibitive. Alternatively, nanocrystalline and the smaller-grained ultrananocrystalline diamond provide a cost-effective means for producing polycrystalline thin films with nanoscale domains that retain many of the desired properties of natural single-crystal diamond. Another allotrope of carbon is graphite, which consists of stacked sheets of hexagonally packed carbon atoms that are sp^2 bonded, while a single sheet, grapheme, is nature's version of an ideal two dimensional conductor. Another advantage of utilizing carbon for nanotechnology is that it naturally forms nanoscale materials that include buckminsterfullerene (C_{60}). Given the many forms of carbon that are technologically relevant, there are certain attributes that seem to be universal, such as high mechanical strength, good thermal conductivity and stability, chemical inertness, and high carrier mobilities.

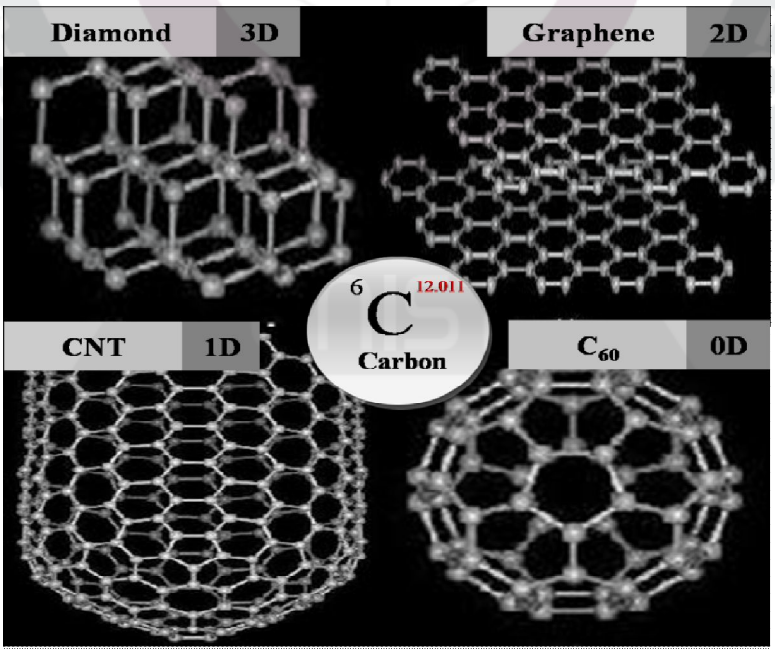

Figure 1. This schematic diagram shows the different allotropes of carbon.

However, two issues have to be resolved first to achieve maximum enhanced properties emerging from nanoscale additives. The one is homogeneous dispersion of CNMs, which is a factor in percolation threshold.[4] The other is interfacial adhesion between reinforcing additive and supporting matrix.[5] Thus, there have been many efforts to afford homogeneous dispersion of CNMs into various matrices via physical,[6] chemical,[7] or combined approaches.[8] However, physical method using sonication damages CNMs depending upon dose time and strength.[9] Because of chemical inertness of CNMs, the chemical modification of CNMs requires harsh reaction condition in strong acids such as nitric acid and sulfuric acid and/or their mixtures at elevated temperatures. These methods cause significant damages to the molecular structure of CNMs. The physical properties of nanocomposites significantly depend on the strength of specific interfacial interactions. Otherwise, the fillers play as defects where stress concentration points. Hence, strong covalent and/or noncovalent interactions between CNMs and matrix in nanocomposite are necessary to efficiently transfer the outstanding properties of CNMs to the supporting polymer matrix. Among CNMs, in particular, Diamond, the king of all gemstones, is acknowledged as an excellent material for almost all the industrial fields including electronic[10] and chemical industry. It has extreme properties in hardness, optical transparency, thermal expansion, thermal conductivity, electrical insulation, chemical corrosiveness, least friction coefficient[11] and biocompatibility.[12] Diamond powder manufacuring and CVD technology have been developed to utilize such properties of diamond effectively and micron-sized diamond powders are being used for various industrial purposes. Recent development in nanotechnology makes it possible to produce nano-sized diamond powders, expanding the realm of diamond industry. There are number of methods in manufacturing nanodiamond, which includes HPHT[13], shock wave, CVD[14], and detonation[15]. Nanodiamond of below 10 nm in radius is specifically called ultrananocrystalline diamond (UNCD). UNCD in size of around 5 nm, is manufactured through detonation method which was originally developed during the former Soviet Union's military research for rocket fuels. Nanodiamond of 10-100 nm in radius is first broken down by shock wave or HPHT (High Pressure/High Temperature) method, and consequently broken down with machineries. Nanodiamond is unique in its shape and structure. It not only retains diamond structure and hardness but also has circular shape and highly active surface, providing outstanding lubricating properties. The active surface makes nanodiamond applicapable to the wide range of industry through surface functionalization. Nanodiamond is being applied to the electroplated coating, polymer, abrasive, lubricant, et al., which improves the quality of target material (i) Electroplated coating : Increased durability and lifespan of the product (ii) Polymer : Increased wear resistance and hardness of polymer (iii) Lubricant: Increased effectiveness of lubricating oil, therefore resulting in the lifespan of engine parts. Typically DNPs (diamond nanoparticles) consist of 4–6 nm diamond nanocrystals coated by a fullerene-like carbon layers (sp^2) on their surface. They are aggregated into

particles 20–50 nm in diameter.[16] Incorporation of DNPs into coatings or bulk materials is of considerable interest to impart the remarkable properties of diamond to coating surfaces and composites.[17] In order to disperse aggregated DNP particles and to give chemical affinity, the chemical functionalization of DNPs may be an option to prevent close surface interaction among DNPs. However, the functionalization of DNPs should be carried out in less or nondestructive reaction medium to maintain their outstanding properties. Thus, the development of an efficient chemical modification method without or with little damages to the surface of DNPs must be an important challenge. The resultant polymer-based DNP composites are expected to display enhanced mechanical strength, wear resistance and thermal stability.[18] Polymer blends, mixtures of two polymers, often offer synergistic effects compared with the pure polymers such as better processibility, chemical resistance, and mechanical properties. However, most polymer pairs are immiscible. Without compatibilization, this leads to rough morphologies, poor phase adhesion and hence inferior mechanical properties. Thus, there is a great demand for additives to improve the compatibility of the polymer blends. These additives can, for example, be block copolymers made of the two blend components. The block copolymer is then located at the interface between the immiscible blend phases. It reduces the interfacial tension and avoids coalescence of the dispersed phase. This results in a finer morphology and better phase adhesion thus improving the properties of the blend. However, when melt mixing a block copolymer into a polymer blend much of the compatibilizer does not migrate into the interface but is lost by micelle formation. Due to the costs of block copolymers this can limit the process economically. Block copolymers as well as reactive polymers for compatibilization of blends can be synthesized by "living" free radical polymerization. Among the different methods one of the most versatile mechanisms is the atom transfer radical polymerization (ATRP) reported by Matyjaszewski.[19] The product of an ATRP has a bromine atom at one chain end. This opens the possibility to functionalize the polymer further by nucleophilic substitution reactions. Although the surface grafting of DNPs with organic polymers can improve properties, there have been very few works reported on the functionalization of DNPs.[20] In order to tailor the properties of resultant nanocomposites, it is necessary to control the composition, density, and thickness of the polymer shells attached to the nanofillers. Thus, new techniques need to be developed to modify DNPs in order to extend their applications. Atom transfer radical polymerization (ATRP) is one of the most versatile approaches to prepare nanocomposites, because of monomer availabilty, controllable macromolecular architectures with relatively low molecular weight distributions, and mild reaction conditions.[21] In fact, many types of polymers, such as poly(*n*-butyl methacrylate)[22], poly(methyl methacrylate)[23], poly(*tert*-butylacrylate)[24], poly(styrene)[25] and polystyrene-blockpoly(*tert*-butyl acrylate)[26], were successfully attached to CNMs by using *in situ* ATRP techniques.

As one component of an ATRP system, the initiator plays an important role. One has control over

the chemistry and structure of the initiator and active end group, so the a-bromination of carbonyl compounds is an important transformation in synthetic organic chemistry. α- Bromination of the side chain of aromatic ketones has attracted attention because the resulting bromoketones are intermediates for the synthesis of a variety of biologically active compounds. α -Bromination is the first step of introducing a heteroatom so as to provide additional conjugation to the carbonyl group, and for generating stabilized carbon radicals or carbanions. Various a-brominated carbonyl compounds have been synthesized using bromine in the presence of protic and Lewis acids, cupric bromide, dioxane dibromide, tetra-butylammonium tribromide and others. The environmentally hazardous bromine has given way to N-bromosuccinimide (NBS) as a user friendly reagent and the conditions for bromination have become milder with the advent of suitable catalysts and co-catalysts. The byproduct, succinimide, can be recycled. It has been reported that a-bromination of carbonyl compounds can be carried out by NBS, with radical initiators such as azobisisobutyronitrile (AIBN) and dibenzoyl peroxide (BPO). Das et al. and Tanemura et al.[27] reported that a-bromination using NBS over silica-supported sodium hydrogen sulfate and ammonium acetate leads to good yields of the corresponding ketones. However, this reaction requires high temperatures (~80 ^{o}C) and the reaction is slower for the formation of monobromoacyclic ketones. Adhikari and Samant[28] reported sonochemical a-bromination of acetophenones catalyzed by p-toluenesulfonic acid using NBS. Recently, Koo and co-workers[29] reported the a-bromination of carbonyl compounds catalyzed by trimethylsilyl trifluoromethanesulfonate in the presence of NBS. Thus, polymers can be end-functionalized and block copolymerized with other monomers using brominated carbonyl compounds as initiators. In recent decades, a variety of living radical polymerization techniques such as nitroxidemediated free radical polymerization (NMP)[30], reversible addition fragmentation chain transfer (RAFT)[31], and atom transfer radical polymerization (ATRP), have been well established. ATRP is a versatile technique to precisely control the chain length and polydispersity of the polymer, and can be used to synthesize well-defined copolymers. If the ATRP reaction conditions used are mild, a wide range of monomers and macromolecular structures can be used for grafting. It is generally believed that the living/controlled nature of ATRP is due to the relatively low radical concentration in the reaction system, which suppresses the termination relative to propagation. The mechanism of ATRP is shown in Scheme 1.

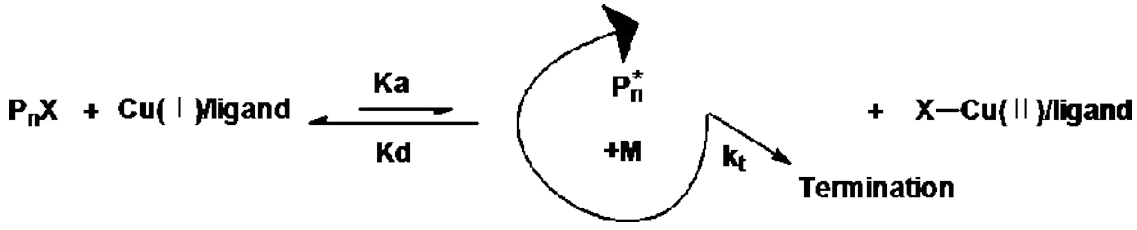

Scheme 1. The mechanism of atom transfer radical polymerization (ATRP).

The graft copolymerization of vinyl monomers onto the polystyrene backbone and other polymers using ATRP has attracted interest, only recently. The ATRP at ambient temperature has been studied and it has been established that ATRP at ambient temperature is less prone to side reactions and chain transfer, resulting in better control over molecular weight and PDI thus enabling the facile synthesis of polymers with well-defined structure. Thus ambient temperature ATRP is ideally suited toward the synthesis of a wide variety of molecular designs and thus can afford some novel types of tailored hybrid materials. Using only a few monomers and a living polymerization, one can create many new materials with vastly differing properties simply by varying the topology of the polymer (i.e., comb, star, dendritic, etc.), the composition of the polymer (i.e., random, periodic, graft, etc.), or the functional groups at various sites on the polymer (i.e., end, center, side, etc.) (Figure 2). And the initiator will give rise to an initiating radical species via homolytic cleavage of its labile bond, such as a carbon–halogen bond, by the catalysts. Most of the initiators for successful ATRP have been organic halides with a potentially active carbon–halogen bond and the obtained polymers usually have halogen atoms in the chain ends.[3 2]

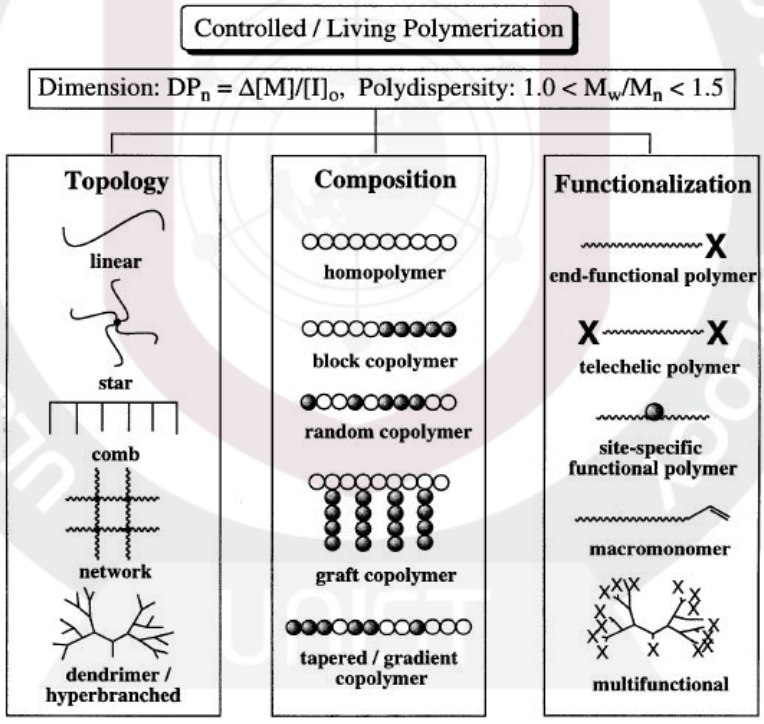

Figure 2. Representation of how new polymers and materials can be prepared from a few monomers using controlled/living polymerizations.

In this work, we would like to report the synthesis of diamond nanopowders (DNPs) containing reactive sites for the polymerization of methyl methacrylate (MMA) via atom transfer radical polymerization (ATRP) to afford poly(methyl methacrylate) grafted DNPs (PMMA-g-DNP).

DNPs/poly(methyl methacrylate) using. Thus, DNPs were functionalized with 4-ethylbenzoic acid (EBA) in a mild chemical modification condition in polyphosphoric acid (PPA)/phosphorus pentoxide (P_2O_5) medium, which is known to be an efficient "direct" Friedel-Crafts acylation reaction.[33] The resultant 4-ethylbenzoyl-functionalized DNP (EBA-g-DNP) was subsequently brominated using N-bromosuccinimide to obtain 4-(α-bromoethyl)benzoyl-functionalized DNP (BrEBA-g-DNP),[34] which is an ATRP initiator for MMA in the presence of a ligand compound. In this way, PMMA could be grafted from the surface of DNPs to prepare poly(methyl methacrylate) (PMMA) grafted DNP (PMMA-g-DNP). The mechanical properties of resultant PMMA-g-DNP composites are expected to be enhanced, because of the formation of covalent links between DNPs and PMMA. Moreover, this approach could suggest many more options to graft various polymers on DNPs, and to synthesize block copolymers by sequential ATRP copolymerization.

Ⅱ. Experimental

2.1 Materials

All reagents, solvents and diamond nanopowders (DNPs, ≥95%) were purchased from Aldrich Chemical Inc. and used as received, unless otherwise mentioned.

2.2 Instrumentations

Fourier-transform Infrared (FT-IR) spectra were recorded on a Jasco Fourier transform spectrophotometer model 480 Plus. All of the samples were mixed with dried KBr and pressed to form the semi-transparent pellets. The FT-IR spectrums were collected in the wavelength range from 650 to 4000 cm^{-1}. Raman analysis was conducted using a Alpha 300R (WlTec, Germany). Thermogravimetric analysis (TGA) used in this work was a TA Q200 equipped. TGA was conducted in air atmosphere with a heating rate of 10 °C/min. X-ray photoelectron spectroscopy (XPS) analysis was carried out on a Thermo Fisher K-alpha employing a monochromatic Al Kα radiation as the X-ray source. Wide-angle X-ray diffraction (WAXD) powder patterns were recorded with a Rigaku RU-200 diffractometer using Ni-filtered Cu Kα radiation (40 kV, 100 mA, λ = 0.15418 nm). Proton nuclear magnetic resonance (^{1}H-NMR) spectra were recorded on a VNMRS 600 (Varian USA), using $CDCl_3$ as solvent. The surface area was measured by nitrogen adsorption-fesorption isotherms using the Brunauer-Emmett-Teller (BET) method using Micromeritics ASAP 2504N. Field emission scanning electron microscopy (FE-SEM) used in this work was FEI NanoSem 230. High resolution transmission electron microscope (HR-TEM) employed in this work was a JEOL JEM-2100F (Cs) operating at 200 kV. The TEM samples were prepared by dipping a holy carbon micro-grid into dispersed samples in ethanol.

2.3 3 Functionalization of DNP with 4-ethylbenzoic acid in PPA/P_2O_5 at 130 °C (EBA-g-DNP)

Into a 100mL resin flask equipped with a high torque mechanical stirrer, nitrogen inlet and outlet, EBA (0.7g, 0.0047 mol), DNPs (0.7g), PPA (83% P_2O_5 assay; 28g), and phosphorus pentoxide (P_2O_5, 7g) were placed and stirred under dry nitrogen purge at 130 °C for 72h. After cooling down to room temperature, water was added to the reaction mixture. The resulting precipitates were collected by suction filtration and washed with distilled water several times. The product was then transferred to glass thimble, Soxhlet extracted with water for three days and with methanol for three days. Finally, the resultant powder was freeze-dried under reduced pressure (0.05mm Hg) for 24h to afford to 0.96 g

(72.72 % yield) of a deep gray powder. Anal. Calcd. for $C_{27.04}H_9O_1$: C, 92.83%; H, 2.59%; O, 4.57%. Found: C, 85.03%; H, 2.10%; N, 5.43%.

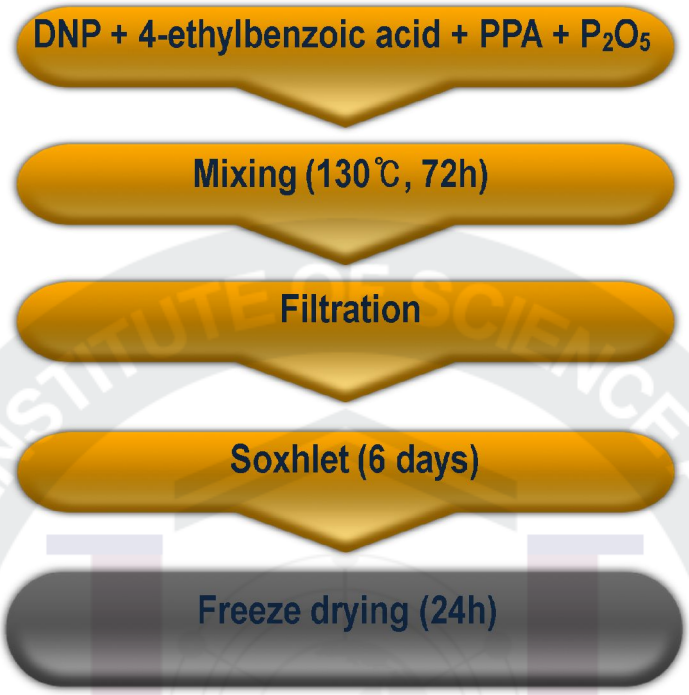

Figure 3. Experimental procedure for functionalization of DNP.

Figure 4. Apparatus for purification, functionalization and Soxhlet extraction.

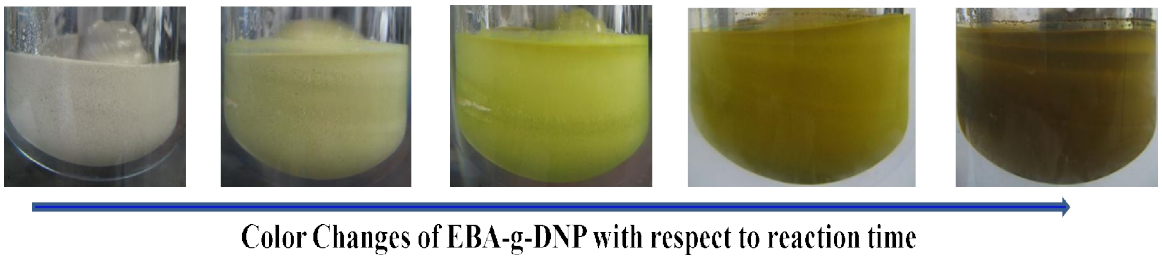

Figure 5. Reaction mixture of functionalized DNP with EBA.

2.4 Bromination of EBA-g-DNP using NBS (BrEBA-g-DNP)

Into a three-necked round bottom flask, EBA-g-DNP (0.5 g), N-bromosuccinimide (NBS, 1.4 g) and benzoyl peroxide (BPO, 0.13 g) in tetrachloromethane (8ml) were charged and the reaction mixture was heated under reflux at 90 °C (oil bath temperature). The bath temperature was slowly increased to 100 °C for 1h. Then, the reaction mixture was cooled in ice bath. The product was collected by suction filtration, Soxhlet extracted with water for two days. Finally, the resultant powdery product was freeze-dried under reduced pressure (0.05mm Hg) for 24h to afford to 0.5 g of a brown powder (34 % yield). Anal. Found : C, 79.52%; H, 1.82%; O, 6.57%.

2.5 ATRP of MMA initiated by BrEBA (PMMA)

Into a 50 ml reaction ampule, MMA (10.0 g, 100 mmol), BrEBA (0.015 g, 0.1 mmol), CuBr (0.014 g, 0.1 mmol), PMDETA (0.017 g, 0.1 mmol) and anhydrous toluene (6 mL) were charged and sealed with glass-cock. The reaction mixture was degassed by five freeze-pump-thaw cycles to remove any trace of oxygen. After this procedure, the ampule was torch-sealed and immersed in an oil bath at 60 °C immediately and kept stirring for 20 h. The reaction mixture was then diluted in THF (100 mL). The product was passing through an aluminum oxide to remove residual metal catalyst, and part solvent was removed on rotary evaporator. The viscous residue was poured into methanol, and white precipitate was collected by filtration vacuum-dried at 50 °C under reduced pressure (0.05mm Hg)for 24h to afford to 4.23 g (42 % yield) of white powder. Anal. Found : C, 60.28%; H, 8.12%; O, 32.69%.

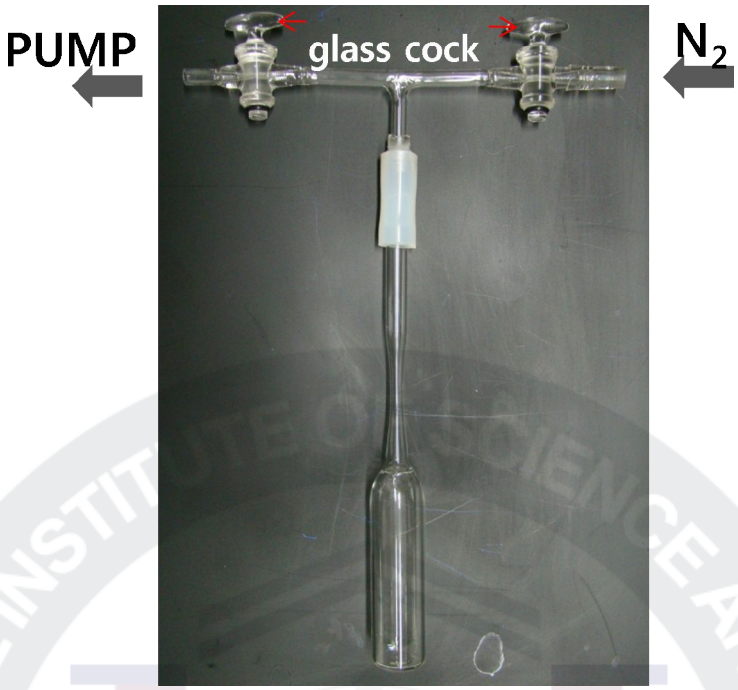

Figure 6. Photograph of Ampule.

2.6 ATRP of MMA initiated by BrEBA-g-DNP (PMMA-g-DNP 1)

Similar to the ATRP and work-up procedures for MMA initiated by BrEBA, MMA (10.0 g, 100 mmol), BrEBA-g-DNP (0.015 g, 0.1 mmol), CuBr (0.014 g, 0.1 mmol), PMDETA (0.017 g, 0.1 mmol) and anhydrous NMP (8 mL) were charged into a 50 ml ampule and sealed with glass-cock, degassed by five freeze-pump-thaw cycles. The rest of reaction and work-up procedures were almost the same for MMA initiated by BrEBA to afford 1 g (10% yield) of light gray powder.

2.7 ATRP of MMA initiated by BrEBA-g-DNP (PMMA-g-DNP 2)

Similar to the ATRP and work-up procedures for MMA initiated by BrEBA, MMA (3.0 g, 30 mmol), BrEBA-g-DNP (0.033 g, 0.15 mmol), CuBr (0.020 g, 0.15 mmol), PMDETA (0.026 g, 0.15 mmol) and anhydrous NMP (6 mL) were charged into a 50 ml ampule and sealed with glass-cock, degassed by five freeze-pump-thaw cycles. The rest of reaction and work-up procedures were almost the same for MMA initiated by BrEBA to afford 0.11 g (3% yield) of deep brown powder. Anal. Found : C, 66.17%; H, 6.49%; O, 24.59%.

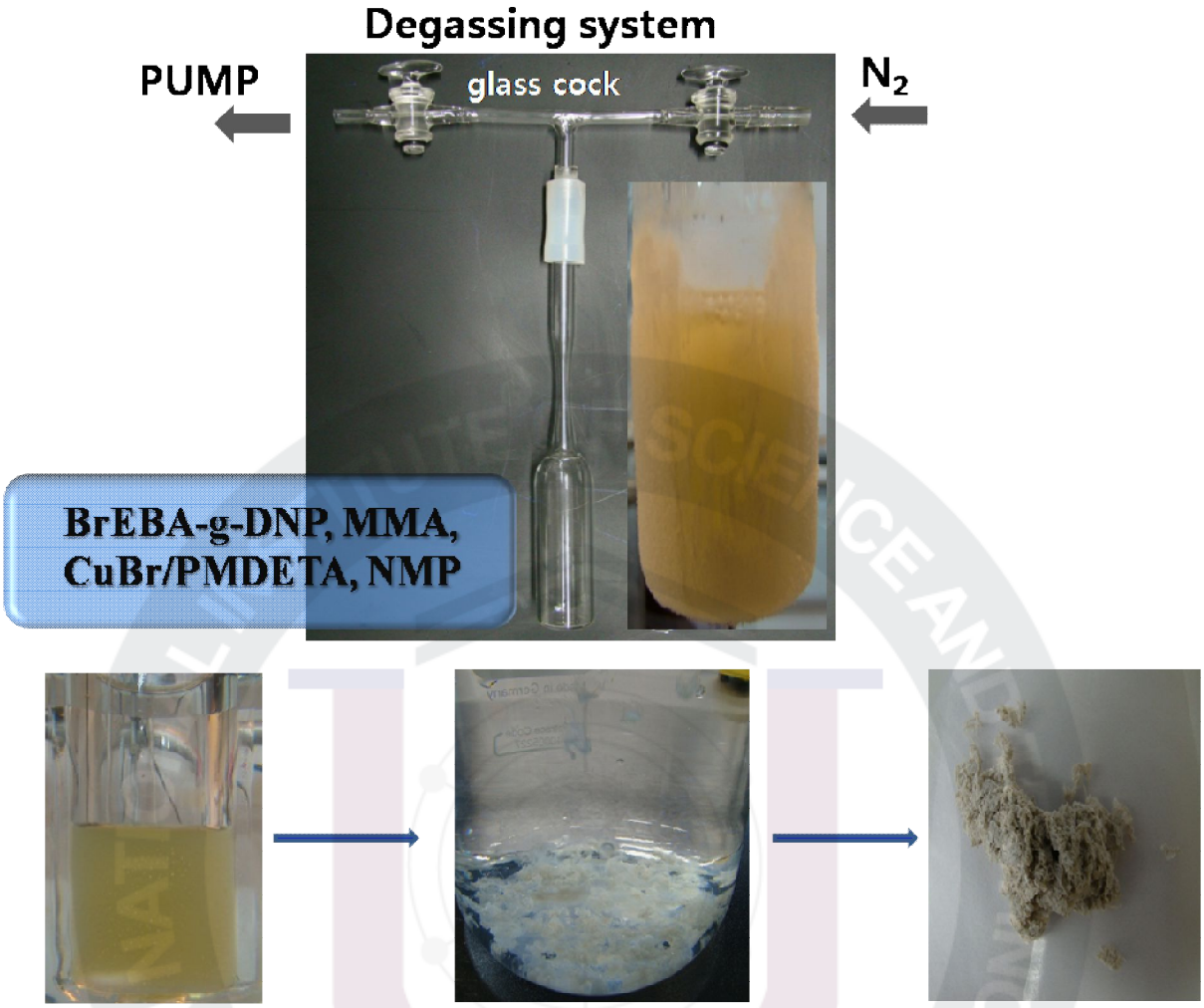

Figure 7. ATRP procedure of MMA with BrEBA-g-DNP as initiator.

Ⅲ. Results and discussion

Previously, we have reported the functionalization of MWNT, SWNT, VGCNF, fullerene (C_{60}) via Friedel-Crafts acylation reaction in polyphosphoric acid (PPA)/phosphorous pentoxide (P_2O_5) mixture.[35] In this study, diamond nanopowders (DNPs, ≤10nm) produced by nanospray combustion process was functionalized in the similar reaction condition.[36] As noted by DNP have never been isolated in pure form (>99.9 % carbon)[37]. Elemental analysis of the pristine DNP has revealed significant presence of heteroatoms (H, N, O) in addition to carbon (Table 1). The carbon content 85.58 % instead of theoretical value of 100 % in a pure diamond. However, the diamond content (77 %) of DNP is even lower than natural diamond (99.42 %). Therefore, an isolated diamond nanoparticle may be considered as having a centeral diamond (sp^3 C) core surrounded by an outer shell comprising of a mixture of sp^2 and sp^3 carbon. It is conceivable that a hydrogenated surface or a fullerenic outer shell ("Bucky diamond") may also exist. On the basis of the information on the sp^2 and sp^3 C-H contents and the sp^2/sp^3 carbon ratios of various grades of DND samples which would be susceptible to a Friedel-Crafts acylation in PPA/P_2O_5 medium. Although in colloidal solution the primary DND particles are 2-6 nm in diameter, they readily self-organize, upon solvent removal, into clusters or primary aggregates (20-30 nm), which in turn form larger but weakly bonded secondary aggregates in a broad size distribution, ranging from hundreds of nanometers to a few micrometers sizes, as shown in SEM images (Figure 16a). This agglomeration observed in solid state is driven by the surface functional groups with high polarity and strong H-bonding capability, such as COOH, OH etc., which were created along with the other functionalities by postsynthesis, acid treatment to purify raw DND. Thus, to disperse the DND quickly into PPA during the reaction, the pristine DND powder was gently ground to particulate with sizes of 20-30 nm using a spatula (Figures 16c, d).

The synthesis approach is described in Scheme 2. Firstly, DNP was functionalized with 4-ethylbenzoic acid (EBA) in polyphosphoric acid (PPA)/phosphorus pentoxide (P_2O_5) (Scheme 1a) to afford EBA-g-DNP. The resultant EBA-g-DNP was subsequently brominated with N-bromosuccinimide (NBS) to give brominated EBA-g-DNP (BrEBA-g-DNPs) (Scheme 1b). The viability of α-brominated EBA (Br-EBA) as an atom transfer radical polymerization (ATRP) initiator for MMA polymerization was tested (Scheme 1c) and successfully worked out. Hence, the BrEBA-g-DNPs can be used as initiator for grafting polymerization of MMA onto the surface of DNP (Scheme 1d). Moreover, the proposed mechanism of the electrophilic substitution reaction is "direct" Friedel-Crafts acylation between aylium ion (R-C^+=O) of EBA and sp^2 CH of DNP to give EBA-g-DNP (Scheme 3).

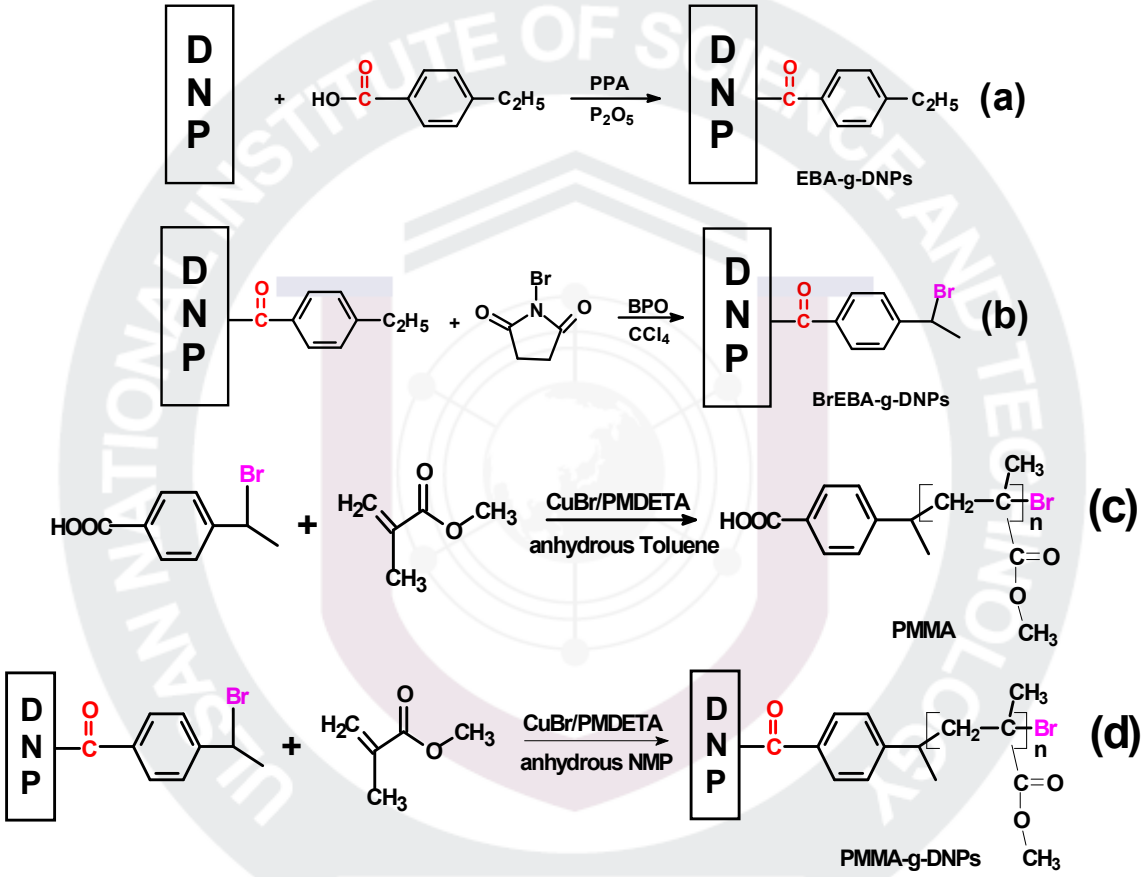

Scheme 2. Synthesis of (a) EBA-g-DNPs, (b) BrEBA-g-DNPs, (c) PMMA, (d) PMMA-g-DNP.

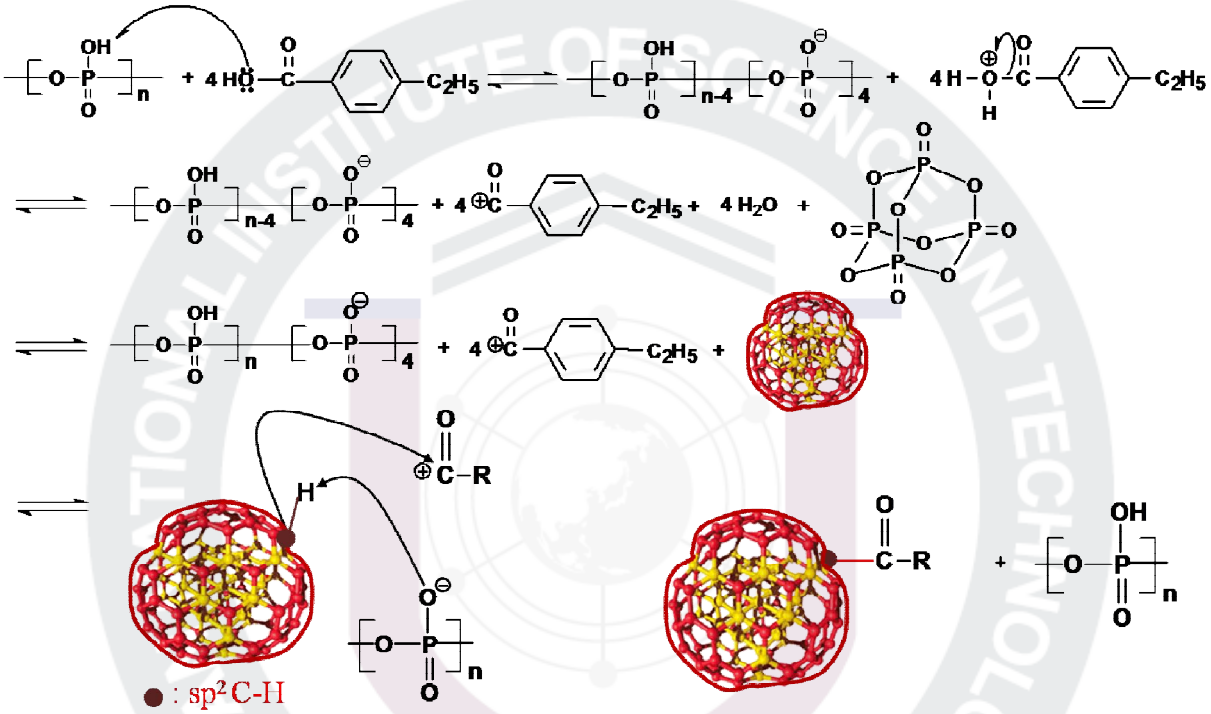

Scheme 3. Proposed mechanism of "direct" Friedel-Creafts acylation reaction between acylium ion ($R\text{-}C^{+}=O$) and $sp^2C\text{-}H$ of DNP.

Table 1. Elemental analysis of samples.

Sample	TGA (in air)		Elemental Analysis			
	$T_{d5\%}$[a] (°C)	char[b] (%)		C (%)	H (%)	O (%)
DNP	578	~0	Calcd.	100	0.00	0.00
			Found	85.58	1.22	2.05
EBA-g-DNP	445	~0	Calcd.	88.73	2.70	8.56
			Found	85.03	2.10	5.43
BrEBA-g-DNP	333	~0	Found	79.52	1.82	6.57
PMMA	280		Found	60.28	8.12	32.69
PMMA-g-DNP (PDG 2)	177		Found	66.17	6.49	24.59

[a] The temperature at which 5% weight loss ($T_{d5\%}$) occurred on TGA thermogram obtained with heating rate of 10 °C/min.

[b] Char yield at 850°C.

3.1 FT-IR Study

The functionalization of DNPs was conveniently monitored by FT-IR. Representative FT-IR spectra of pristine DNP, functionalized DNP, initiator-bound DNP (BrEBA-g-DNP), PMMA, PMMA-g-DNP 1 and PMMA-g-DNP 2 polymer composites are shown in Figure 1. The FT-IR spectra of pristine DNPs (Figure 8a) show the weak sp^2C-H and sp^3C-H bands around 2923 cm^{-1}. The sites, specifically sp^2C-H, are available for the Friedel-Crafts acylation reaction. After functionalization of EBA, EBA-g-DNP shows new keto-carbonyl (C=O) peak at 1710 cm^{-1} and aromatic C=C peak at 1605 cm^{-1} (Figure 8b). In the case of BrEBA-g-DNP, it is difficult to detect Br peaks (Figure 8c), since bromine stretching is typically so weak. After ATRPs reaction, characteristic signature peaks for PMMA, PMMA-g-DNP1 and PMMA-g-DNP2 are also compared (Figure 8d, 8e, 8f). Due to the amount of BrEBA-g-DNP is low, overall spectra are almost identical. The highest peaks at 1738 cm^{-1} and 1148 cm^{-1} are corresponded to the keto-carbonyl (C=O) from aliphatic ester and C-O stretching, respectively.

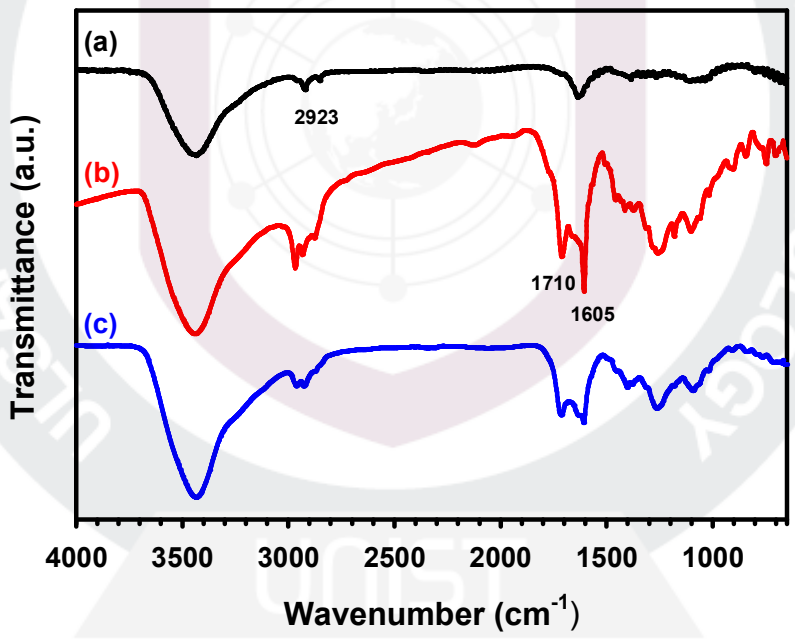

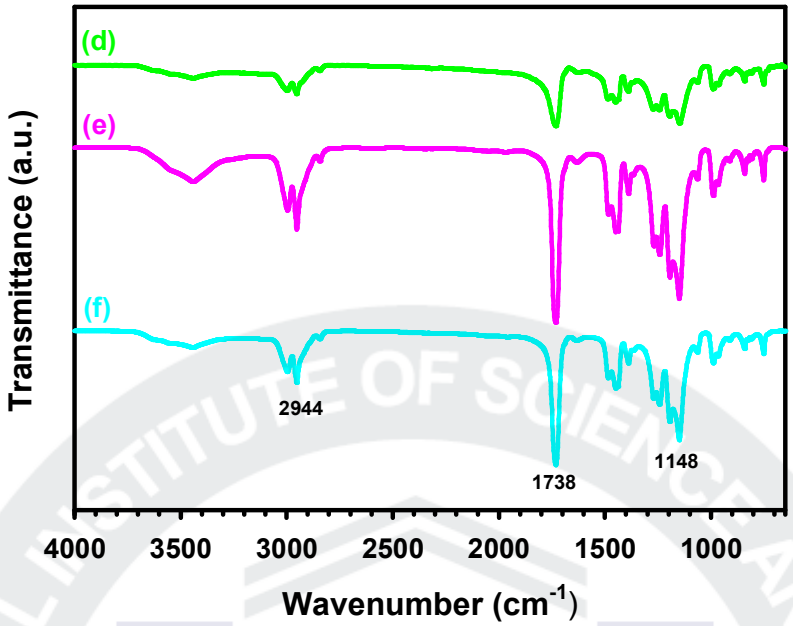

Figure 8. FT-IR (KBr pellet) spectra of (a) DNPs, (b) EBA-g-DNPs, (c) BrEBA-g-DNPs, (d) PMMA, (e) PMMA-g-DNP1, (f) PMMA-g-DNP2.

3.2 Raman spectroscopy

The Raman spectroscopy of DNP and EBA-g-DNP in Figure 9 is composed of three characteristic peaks for the diamond nanoparticles. The raw DNP was chosen because of its large content of nondiamond carbon and more evident spectral changes. The Raman spectrum of DNP show the disorder-induced double-resonance D band at ~1400 cm^{-1} [38] the unshifted graphite G band at 1600 cm^{-1}, and the downshifted and broadened, with respect to the Raman mode of single-crystal diamond (1332 cm^{-1}), diamond peak at ~1325 cm^{-1} [39] (Figure 9). Oxidation evidently removed fullerenic shells and other sp^2-bonded carbon impurities from pristine DNP, it also influences the surface chemistry and thus affects the shape of the Raman peaks. The appearance of a shoulder at 1140-1300 cm^{-1} as well as the upshift of the G peak to ~1640 cm^{-1} in the modified DNP could be the manifestations of bond formation of carbonyl oxygen containing functional groups on sp^2- or sp^3-bonded carbon.[40] The intensity ratio of D/G band intensity (I_D/I_G) of the functionalized DNP is about six times larger than that the pristine DNP. This again suggests that DNP is successfully functionalized with 4-ethylbenzoic acid as increased intensity of disorder-induced double-resonance D band at ~1400 cm^{-1}.

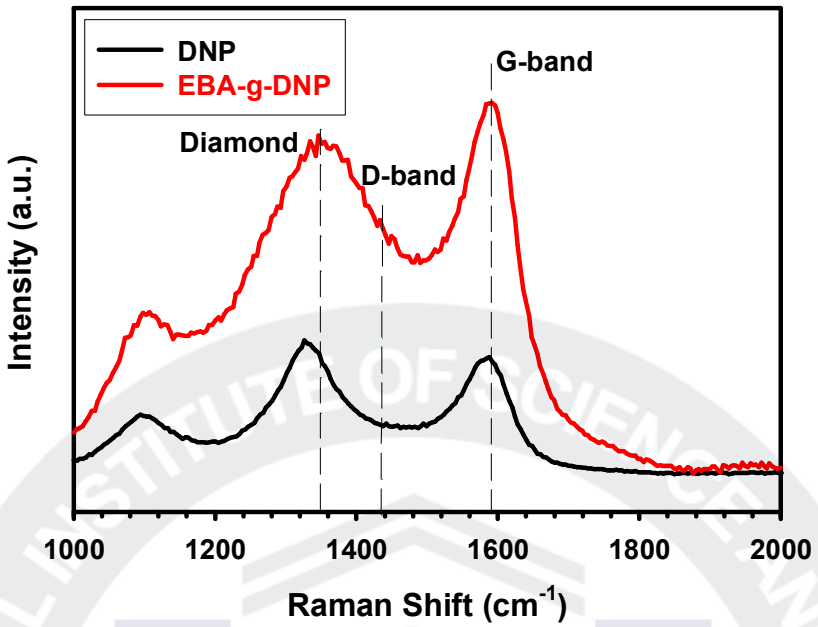

Figure 9. Raman Spectra of DNP and EBA-g-DNP.

3.3 BET (Brunauer, Emmett, Teller)

To measure surface area and pore volume using the BET method, the DNP and EBA-g-DNP were degassed under vacuum at 250 °C before measurement. The surface area of DNP and EBA-g-DNP were 262.14 and 248.11 m^2/g, respectively (Table 2). The surface area of EBA-g-DNP was decreased by ~6 %, this result shows that EBA-g-DNP was filled in the gaps with EBA moiety on the surface of DNP. Furthermore, pore volume of EBA-g-DNP was decreased by ~12 % than pristine DNP which implied that EBA-g-DNP should be more compact morphology (Figure 10).

Table 2. BET Surface Area, Pore Volume of DNP and EBA-g-DNP.

Sample	**Surface Area (m^2/g)**	**Pore Volume (cc/g)**
DNP	262.14	1.12
EBA-g-DNP	248.11	0.98

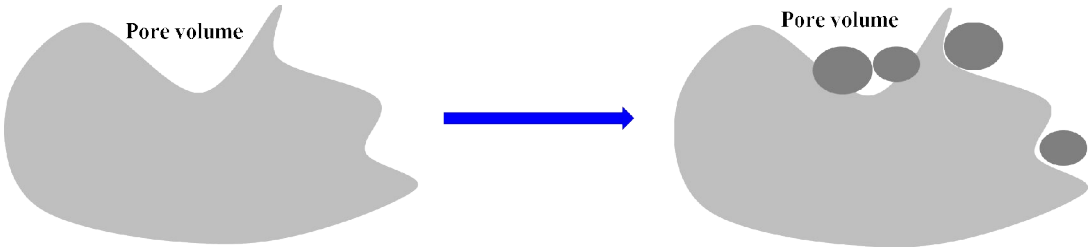

Figure 10. Physical adsorption and desorption isotherms of DNP and EBA-g-DNP.

3.4 XPS (X-ray photoelectron spectroscopy)

To confirm the existence of necessary elements in the EBA-g-DNP, BrEBA-g-DNPs and PMMA-g-DNPs were subjected to XPS analysis. The XPS surveys show that major C1s and O1s peaks at 285 and 534 eV, respectively (Figure 11a). The Br3d at 70.5 eV (Br; combined carbon) was observed after bromination (Figure 11a, inset). The quantity of measured Br on BrEBA-g-DNP and PMMA-g-DNP1 were 0.73 *At%*, 0.71 *At%,* respectively, assuring that the presence of bromine. For qualitative analysis, the C1s peaks of DNP, BrEBA-g-DNP and PMMA-g-DNP1 were magnified as shown in Figure 11b. After modification, the peak position of EBA-g-DNPs was shifted from 287.8 eV to 284.9 eV due to attached C_6H_5CO.[41] Figure 11c shows that C1s of PMMA-g-DNP1 was fitted with C-C, C-O, OCH_3, and C=O (combined C_6H_5).

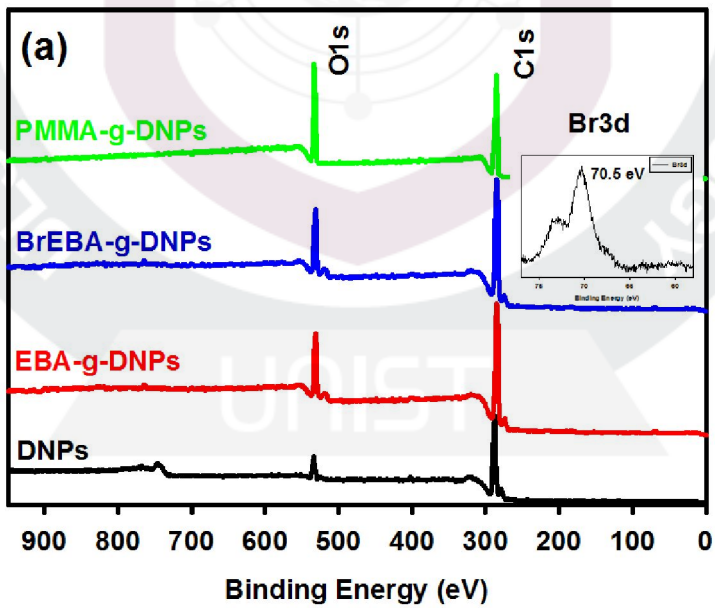

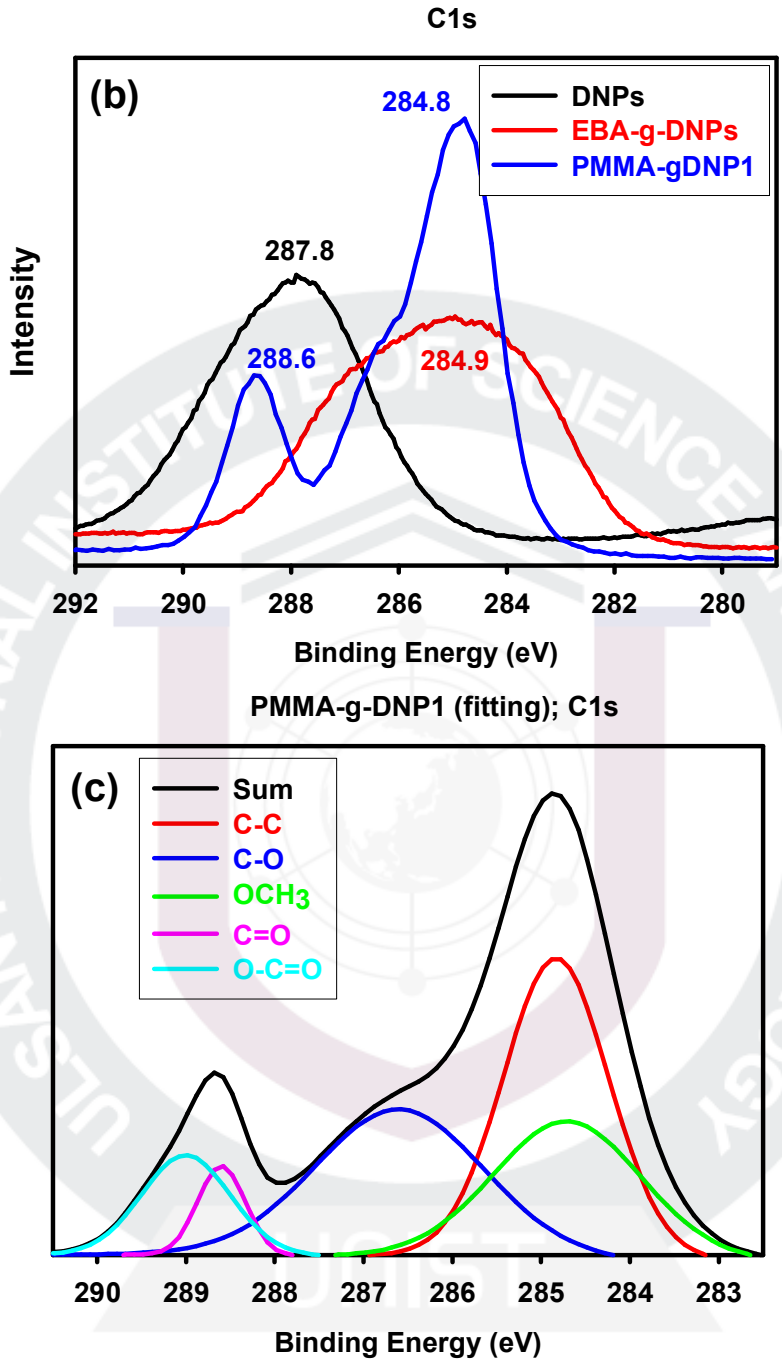

Figure 11. XPS spectra: (a) full spectra (inset, magnified peak of the Br3d), (b) The C1s peaks of DNP, BrEBA-g-DNP and PMMA-g-DNP1, (c) fitted C1s from PMMA-g-DNP1.

3.5 ^{1}H NMR Characterization

^{1}H NMR spectra of pure PMMA and PMMA-g–DNP2 provide clear evidence of ATRP polymerization of MMA with α-brominated initiators (Figure 12 (a, b)). Firstly, to prove the possibility of bromination with NBS, we prepared brominated EBA and compare with 4-ethylbenzoic acid. From H NMR and C NMR, we confirmed that signal for CH_3 were shifted after bromination. Overall NMR of brominated EBA signal affected bromine. For instance, proton signals for Br-C-H at δ = 5.21 ppm shifted after bromination (Figure 12a) and carbon signals for Br-C-H at δ = 47.78 ppm shifted due to attached bromine (Figure 12b). All the characteristic proton peaks attributed to PMMA can be found in the spectrum of PMMA-grafted DNPs (Figure 12(c, d)). For example, the proton signals for –$OCOCH_3$ at δ = 3.59 ppm,[4 2] proton signals for C–CH_2–C at δ = 1.78 ppm, and proton signals for −CH_3 at δ = 0.84–1.02. All these results strongly support that PMMA has been successfully initiated by α-brominated initiators (BrEBA and BrEBA-g-DNP). Hence, the grafting of PMMA onto the surface of DNP is indeed viable approach to synthesize PMMA-g-DNP via atom transfer radical polymerization (ATRP).

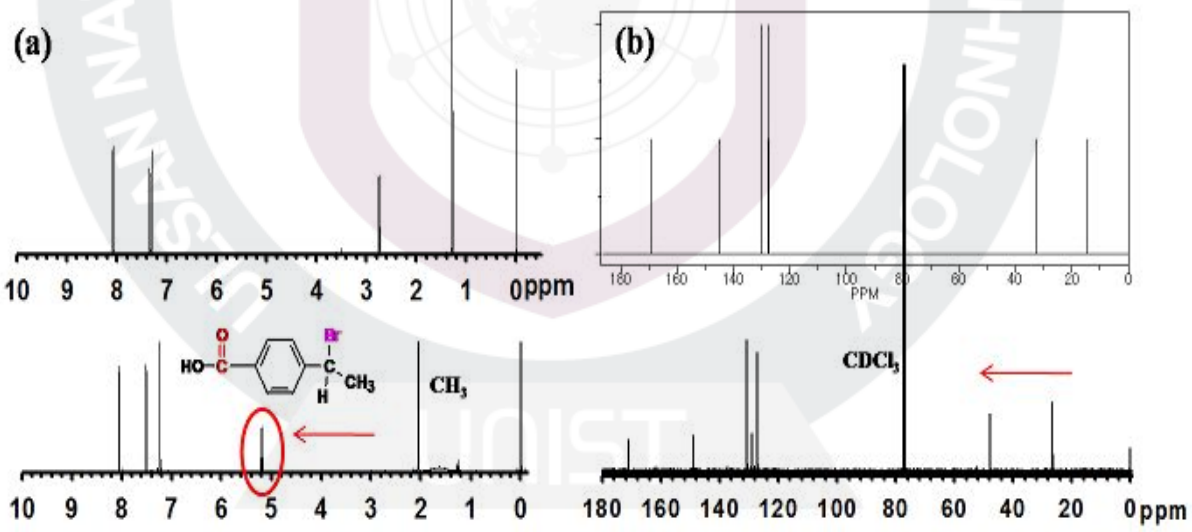

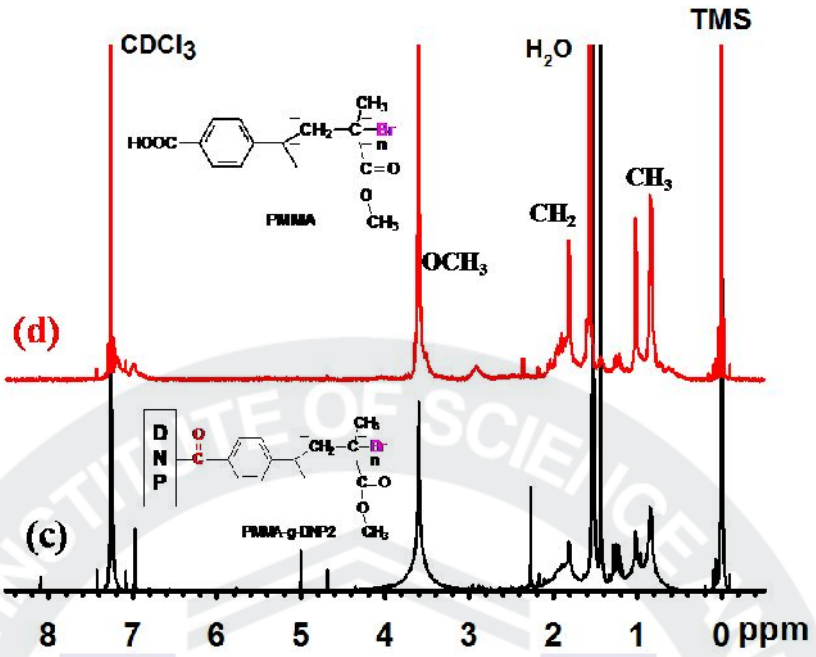

Figure 12. (a) ^{1}H NMR spectrum ($CDCl_3$) of EBA and BrEBA, (b) ^{13}C NMR spectrum ($CDCl_3$) of EBA and BrEBA, (c) ^{1}H NMR spectrum ($CDCl_3$) of PMMA-g-DNP2 and (d) ^{1}H NMR spectrum ($CDCl_3$) of PMMA.

3.6 Thermal Properties

The thermogravimetric analysis (TGA) experiments on the powder samples of DNP, EBA-g-DNP, BrEBA-g-DNP, PMMA, PMMA-g-DNP1 and PMMA-g-DNP2 indicated that the temperatures at which a 5% weight loss ($T_{d5\%}$) in air occurred at 578, 445, 333, 280, 305 and 177 °C in that order (Figure 13 and Table 3). As-received DNPs is fairly stable up to 500 °C. It showed that the temperature at which 5 wt% weight loss ($T_{d5\%}$) occurred was at 578 °C. The char yield at 800 °C was almost 0 wt%. In the case of the EBA-g-DNPs and BrEBA-g-DNPs early weight loss started around 400 and 240, respectively. The first-stage weight loss approximately at 500, 400 °C approached about 7 wt%, respectively (Figure 13a), which was presumably because of the detachment of ethyl group and α-bromine on the ethyl group. Interestingly, EBA-g-DNP and BrEBA-g-DNP displayed better thermal stability pristine DNP after EBA and BrEBA moieties were carbonized. There could be two reasons attributed to the improved thermal stability of EBA-g-DNP and BrEBA-g-DNP. The one is presumably PPA/P_2O_5 medium plays functionalization and purification.[43] Simply, some impurities were removed such as graphitic shell or onion-like fullerene during the functionalization in the reaction medium. The other would be defects are healed during pyrolying (charring) process. Thermally generated carbon feedstock (radical, anion and cation) from EBA and BrEBA moieties could fix the defects present on the shell of DNP.

From the Figure 13b, the amount polymer grafts on the DNP could be estimated. The TGA curves of PMMA-g-DNP1 and PMMA-g-DNP2 show that major decomposition occurred in the temperature range of 260–400 °C due to thermal stripping of PMMA. The residual amount above 400 °C should be contributed to DNP. Thus, the PMMA content in PMMA-grafted DNPs can be calculated. As shown in Table 3, the weight fraction of grafted PMMA f_{wt}% increases from 77% to 96% with increasing stoichiometric ratio from 1:200 to 1:1000. Probably, the greater the f_{wt}%, the higher the molecular weight of grafted PMMA from DNPs. Thus, PMMA-g-DNP2 has poorer thermal stability than PMMA-g-DNP1 due to smaller molecular weight of the PMMA grafts. The TGA results suggest that the content of the PMMA grafts in the functionalized DNPs can be tuned by stoichiometric ratio.

Table 3. Thermogravimetric analysis (TGA) data of samples.

Sample	$T_{d5\%}$[a] (°C)	char[b] (%)	Sample	$T_{d5\%}$[a] (°C)	Char[c] (%)	f_{wt} (%)[d]
DNP	578	~0	PMMA	280	~0	~100
EBA-g-DNP	445	~0	PGD1 (1:1000)[e]	305	~0	96.7
BrEBA-g-DNP	333	~0	PGD2 (1:200)[e]	264	0.91	77.5

[a] The temperature at which 5% weight loss ($T_{d5\%}$) occurred on TGA thermogram obtained with heating rate of 10 °C/min.

[b] Char yield at 900 °C.

[c] Char yield at 700 °C.

[d] f_{wt} = the loss weight fraction of polymer calculated from TGA data.

[e] initiator : monomer (stoichiometry ratio)

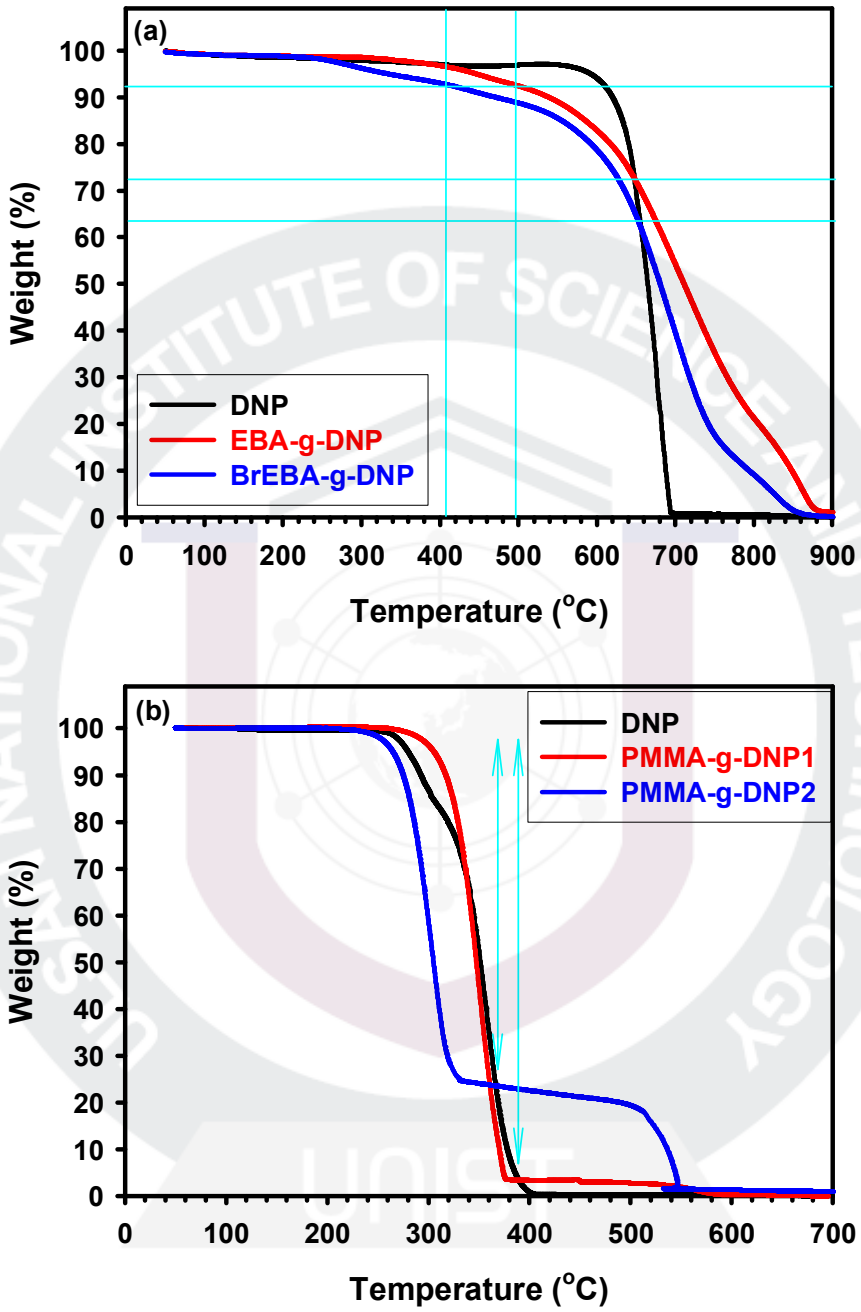

Figure 13. TGA thermograms obtained with heating rate of 10 °C/min in air.

3.7 Wide-Angle X-ray Diffraction (WAXD)

To monitor the morphologies of samples, XRD scattering patterns were obtained powder samples without applied strain. The XRD pattern of the as-received DNP shows that the intensity of the characteristic diamond *d*-spacing (111) appears at 2.07 Å and *d*-spacing (220) at 1.26 Å (Figure 14a).

Furthermore, characteristic peak of DNP is described after EBA modification and bromination (Figure 14b, 14c). Hence, it is reasonable to say that PPA is non-destructed reaction medium for chemical modification. After ATRP polymerization, PMMA-g-DNP1 and PMMA-g-DNP2 show overall broad amorphous peaks Figure 14e and 14f). As expected, PMMA-g-DNP1 and PMMA-g-DNP2 faintly show characteristic diamond peak (111) and the intensity is slightly proportionally increased with the amount of DNP increased in the samples.

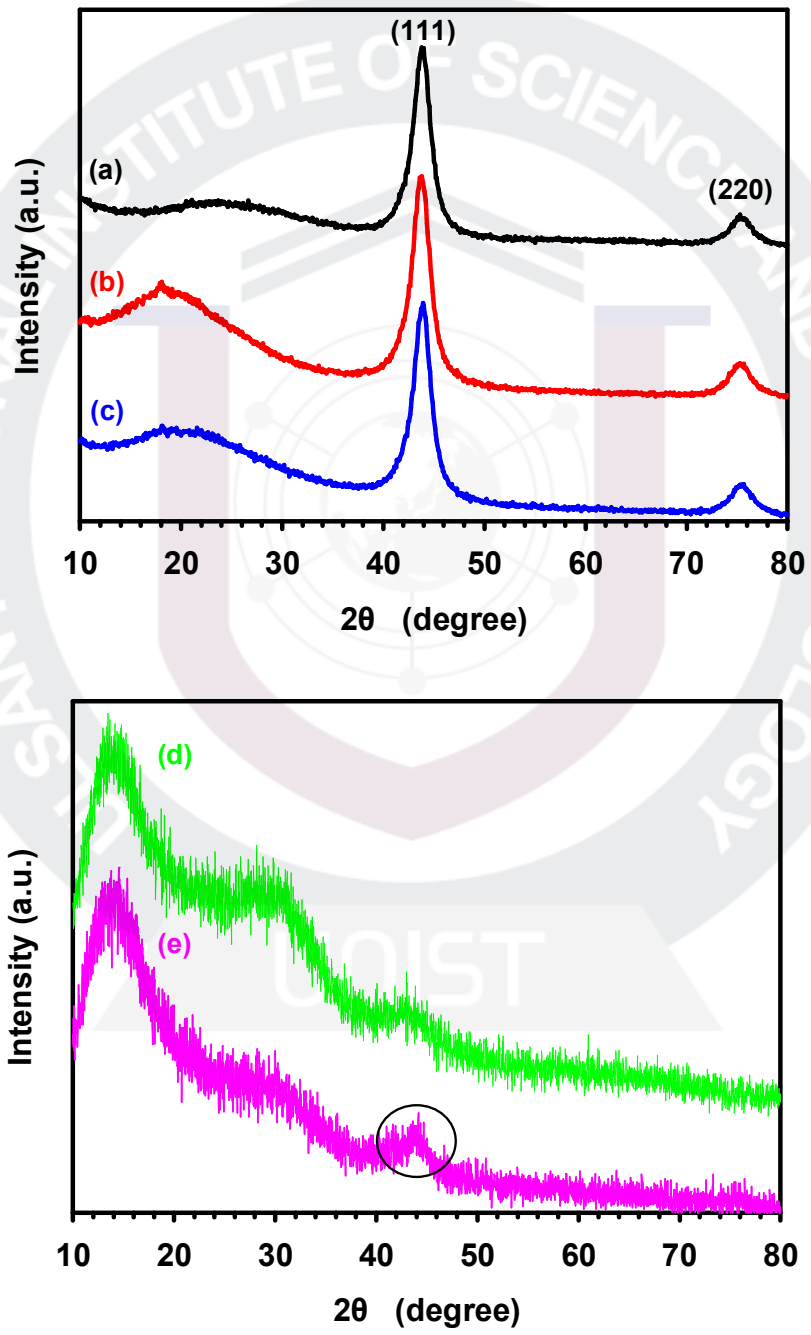

Figure 14. WAXD patterns: (a) DNPs, (b) EBA-g-DNPs, (c) BrEBA-g-DNPs, (d) PMMA-g-DNP1, (e) PMMA-g-DNP2.

3.8 UV-vis absorption behaviors.

UV-vis absorption measurements were conducted to have information of interfacial interaction between EBA and DNP. Stock solution (0.01mol/L) of each sample was prepared in NMP. The UV-absorption of DNP and EBA-g-DNP showed sharp peak at 258 nm (Figure 15a). And The UV-absorption of EBA-g-DNP showed relatively broad peak at 361 nm. This implied that EBA should be successfully grafted onto the surface of DNP. As can be seen, EBA-g-DNP exhibit larger absorbance than pristine DNP (Figure 15a), it is probably implied that double bond in EBA is more nicely show up during removed amorphous carbon. The UV-absorption of PMMA and PM-g-DNP1 showed sharp peak at ~258 nm and broad peak at 287 nm (Figure 15b).

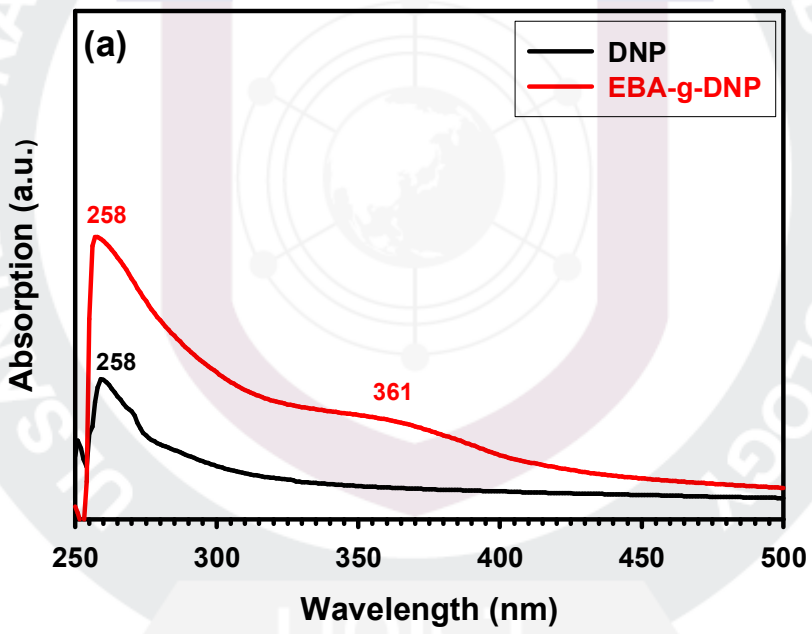

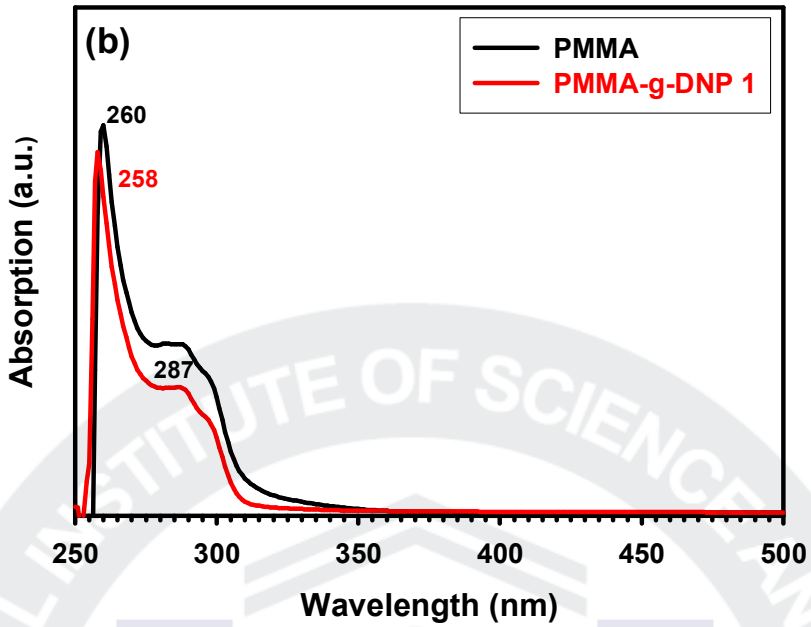

Figure 15. UV-Vis absorption spectra of samples: (a) DNP and EBA-g-DNP, (b) PMMA and PMMA-g-DNP1.

3.9 Scanning Electron Microscopy

The SEM images of pristine DNP show that the surface texture consisted of aggregates and agglutinates (Figure 16a). After EBA modification, while aggregated diamond nanoparticles were fairly individualized due to the molecular wedge effect of EBA (Figure 16b). Furthermore, the less polarity of EBA moiety on the surface of EBA-g-DNP helps the individualization. In the case of BrEBA-g-DNP, overall particle size was increased due to the polarity if its surface increased by bromine attachment (Figure 16c). The morphologies of PMMA-g-DNP1 (Figure 16e) and PMMA-g-DNP2 (Figure 16f) are quite different from that of PMMA (Figure 16d).The SEM image of PMMA-g-DNP1 appears to be a rugged surface covered with polymer shells. This could be caused by the increasing affinity among the polymer shells coated on the DNPs. When the polymer content is higher in PMMA-g-DNP2, which surfaces were so crowded and thus, polymer covers the surface. Thus, we conclude that the thickness of coated polymer shell in PMMA-g-DNPs is increased as polymer content increased, which agrees well with TGA result. Thus, the covalently grafting of PMMA onto the surface of DNP is fairly uniform and viable.

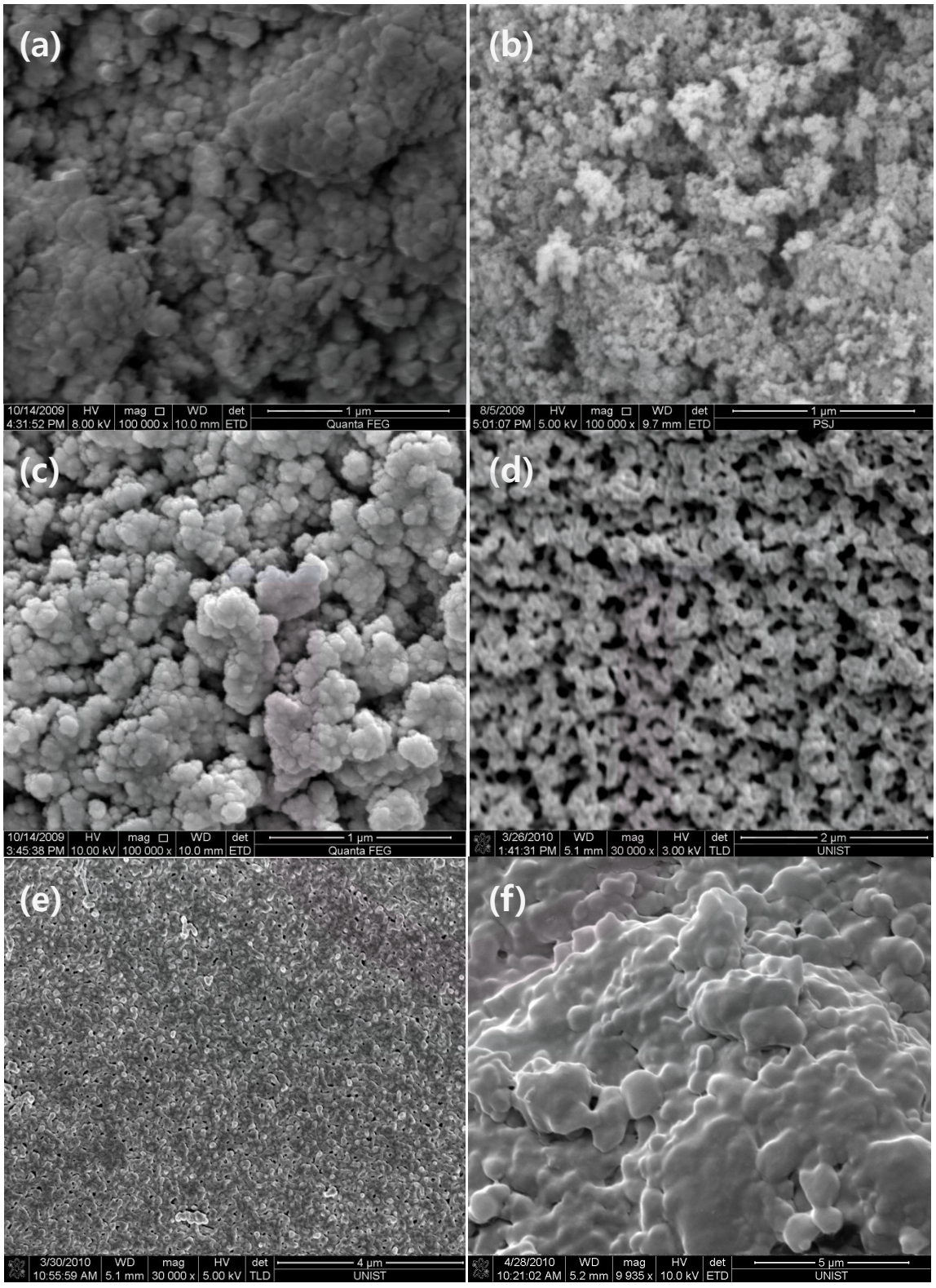

Figure 16. SEM images: (a) pristine DNPs (100,000×), (b) EBA-g-DNPs (100,000×), (c) BrEBA-g-DNPs (100,000×), (d) PMMA (100,000×), (e) PMMA-g-DNP1 (30,000×) and (f) PMMA-g-DNP2 (30,000×).

3.10 HR-Transmission Electron Microscopy (HR-TEM)

Pristine DNP, used in this study and prepared by nanospray combustion process, consists of diamond nanoparticles coated by a graphitic or onion-like fullerene matrix. The TEM images of pristine DNP show that DNP stays as aggregate and/or agglutinate form (Figure 17a, 17b). The images of the PMMA-g-DNP2 in Figures 17c and 17d could be clearly discernable between the diamond core and the PMMA shell. The images show an ordered crystalline core and a light amorphous polymeric coating marked by the red arrows. The space between crystalline DNPs is filled by amorphous PMMA, indicating that the grafting of PMMA onto the surface of DNP by using BrEBA-g-DNPs as the ATRPs's initiator is successful.

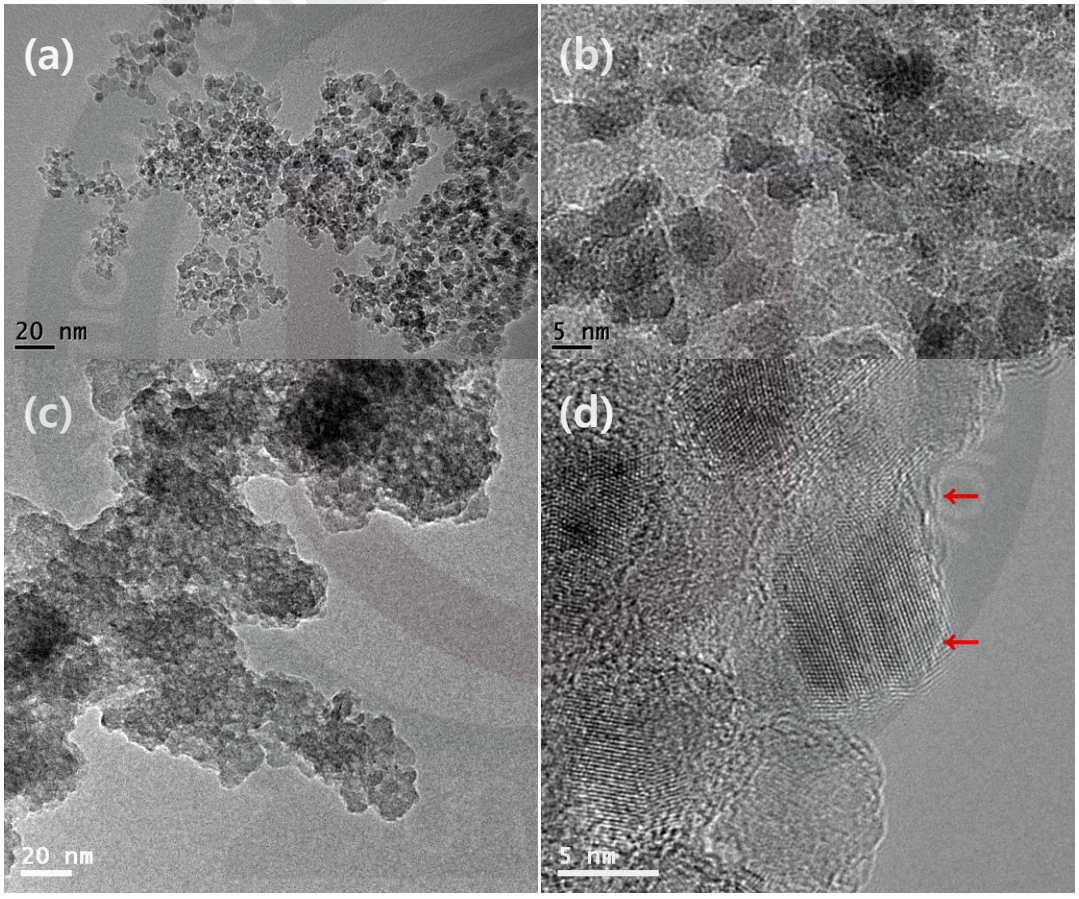

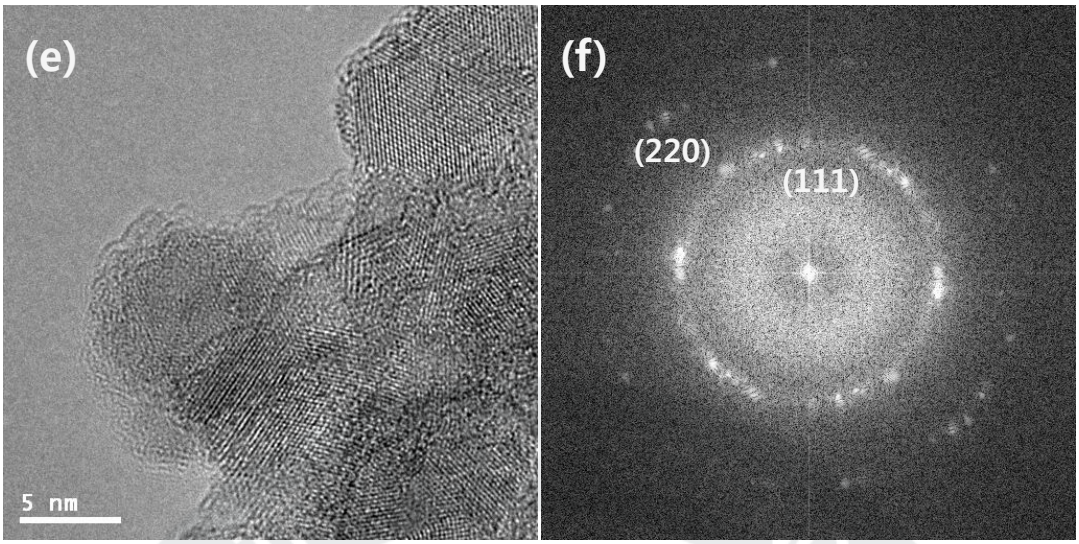

Figure 17. TEM images of (a) pristine DNP (100,000×), (b) pristine DNP (400,000×), (c) PMMA-g-DNP2 (100,000×), (d) PMMA-g-DNP2 (500,000×), (e) PMMA-g-DNP1 (500,000×) and (f) Electron diffraction pattern.

3.11 Optical Transmittance Spectra

Figure 18 shows the optical transmittance spectra for the PMMA and PMMA-g-DNP1 samples. Transparent films were produced from Tetrahydrofuran solution of the composite, as depicted inset Figure 11 (a). PMMA has a transmittance of 94 %. The loss of 6 % is caused by reflection on the two surfaces of the block (0.03 mm thickness). The final PMMA-g-DNP1 nanocomposite contains acrylates and small amounts of diamond nanoparticels. Larger particles and agglomerated DNPs would give rise to a significant reduction of the transmittance (44%)[44], with a resulting decrease in transmittance. Before re-agglomeration, evaporation of the solvent (THF) resulted in transparent films. Similarly, if the agglomerated solutions are agitated, the particulates break apart and the solution can be cast into clear films. Consequently, transmittance confirms the concept of our approach. The integration of nanoparticles allows for the incorporation of functional diamond nanoparticles that are visible by the human eye.

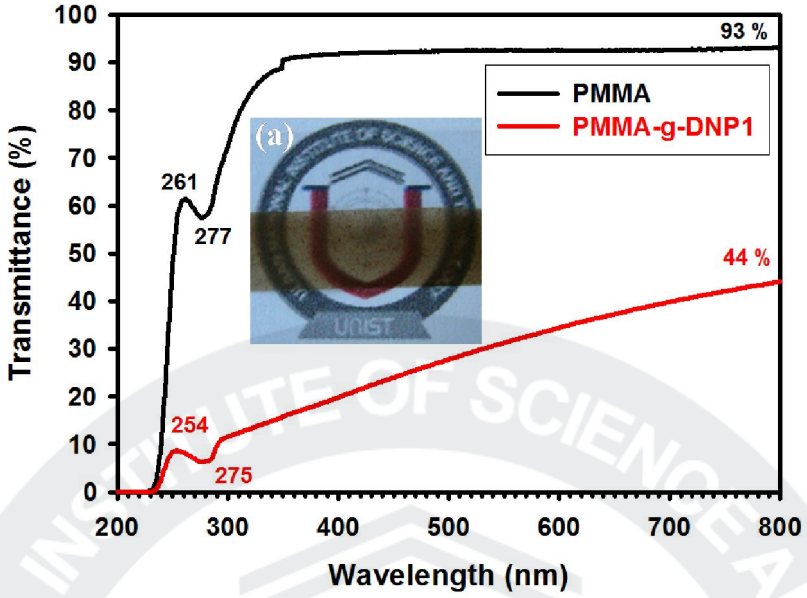

Figure 18. Transmittance UV-vis spectra of PMMA and PMMA-g-DNP1. (inset (a) Film of PMMA and PMMA-g-DNP1. Thickness is 0.03 mm)

3.12 Mechanical Properties

PMMA and PMMA-g-DNP1 composites were shaped into specimens with size of 4.7 X 8.5 mm^2 and thickness of 0.11-0.13 mm. Tensile strength and Modulus of samples are presented in Figure 19. Through TGA data, we know that PMMA-g-DNP2 has poorer thermal stability than PMMA-g-DNP1 due to smaller molecular weight of the PMMA grafts. And PMMA-g-DNP composites displayed homogeneously dispersed onto DNP surface (Figure 16e, f). So, we made film using the PMMA-g-DNP1. Compared with pure PMMA, strength and modulus of PMMA-g-DNP1 were increased as high as 3.4 %, 24 % respectively, which assured that PMMA-g-DNP1 composites systems with covalent linkage between reinforcing additive and matrix are expected to display better enhanced properties. The improvement of tensile modulus should be attributable to successful ATRP for introduced DNPs. Originally PMMA has good tensile strength properties [4 5] and because of agglomerated DNPs tensile strength value slightly increased than pure PMMA.

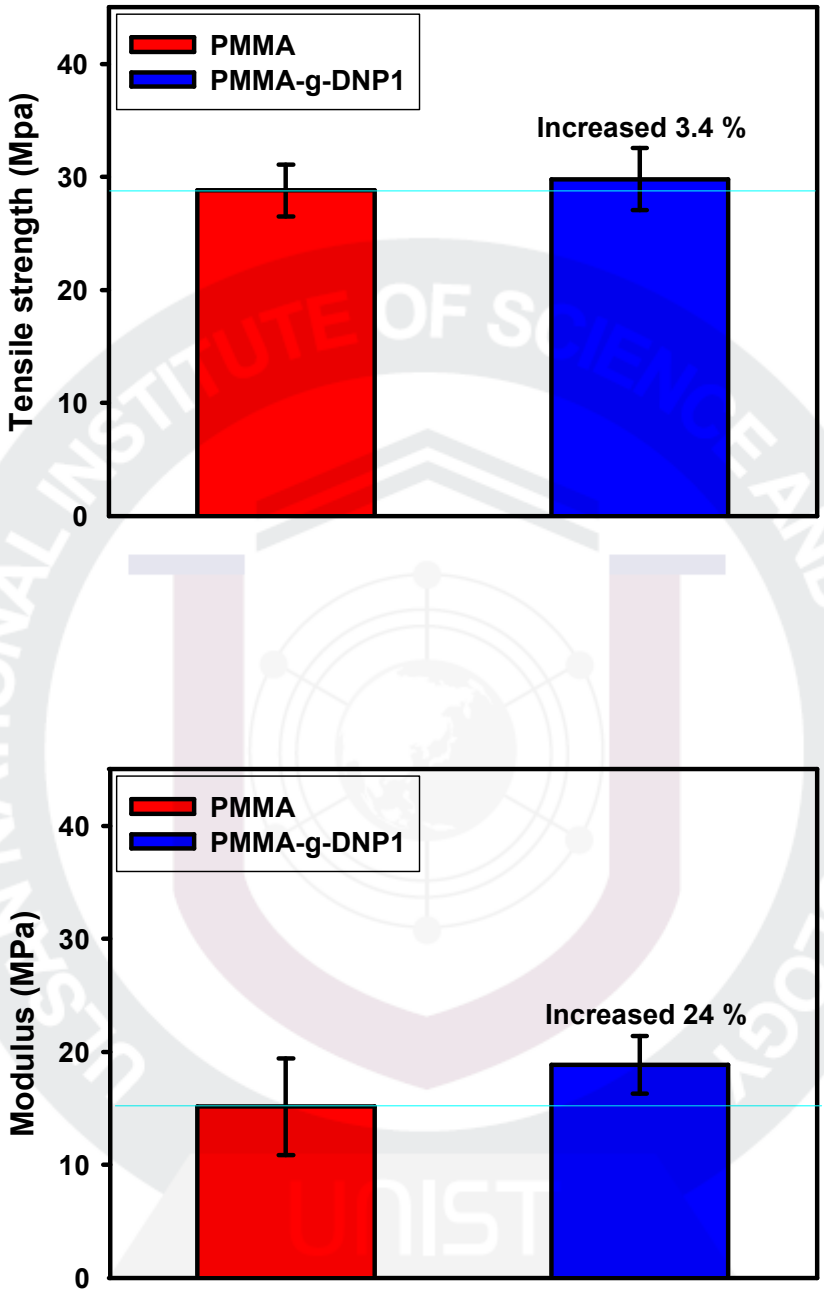

Figure 19. Tensile strength and modulus of PMMA and PMMA-g-DNP1.

Conclusions

In this paper, we verified that PPA/P_2O_5 is strong enough to facilitate Friedel-Crafts acylation reaction to the sp^2 C-H bonds of DNP's outer shell. Also, we learned that PPA/P_2O_5 medium plays functionalization and purification. And then, Poly(methyl metacrylate) (PMMA) grafted diamond nanoparticle (DNP) was prepared in the sequence of functionalizations and atom transfer radical polymerization (ATRP). Diamond nanoparticles (DNPs) were first functionalized by 4-ethylbenzoic acid (EBA) and the resultant EBA-g-DNP was brominated to prepare BrEBA-g-DNP as an initiator for ATRP. The functionalization of EBA onto the surface of DNP was confirmed by various analytic techaniques such as FTIR, TGA, XPS, XRD, SEM and TEM. By using BrEBA-g-DNP as an ATRP initiator, methyl metacrylate (MMA) was subsequently polymerized to afford PMMA grafted DNP (PMMA-g-DNP). On the basis of TGA data, we know that we can control amounts of DNP as stoichiometry ratio. Hence, we prepared PMMA-g-DNP films using PMMA-g-DNP 1 (stoichiometry ratio 1:1000). The homogeneous dispersion of PMMA onto DNP surface was visually confirmed by SEM and TEM image experiments. As a result, consequently, tensile modulus increased as high 24 % although considerable improvement of mechanical properties of PMMA-g-DNP films. The resultant nanohybrid materials showed core-shell structure. The thickness of PMMA shell could be tailored by stoichiometric feed ratio of MMA and BrEBA-g-DNP. The results envision that the chemistry first developed in this work is indeed viable and can be applicable for many other polymer-based DNP nanohybrid systems for application-specific materials.

REFERENCES

[1] SUMIO IIJIMA. 1991. Helical microtubules of graphitic carbonprotonated with camphorsulfonic acid. *Nature,* 354, 56-58.

[2] (a) Milo S. P. Shaffer, Alan H. Windle. 1999. Fabrication and Characterization of Carbon Nanotube/Poly(vinyl alcohol) Composites. *Advanced Materials*, 11, 937-941. (b) I-Chun Liu, Hsuan-Ming Huang, Ching-Yu Chang, Hung-Chieh Tsai, Chuan-Hsiao Hsu, and Raymond Chien-Chao Tsiang. 2004. Preparing a Styrenic Polymer Composite Containing Well-Dispersed Carbon Nanotubes: Anionic Polymerization of a Nanotube-Bound *p*-Methylstyrene. *Macromolecules*, 37, 283-287. (c) Tang, B.Z. Xu, H. 1999. Preparation, Alignment, and Optical Properties of Soluble Poly(phenylacetylene)-Wrapped Carbon Nanotubes. *Macromolecules,* 32, 2569-2576. (d) Mark Hughes, George Z. Chen, Milo S. P. Shaffer, Derek J. Fray, and Alan H. Windle. 2002. Electrochemical Capacitance of a Nanoporous Composite of Carbon Nanotubes and Polypyrrole. *Chemistry of Materials*, 14, 1610-1613. (e) Cochet, M. Maser, W.K.; Benito, A.M. Callejas, M.A. Martínez, M.T. Benoit, J.M. Schreiber, J. Chauvet, O. 2001. Synthesis of a new polyaniline/nanotube composite: in-situ polymerisation and charge transfer through site-selective interaction. *Chemical Communications,* 1, 1450–1451.

[3] (a) R. Kalish. 2007. Diamond as a unique high-tech electronic material: difficulties and prospects. *Journal OF Physics D: Applied Physics*, 40 6467–6478. (b) M. Heyns, W. Tasi. 2009. Ultimate Scaling of CMOS Logic Devices with Ge and III–V Materials. *Materials Research Society Bull.* 34, 485-488.

[4] (a) Li, J. Ma, P.C. Chow, W.S. To, C.K. Tang, B.Z and Kim, J.-K. 2007. Correlations between percolation threshold, dispersion state, and aspect ratio of carbon nanotubes. *Advanced Functional Materials*, 17, 3207-3215. (b) Y.S. Song and J.R. Youn. 2005. Constitutive Equations for Dilute Bubble Suspensions and Rheological Behavior in Simple Shear and Uniaxial Elongational Flow Fields. *Carbon,* 43, 1378-1385.

[5] (a) Florian H. Gojny, Jacek Nastalczyk, Zbigniew Roslaniec and Karl Schulte. 2003. Surface modified multi-walled carbon nanotubes in CNT/epoxy-composites. *Chemical Physics Letters,* 370, 820-824. (b) Ami Eitan, Kuiyang Jiang, Doug Dukes, Rodney Andrews, and Linda S. Schadler. 2003. Surface Modification of Multiwalled Carbon Nanotubes: Toward the Tailoring of the Interface in Polymer Composites. *Chemistry Materials*, 15, 3198–3201.

[6] (a) D. Qian, E. C. Dickey, R. Andrews and T. Rantell. 2000. Load transfer and deformation mechanisms in carbon nanotube-polystyrene composites. *Applied Physics Letters*, 76, 2868-2870. (b) Andrews, R. Jacques, D. Rao, A. M.; Rantell, T. Derbyshire, F. Chen, Y. Chen, J. and Haddon, R. C. 1999. Nanotube composite carbon fibers. *Applied Physics Letters,* 75, 1329–1331.

[7] (a) Ya-Ping Sun, Kefu Fu, Yi Lin and Weijie Huang. 2002. Functionalized Carbon Nanotubes: Properties and Applications. *Accounts of Chemical Research, 35*, 1096–1104. (b) Peng Cheng Ma, Jang-Kyo Kim and Ben Zhong Tang. 2007. Effects of silane functionalization on the properties of carbon nanotube/epoxy nanocomposites. *Composites Science and Technology,* 67, 2965-2972. (c) Yi Lin, Bing Zhou, K. A. Shiral Fernando, Ping Liu, Lawrence F. Allard, and Ya-Ping Sun. 2003. Polymeric Carbon Nanocomposites from Carbon Nanotubes Functionalized with Matrix Polymer. *Macromolecules,* 36, 7199–7204.

[8] (a) Weijie Huang, Yi Lin, Shelby Taylor, Jay Gaillard, Apparao M. Rao, and Ya-Ping Sun. 2002. Sonication-Assisted Functionalization and Solubilization of Carbon Nanotubes**.** *Nano Letters***,** 2, 231–234. (b) Kumar, S. Dang, T. D.; Arnold, F. E. Bhattacharyya, A. R. Min, B. G. Zhang, X. Vaia, R. A. Park, C. Adams, W. W. Hauge, R. H. Smalley, R. E. Ramesh, S. and Willis, P. A. 2002. Synthesis, Structure, and Properties of PBO/SWNT Composites. *Macromolecules,* 35, 9039–9043.

[9] Daniel A. Heller, Paul W. Barone and Michael S. Strano. 2005. Sonication-induced changes in chiral distribution: A complication in the use of single-walled carbon nanotube fluorescence for determining species distribution. 43, 651-653.

[10] (a) Belobrov PI, Bursill LA, Maslakov KI, Dementjev AP. 2003. Electron spectroscopy of nanodiamond surface states. *Applied Surface Science*, 215, 169-177. (b) C. Portet, G. Yushin, Y. Gogotsi. 2007. Electrochemical performance of carbon onions, nanodiamonds, carbon black and multiwalled nanotubes in electrical double layer capacitors. *Carbon*, 45, 2511-2518.

[11] Zhao DS, Zhao M, Jiang Q, Diam. 2002. Size and temperature dependence of nanodiamond-nanographite transition related with surface stress. *Diamond Related Meterials*, 11, 234-236.

[12] Bucak S, Jones, D. A, Laibinis P. E and Hatton T. A. 2003. Protein separations using colloidalmagnetic nanoparticles. *Biotechnology* , 19, 477-484.

[13] Faming Zhang, Jun Shen, Jianfei Sun, Yan Qiu Zhu, Gang Wang, G. McCartney. 2005. Conversion

of carbon nanotubes to diamond by spark plasma sintering. *Carbon*, 43, 1254-1258.

[14] Chunnian He, Naiqin Zhao, Chunsheng Shi, Xiwen Du, Jiajun Li, Lan Cui, Fei He. 2006. Carbon onion growth enhanced by nitrogen incorporation. *Scripta METERIALIA*, 54, 1739-1743.

[15] G.P. Bogatyreva, M.N. Voloshin, V.I. Padalko. 2008. Detonation synthesized nanodiamond powder for the preparation of porous polycrystalline micron powders. *Diamond and Related Materials*, 17, 213-216.

[16] E. Koudoumas a, O. Kokkinaki, M. Konstantaki, S. Couris, S. Korovin, P. Detkov, V. Kuznetsov, S. Pimenov, and V. Pustovoi. 2002. Onion-like carbon and diamond nanoparticles for optical limiting. *Chemical Physics Letters,* 357, 336-340.

[17] Lang Li, J.L. Davidson, Charles M. Lukehart. 2006. Surface functionalization of nanodiamond particles via atom transfer radical polymerization. *Carbon*, 44, 2308-2315.

[18] (a) Shenderova OA, Zhirnov VV, Brenner DW. 2002. Carbon nanostructures. *Crit Rev Solid State*, 27, 227–356. (b) Dolmatov VY, Burkat GK. 2000. Detonation synthesized ultradisperse diamonds as a basis for novel class of composite metal-diamond galvanic coatings. *Journal of Superhard Mater*ials, 1, 84–95. (c) Dolmatov VY, Kostrova LN. 2000. Shock wave-synthesized nanometric diamond and potentials for development of new generation of medicinal preparations. *Journal of Superhard Mater*ials, 3, 82–85.

[19] Jin-Shan Wang, Krzysztof Matyjaszewski. 1995. "Living"/Controlled Radical Polymerization. Transition-Metal-Catalyzed Atom Transfer Radical Polymerization in the Presence of a Conventional Radical Initiator. *Macromolecules*, 28, 7572-7573.

[20] A. Kru¨ger, F. Kataoka , M. Ozawa, T. Fujino, Y. Suzuki, A.E. Aleksenskii, A. Ya. Vul, and E Osawa. 2005. Unusually tight aggregation in detonation nanodiamond: Identification and disintegration. *Carbon*, 43, 1722-1730.

[21] (a) Masami Kamigaito, Tsuyoshi Ando, and Mitsuo Sawamoto. 2001. Metal-Catalyzed Living Radical Polymerization. *Chemical Reviews*, 101, 3689–3746. (b) Haifeng Gao and Krzysztof Matyjaszewski. 2006. Synthesis of Star Polymers by a Combination of ATRP and the “Click” Coupling Method. *Macromolecules,* 39, 4960–4965.

[22] Shuhui Qin, Dongqi Qin, Warren T. Ford, Daniel E. Resasco and Jose E. Herrera. 2004. Polymer Brushes on Single-Walled Carbon Nanotubes by Atom Transfer Radical Polymerization of n-Butyl Methacrylate. *Journal of the American Chemical Society***,** 126, 170-176.

[23] L. S. Cahill, Z. Yao, A. Adronov, J. Penner, K. R. Moonoosawmy, P. Kruse, and G. R. Goward. 2004. Polymer-Functionalized Carbon Nanotubes Investigated by Solid-State Nuclear Magnetic Resonance and Scanning Tunneling Microscopy. *Journal of Physical Chemistry B,*108, 11412–11420..

[24] Zhaoling Yao, Nadi Braidy, Gianluigi A. Botton, and Alex Adronov. 2003. Polymerization from the Surface of Single-Walled Carbon Nanotubes − Preparation and Characterization of Nanocomposites. *Journal of the American Chemical Society,* 125, 16015–16024.

[25] (a) Guoyong Xu1, Wei-TaiWu1, Yusong Wang1, Wenmin Pang1, PinghuaWang2, Qingren Zhu1,3 and Fei Lu1. 2006. Synthesis and characterization of water-soluble multiwalled carbon nanotubes grafted by a thermoresponsive polymer. *Nanotechnology*, 17**,** 2458–2465. (b) Shuhui Qin, Dongqi Qin, Warren T. Ford, Daniel E. Resasco, and Jose E. Herrera. 2004. Functionalization of Single-Walled Carbon Nanotubes with Polystyrene via Grafting to and Grafting from Methods. *Macromolecules,* 37, 752–7.

[26] Hao Kong, Wenwen Li, Chao Gao, Deyue Yan, Yizheng Jin, David R. M. Walton, and Harold W. Kroto. 2004. Poly(*N*-isopropylacrylamide)-Coated Carbon Nanotubes: Temperature-Sensitive Molecular Nanohybrids in Water. Macromolecules, 37, 6683-6686.

[27] Kiyoshi Tanemura, Tsuneo Suzuki,*a* Yoko Nishida, Koko Satsumabayashi and Takaaki Horaguchi. 2004. A mild and efficient procedure for a-bromination of ketones using N-bromosuccinimide catalysed by ammonium acetate. *Chemical communication*. 59, 470-471.

[28] M. V. Adhikari and S. D. Samant. 2002. Sonochemical bromination of acetophenones using *p*-toluenesulfonic acid–N-bromosuccinimide. *Ultrasonic Sonochemistry*, 9, 107-111.

[29] Samar Kumar Guha, Bo Wu, Beom Soo Kim, Woonphil Baik and Sangho Koo. 2006. TMS/OTf-Catalyzed *a*-bromination of carbonyl compounds by *N*-bromosuccinimide. *Tetrahedron Letters,* 47

291–293.

[30] Michael K. Georges, Richard P. N. Veregin, Peter M. Kazmaier, Gordon K. Hamer. 1993. Narrow molecular weight resins by a free-radical polymerization process. *Macromolecules*, 26 , 2987–2988.

[31] John Chiefari, Y. K. Chong, Frances Ercole, Julia Krstina, Justine Jeffery, Tam P. T. Le,Roshan T. A. Mayadunne, Gordon F. Meijs, Catherine L. Moad, Graeme Moad, Ezio Rizzardo, and San H. Thang. 1998. Living Free-Radical Polymerization by Reversible Addition-Fragmentation Chain Transfer: The RAFT Process. *Macromolecules, 31,* 5559-5562.

[32] (a) Wei Zhang, Xiulin Zhu, Zhenping Cheng, Jian Zhu. 2007. Atom Transfer Radical Polymerizations of Methyl Methacrylate and Styrene with an Iniferter Reagent as the Initiator. *Journal of Applied Polymer Science*, 106, 230–237. (b) E. Kroeze, B. de Boer, G. ten Brinke, and G. Hadziioannou. 1996. Synthesis of SAN-PB-SAN Triblock Copolymers via a "Living" Copolymerization with Macro-Photoiniferters. *Macromolecules,* 29, 8599–8605. (c) Jianzhong Du and Yongming Chen. 2004. Atom-Transfer Radical Polymerization of a Reactive Monomer: 3-(Trimethoxysilyl)propyl Methacrylate. *Macromolecules,* 37, 6322-6328.

[33] Baek, J.-B and Tan, L.-S. 2003. Improved Syntheses of Poly(oxy-1.3-phenylenecarbonyl-1,4-phenylene) and Related Poly(ether-ketones) Using Polyphosphoric Acid/P2O5 as Polymerization Medium. *Polymer*, 44, 4135-4147.

[34] H. Malz, H. Komber, D. Voigt, I. Hopfe and J. Pionteck. 1998. Synthesis of Functional polymers by atom transfer radical polymerization. *Macromolecular Chemistry And Physics,* 200, 642-651.

[35] (a) Ahn, S.-N. Lee, H.-J. Kim, B.-J. Tan, L.-S. and Baek, J.-B. 2008. Epoxy/amine-functionalized short length vapor-grown carbon nanofiber composites. *Journal of Polymer Science: Polymer Chemistry,* 46, 7473-7482 (b) Baek, J.-B. Lyons, C. B. and Tan, L.-S. 2004. Grafting of Vapor-Grown Carbon Nanofibers via In-Situ Polycondensation of 3-Phenoxybenzoic Acid in Polyphosphoric Acid. *Macromolecules,* 37, 8278-8285. (c) Oh, S.-J. Lee, H.-J. Keum, D.-K. Lee, S.-W. Park, S.-Y. Tan, L.-S. and Baek, J.-B. 2006. Multiwalled Carbon Nnanotubes and Nanofibers Grafted with Polyetherketones in Mild and Viscous Polymeric Acid. *Polymer*, 47, 1132-1140.

[36] http://www.sigmaaldrich.com/catalog/ProductDetail.do

[37] Anke Krueger. 2008. The structure and reactivity of nanoscale diamond. *Journal of Materials Chemistry*, 18, 1485–1492.

[38] C. Casiraghi, A. C. Ferrari, and J. Robertson. 2005. Raman spectroscopy of hydrogenated amorphous carbons. *PHYSICAL REVIEW B* 72, 085401-1 – 085401-14.

[39] S. Prawer , K.W. Nugent, D.N. Jamieson, J.O. Orwa, L.A. Bursill, J.L. Peng. 2000. The Raman spectrum of nanocrystalline diamond. *Chemical Physics Letters*, 332, 93-97.

[40] Sebastian Osswald, Gleb Yushin, Vadym Mochalin, Sergei O. Kucheyev, and Yury Gogotsi. 2006. Control of sp2/sp3 Carbon Ratio and Surface Chemistry of Nanodiamond Powders by Selective Oxidation in Air. *American Chemical Society*, 128, 11635-11642.

[41] http://www.lasurface.com/database/elementxps.php

[42] Yuan Gao, Xueping Gao, Yongfeng Zhou and Deyue Yan. 2008. Preparation of poly(methyl methacrylate) grafted titanate nanotubes by *in situ* atom transfer radical polymerization. *Nanotechnology*, 19, 495604-495613.

[43] Han, S.-W.; Oh, S.-J.; Tan, L.-S.; Baek, J.-B. 2008. One-Pot purification and functionalization of single-walled carbon nanotubes in less-corrosive poly(phosphoric acid). *Carbon*, 46, 1841-1849.

[44] H. Althues, R. Palkovits, A. Rumplecker, P. Simon, W. Sigle, M. Bredol,U. Kynast, and S. Kaskel. 2006. Synthesis and Characterization of Transparent Luminescent ZnS:Mn/PMMA Nanocomposites. *American Chemical Society, 18,* 1068-1072.

[45] Jong Hyun Park and Sadhan C. Jana. 2003. The relationship between nano- and micro-structures and mechanical properties in PMMA–epoxy–nanoclay composites. *Polymer,* 44, 2091–2100.

[Appendix]

Purification of Carbon nanonion and Diamond nanoparticle.

Introduction

Carbon nanomaterials have received a great deal of attention since the discovery of the C_{60} fullerene molecule and the carbon nanotube. Three-dimensional, carbon based, nano-structures materials are generally various : (i) fullerene (0.7 ~ 3nm) ;(ii)carbon nanopowders (≤30nm) ;(iii)diamond nanopowders (3.2nm). In 1992 Ugarte, while examining carbon nanoparticles filled with gold and lanthanum oxide found fascinating particles consisting of concentric graphite-like shells. So, these particles were called carbon onion or carbon nanopowder. Carbon nanopowders (CNP) such as fullerenes have good electrochemical and photophysical properties. Also diamond nanopowders (DNP) are worth of investigating due to the unique properties, such as highest hardness, highest thermal conductivity, low thermal expansion coefficient, and low friction coefficient. CNP can be produced from different carbon materialsvia arc discharge, plasma chemical deposition (CVD) and shock wave treatment of carbon soot. and diamond nanopowders (DNP) were produced CVD (Chemical Vapor Deposition), detonation and spark plasma sintering method. In producing CNP and DNP, Metal catalysts are generally necessary to activate materials. (CNP: ≥99% trace metals basis, DNP: ≥95% trace metals basis.) In consequence, all CNT and DNP product from those method in could impurities such as metal catalyst particles, amorphous carbon and carbon nanoparticles. Therefore, CNP and DNP may find their limited use for some applications as they contain a small fraction of metal catalyst. Lately, many purified method have been investigated and have been used successfully to remove impurities from carbon soot. For example, there are oxidation, thermal annealing, thermal oxidation, ultra-sonication, a strong acid treatments and so on… Recently, in my Lab., the less destructive chemical modification and to minimize the surface damages of various carbon nanomaterials via electrophilic substitution reaction in a mild polyphosphoric acid (PPA)/phosphorous pentoxide (P_2O_5) medium has been developed. By using the method, We tried to purify the as-received CNP and DNP in PPA/ P_2O_5 to remove like a metallic impurities.

Purification procedure of Carbon nanoparticle & Diamond nanoparticle.

Into a 100mL three-necked, round-bottom resin flask equipped with a high torque mechanical stirrer, and nitrogen inlet and outlet, CNP or DNP (0.5g), PPA (83% assay, 10g) and P_2O_5 (2.5g) were placed and stirred with dried nitrogen purging at 80°C for 1h. The reaction mixture was heated at 100 °C for 1h and then it was heated and maintained at 130 °C for 72h. After cooled down, water was added into the mixture. The precipitates were collected by suction filtration, Soxhlet extracted with water for three days and then methanol for three days. The product was finally freeze dried for 24h to give black and dark gray powder, repectively.Anal. Found for CNP: C, 92.56%; H, 0.33%; N, 0.22%. P-CNP: C, 91.21%; H, 0.50%; N, 0.19%. DNP: C, 85.58%; H, 1.22%; N, 2.06%. P-DNP: C, 85.44%; H, 1.61%; N, 1.89%.

Results and Discussion

Purification of CNP & DNP.

As shown in Scheme 1, Purification of CNP and DNP are carried out following the literature procedure.

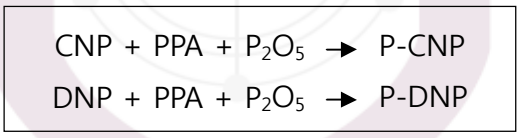

Scheme 1. Purification of CNP & DNP.

FT-IR spectra.

The progress of the reaction was conveniently monitored with FT-IR. All sample showed sp^3 C-H peak at 2921 cm^{-1} ~ 2923 cm^{-1} and C=O peak at 1593 cm^{-1} ~ 1633 cm^{-1}. We knows that CNP and DNP were preserved original structure of them via purification procedure

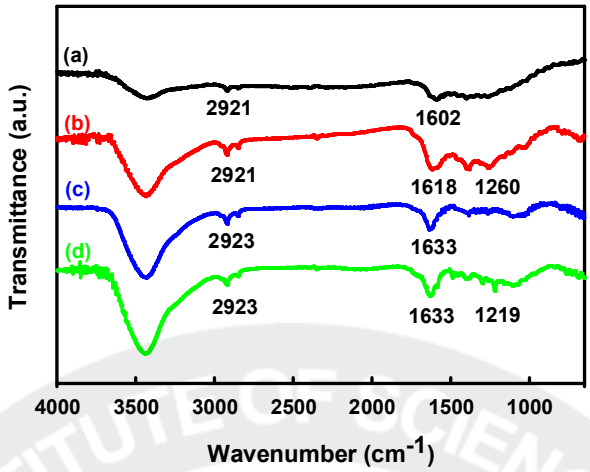

Figure 1. FT-IR (KBr pellet) spectra of samples. (a) CNP; (b) P-CNP; (c) DNP; (d) P-DNP.

Scanning Electron Microscopy (SEM).

For the comparison purpose, the SEM image of pristine CNP, DNP are presented (Figure 2a, 3c). It shows that the surfaces are slightly rough and be not uniform. But the surfaces of purificated P-CNP, P-DNP are clearly smooth and seamless surfaces.(Figure 2b, 4d).

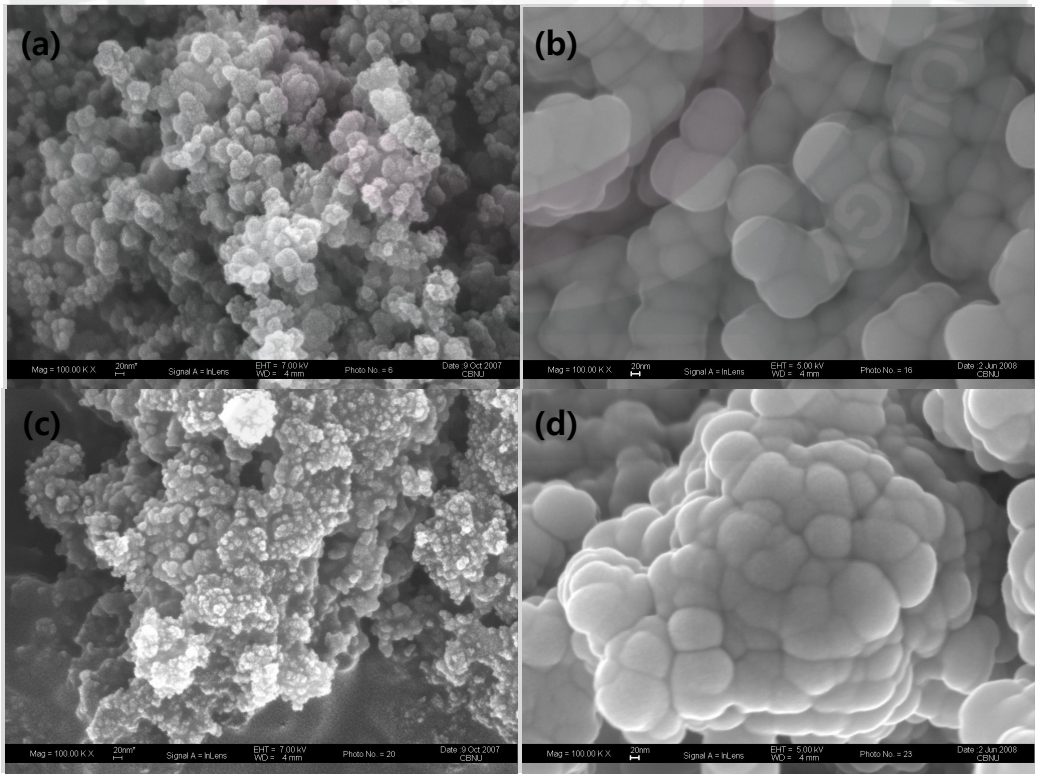

Figure 2. SEM images: (a) as-received CNP (100,000x); (b) P-CNP (100,000x); (c) as-received

DNP (100,000x); (d) P-DNP (100,000x).

Thermal Properties.

The TGA graphs of raw samples and purified CNP & DNP. Figure 3(a) shows the TGA of as-received CNP and purified CNP indicated that the temperatures at which 5% weight loss *($T_{d5\%}$)* occurred were at 655 and 657 °C in air, and then the weight sharply decreases. As-received CNP was completely evaporated at 813 °C. Figure 3(b) shows the TGA of as-received DNP and purified DNP indicated that the temperatures at which 5% weight loss *($T_{d5\%}$)* occurred were at 602 and 606 °C in air. And to conclude purified samples have a better thermal stability than as-receive samples.

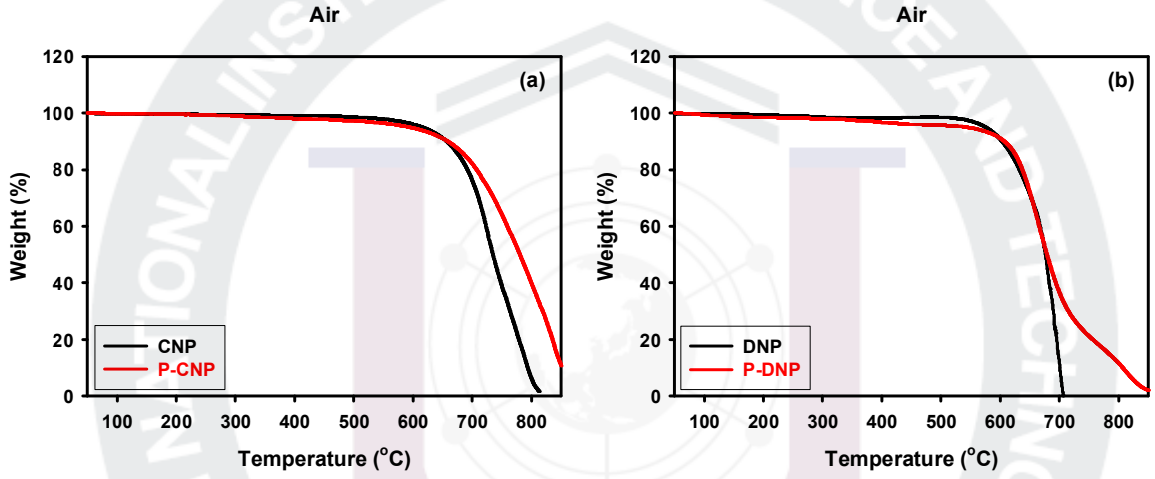

Figure 3. TGA thermograms obtained with heating rate of 10℃/min: (a) CNP & P-CNP (b) DNP & P-DNP.

X-ray Photoelectron Spectroscope (XPS).

Figure 4 (a) and (b) shows XPS C 1s spectra of pristine CNP and P-CNP. The C 1s peak at 284.1 eV, 286 eV, and 287.6 eV was observed for C (graphite), C (non combine), and C (combine avec oxygene), respectively. After purification, at 286 eV peak was remarkably increaser than before. The results show that the CNP's purity was increase due to remove impurities of surrounding carbon atoms. Figure 4(c) and (d) shows XPS C 1s spectra of pristine DNP and P-DNP. Above all things, at 290.45 eV, Diamante (DIA) peak was significantly increased. Therefore, pristine CNP and DNP were successfully purified to P-CNP, P-DNP

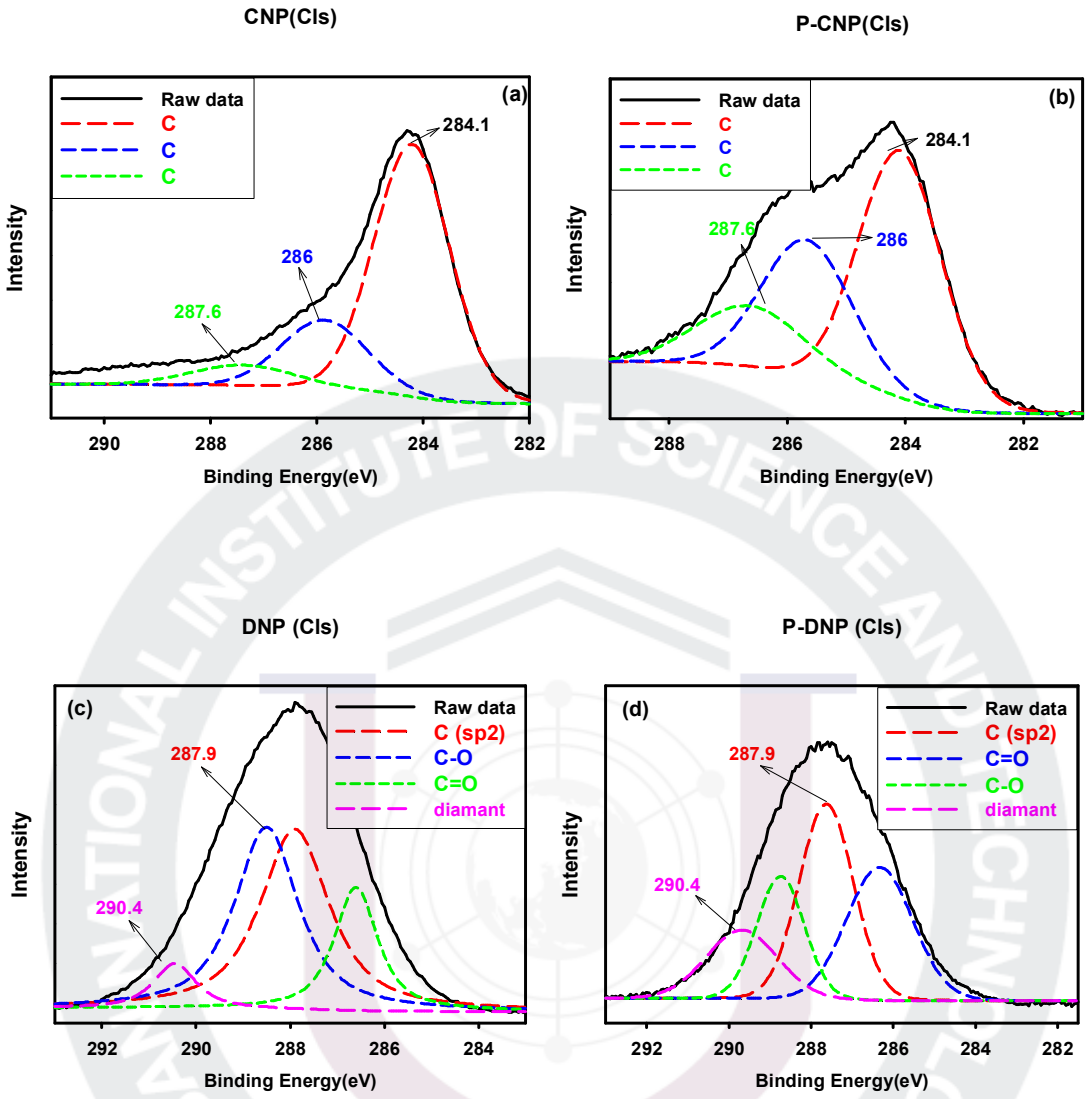

Figure 4. XPS C 1s Spectra : (a) as-received CNP; (b) P-CNP;(c) as-received DNP; (d) P-DNP.

Wide-Angle X-Ray Diffraction (WAXS).

The X-ray diffraction patterns of CNP and P-CNP were shown in Figure 5(a). The *d*-spacing values are 3.72, 2.95, 2.54, 2.01, 1.79, and 1.53 nm in that order. CNP and P-CNP peak were nearly similar with intensity, but there are exists a little shift. The X-ray diffraction patterns of DNP and P-DNP were shown in Figure 5 (b). The *d*-spacing values are 2.95, 2.55, 2.07, 1.80, 1.53, and 1.26 nm in that order. The peak at 2.07 Å was related to carbon atoms distance of diamond nanopowders. In P-DNP, this peak was remarkably stronger than before. As expected, this reflects the higher purity of DNP.

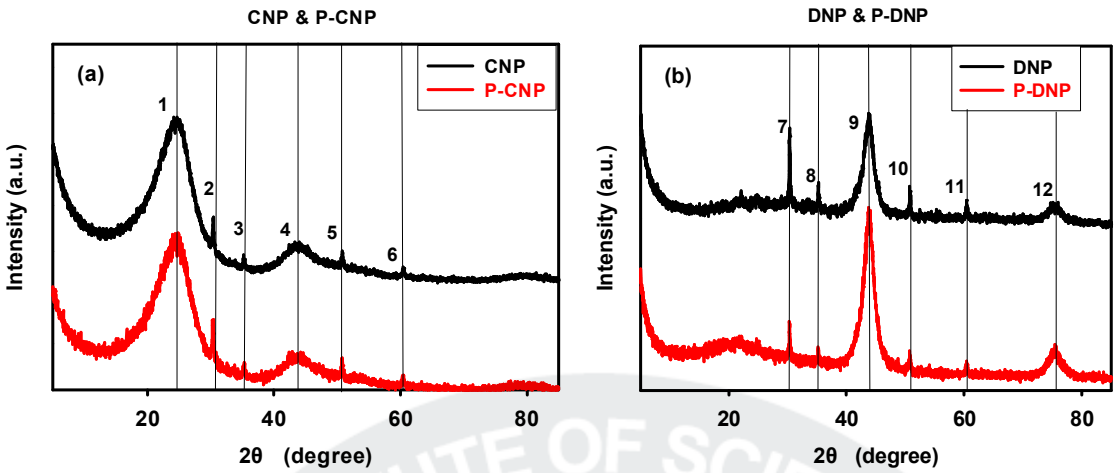

Figure5. WAXS patterns: (a) CNP and P-CNP; (b) DNP and P-DNP.

Surface Area.

Changes of surface area after purification procedure were evaluated by BET. CNP and P-CNP were very similar values. However, after purification, surface area of P-DNP were slightly decrease.

Table 1. Surface Area of samples

	CNP	P-CNP	DNP	P-DNP
Surface Area	112.89	114.12	262.14	234.678

(m^2/g)

Conclusion

We confirmed purification of CNP & DNP with FT-IR, X-Ray photoelectron Spectroscopy (XPS), X-ray Diffraction (XRD), and thermogravimetric analysis (TGA). As a result, we conducted successfully that purification of CNP and DNP in a mild and non-destructive medium, PPA/P_2O_5. Although it was not clear that the process is an ultimate purification method, it was efficient enough to remove persisting impurities like metals. Morphology clearly difference between pristine CNP & DNP and purified CNP & DNP was confirmed by scanning electron microscopy (SEM).

Purification and Functionalization of Diamond Nanoparticles in Polyphosphoric acid/Phosphorus Pentoxide

Introduction

Since their discovery, carbon nanomaterials have attracted great attention from many research groups worldwide due to their unique chemical and physical properties. And they have a high potential for many technological application. Also, They have various structures such as fullerene (0.7~3nm), carbon nanopowders (≤30nm) and diamond nanopowders (≤10nm), etc. Among the great nanocomposites, In particular, Diamond nanopowders (DNPs) are worth of investigating due to the unique properties such as ultimate hardness, highest thermal conductivity, lowest thermal expansion coefficient, and least friction coefficient. So, for more than 20 years a lot has been published regarding the development of production technologies of nanodiamond. An efficient commercial technology of nanodiamond synthesis by detonation of oxygen-deficient explosives and ultradisperseddiamond powders of nanosizes has been developed in Ukraine. Other methods are nanospray combustion process, spark plasma sintering, etc. For produce DNPs, metal catalysts are generally necessary to activate materials. So that reason, the raw DNPs obtained include nanodiamond particles, non-diamond carbon, as well as metals, metal oxides and other impurities. Recently, many purified methods have been investigated and have been used to remove impurities from carbon soot. But they have some problems. For example, Liquid phase purification is not an environmentally friendly process and requires expensive corrosion-resistant equipment. Oxidation purification and ozone-enriched air oxidation are also requires the use of either toxic or aggressive substances or supplementary catalysts which result an additional contamination or a significant loss of the diamond phase. As a result, it is probably difficult that Diamond nanopowders (DNPs) preserve property and shape because of thermal annealing, strong acid treatment and ultra-sonication, etc., Therefore, DNPs may find their limited use for some application. To solve this issue, we recently developed that non-destructive purification method via in a mild polyphosphoric acid (PPA)/phosphorous pentoxide (P_2O_5).

Our previous work on the successful grafting of various polymers onto carbon nanomaterials like a CNTs, CNF, Fullerene, etc. was reported. Therefore, for comparison, we also carried out the chemical modification of pristine DNPs and purified DNPs (PDNP) with 4-(2,4,6-trimethylphenoxy)benzamide (TMPBA) to afford TMPBA-g-DNP and TMPAB-g-PDNP to compare with PPA-treatment before and after Although PPA-treatment was not clear that it was an ultimate purification method, we present that is efficient enough to remove persisting impurities. The resultant purified nanocomposites were expected to display enhanced crystallinity. Furthermore, their morphology and some properties were investigated.

2. Experimental

2.1 Materials

All reagents, solvents and diamond nanopowders (DNPs, ≥95% trace metals basis) were purchased from Aldrich Chemical Inc. and used as received, unless otherwise mentioned.

2.2 Instrumentation

Infrared (IR) spectra were recorded on Jasco FT-IR 480 Plus spectrophotometer. Solid samples were imbedded in KBr disks. Elemental analyses (EA) were performed by system support at CBNU with a CE Instruments EA1110. Thermogravimetric analysis (TGA) was conducted air atmospheres with a heating rate of 10 °C/min using a Perkin-Elmer TGA 7. The field emission scanning electron microscopy (FE-SEM) used in this work was LEO 1530FE. The Brunauer-Emmett-Teller (BET) surface area was measured by nitrogen adsorption-desorption isotherms using Micromeritics ASAP 2504N. Wide-angle X-ray diffraction (WAXD) powder patterns were recorded with a Rigaku RU-200 diffractometer using Ni-filtered Cu Kα radiation (40 kV, 100 mA, λ = 0.15418 nm). X-ray photoelectron spectroscopy (XPS) was recorded on ESCALAB 210 with Mg Kα source. UV-vis spectra were obtained on a Perkin-Elmer Lambda 35 UV-vis spectrometer. Stock solutions were prepared by dissolving 1 mg of each sample in 8mL of *N*-methyl-2-pyrrolidone (NMP). Photoluminescence measurements were performed with a Perkin-Elmer LS 55 Fluorescence spectrometer. The excitation wavelength was that of the UV absorption maximum of each sample.

2.3 Purification of DNPs in PPA/P_2O_5

Into a 100mL resin flask equipped with a high torque mechanical stirrer, nitrogen inlet and outlet, DNPs (1g), PPA (83% P_2O_5 assay; 10g), and phosphorus pentoxide (P_2O_5, 5g) were placed and stirred under dry nitrogen purge at 130℃ for 72h. After cooling down to room temperature, water was added to the reaction mixture. The resulting precipitate was collected and Soxhlet extracted with water for three days, and then with methanol for three days. Finally, the PPA-treated DNPs (PDNP) were freeze-dried under reduced pressure (0.5mm Hg) for 24h to afford 0.92 g (92% yield) of a black powder.

2.4 4-(2,4,6-Trimethylphenoxy)benzamide

4-(2,4,6-Trimethylphenoxy)benzonitrile (49.8 g, 0.21 mol) and phosphoric acid (190 g) were placed in a 250 mL three-necked roundbottomed flask equipped with a magnetic stir-bar, nitrogen inlet, and a condenser. The reaction mixture was then heated at 120°C for 22 h. During this time, the benzamide product crystallized out of the reaction mixture. The crystals were collected by suction filtration, air-dried, dissolved in warm ethanol, and filtered. The filtrate was allowed to cool to room temperature to afford 37.0 g (69% yield) of white crystal

2.5 Functionalization of DNPs with 4-(2,4,6-trimethylphenoxy)benzamide in PPA/P_2O_5 at 130℃ (TMPBA-g-DNP)

Into a 100mL resin flask equipped with a high torque mechanical stirrer, nitrogen inlet and outlet, TMPBA (0.5g), DNPs (0.5g), PPA (83% P_2O_5 assay; 20g), and phosphorus pentoxide (P_2O_5, 5g) were placed and stirred under dry nitrogen purge at 130℃ for 72h. After cooling down to room temperature, water was added to the reaction mixture. The resulting precipitate was collected and Soxhlet extracted with water for three days, and then with methanol for three days. Finally, the resultant powder was freeze-dried under reduced pressure (0.5mm Hg) for 24h to afford to 0.84 g (86 % yield) of a gray powder.

2.6 Functionalization of PDNP with 4-(2,4,6-trimethylphenoxy)benzamide in PPA/P_2O_5 at 130℃ (TMPBA-g-PDNP)

Into a 100mL resin flask equipped with a high torque mechanical stirrer, nitrogen inlet and outlet, TMPBA (0.5g), PDNPs (0.5g), PPA (83% P_2O_5 assay; 20g), and phosphorus pentoxide (P_2O_5, 5g)

were placed and stirred under dry nitrogen purge at 130℃ for 72h. After cooling down to room temperature, water was added to the reaction mixture. The resulting precipitate was collected and Soxhlet extracted with water for three days, and then with methanol for three days. Finally, the resultant powder was freeze-dried under reduced pressure (o.5mm Hg) for 24h to afford to 0.74 g (77 % yield) of a dark-gray powder.

3. Results and Discussion

Previously, we have reported about purification of SWNTs (single-wall nanotubes) and also functionalization of MWNT, SWNT, VGCNF via Friedel-Crafts reaction in polyphosphoric acid (PPA). In this study, we used as-received DNPs (≤10nm) by nanospray combustion process from SIGMA-ALDRICH. As you know, DNPs by combustion, detonation, arc-discharge method include nanodiamond powders, non-diamond carbon, as well as metals, metal oxides and other impurities. To remove like a impurities, we tried to purify the DNPs in polyphosphoric acid (PPA)/phosphorus pentoxide (P_2O_5) (Figure 1a) and we also carried out the chemical modification of pristine DNPs and purified DNPs (PDNP) with 4-(2,4,6-trimethylphenoxy)benzamide (TMPBA) to afford TMPBA-g-DNP and TMPAB-g-PDNP (Figure 1b,1c). In the beginning, the color of mixtures was dark gray due to PDNPs. After 2h at 130℃, the color of the reaction mixture became light yellow indicating that TMPBA were grafted to DNPs and thus, homogeneously dispersed in the reaction medium (Figure 1c). DNPs have never been isolated in pure form (>99.9% carbon). Elemental analysis of the pristine DNPs has revealed significant presence of heteroatoms (H, N, O) in addition to carbon. The samples show relatively larger discrepancies of carbon content between theoretical and experimental values in elemental analysis (Table 1). This was presumably due to the low carbon content of as-received DNPs.

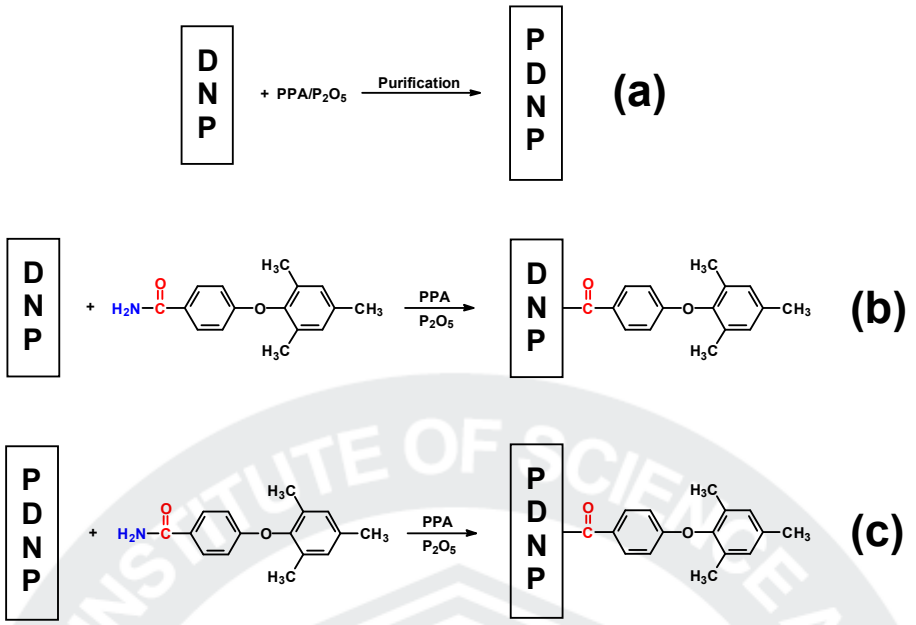

Figure 1. (a) Purification of DNPs (PDNP); (b) Functionalization of DNPs (TMPBA-g-DNP); (c) Functionalization of PDNPs (TMPBA-g-PDNP)

3.1 FT-IR Study

The FT-IR spectrum of pristine DNPs (Figure 2a) show the weak sp^3C-H band stretching at 2921cm^{-1}, C=O band stretching at 1630 cm^{-1}. After PPA-treated DNPs, Figure 2b shows that maintained original framework during purification procedure. Furthermore, C-O band stretching at 1159cm^{-1}, 1089cm^{-1} are sharper and larger than pristine DNPs peaks. It is probably describes that hidden peaks come out via purification process. We are also verified successful functionalization of DNPs and PDNP, respectively with TMPBA via FT-IR (Figure 2c, 2d). After modified, N-H (amide) band stretching at 3385cm^{-1} and 3210cm^{-1} and C=O (aromatic carbonyl) band stretching at 1642cm^{-1} disappeared (Figure 2e), and newly C=O (aromatic ketone) peak appears at 1662cm^{-1} (Figure 2c), 1655cm^{-1} (Figure 2d), respectively.

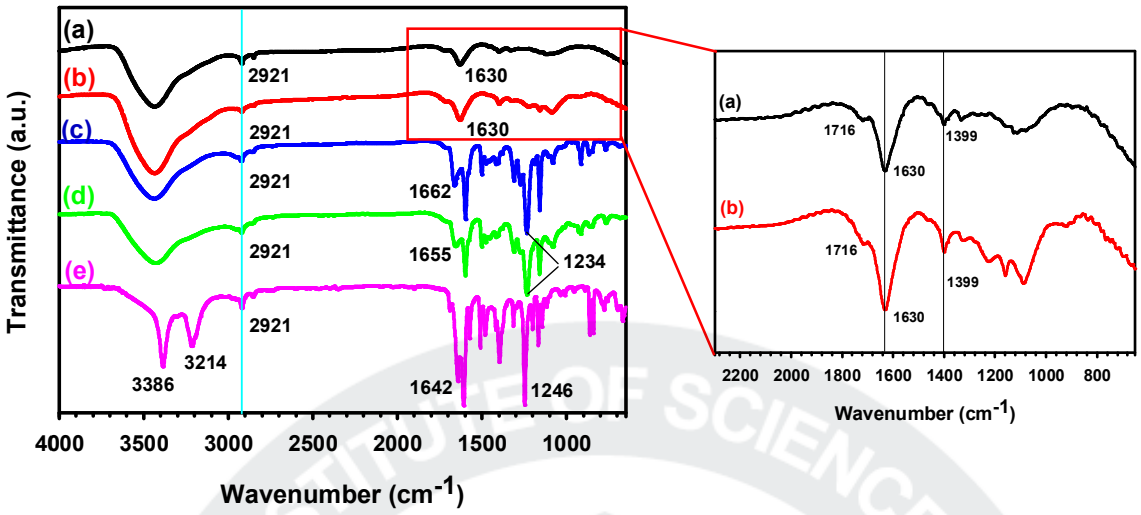

Figure 2. FT-IR (KBr pellet) spectra of samples: (a) DNPs; (b) PDNP; (c) TMPBA-g-DNP; (d) TMPBA-g-PDNP (e) 4-(2,4,6-trimethylphenoxy)benzamide (TMPBA).

3.2 Scanning Electron Microscopy (SEM)

The SEM images of pristine DNPs and TMPBA-g-DNP shows that the surface texture of sample consisted as aggregates and agglutinates even though after modified (Figure 3). Crystalline spherical diamond particle shape (≤10nm) is not clearly appear due to attached impurities. Namely, it is fairly difficult to discern a boundary between crystalline spherical diamond particle and monomer. But Figure 5a shows that the surface texture of PDNP fairly displayed more smooth and uniform than before PPA-treatment. Furthermore, Crystalline spherical diamond particles bigger than before, this result shows that diamond particles are gather flock to lump by covalent bond during impurities are removed. Figure 4-d shows definitely that diamond particles are persists originally shape.

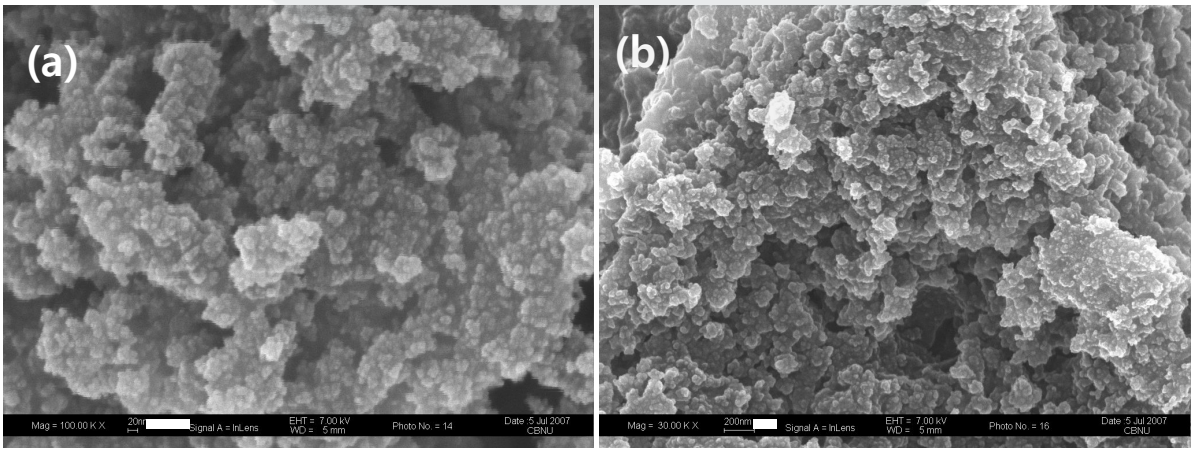

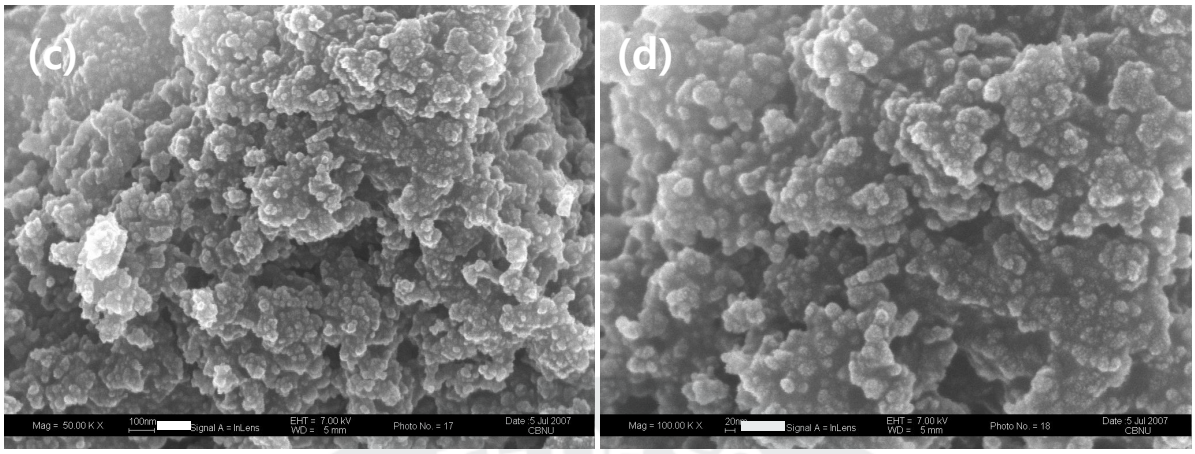

Figure 3. SEM images of (a) DNPs (100,000×); (b) TMPBA-g-DNP (30,000×); (c) TMPBA-g-DNP (50,000×); (d) TMPBA-g-DNP (100,000×). Scale bars are: 100 nm

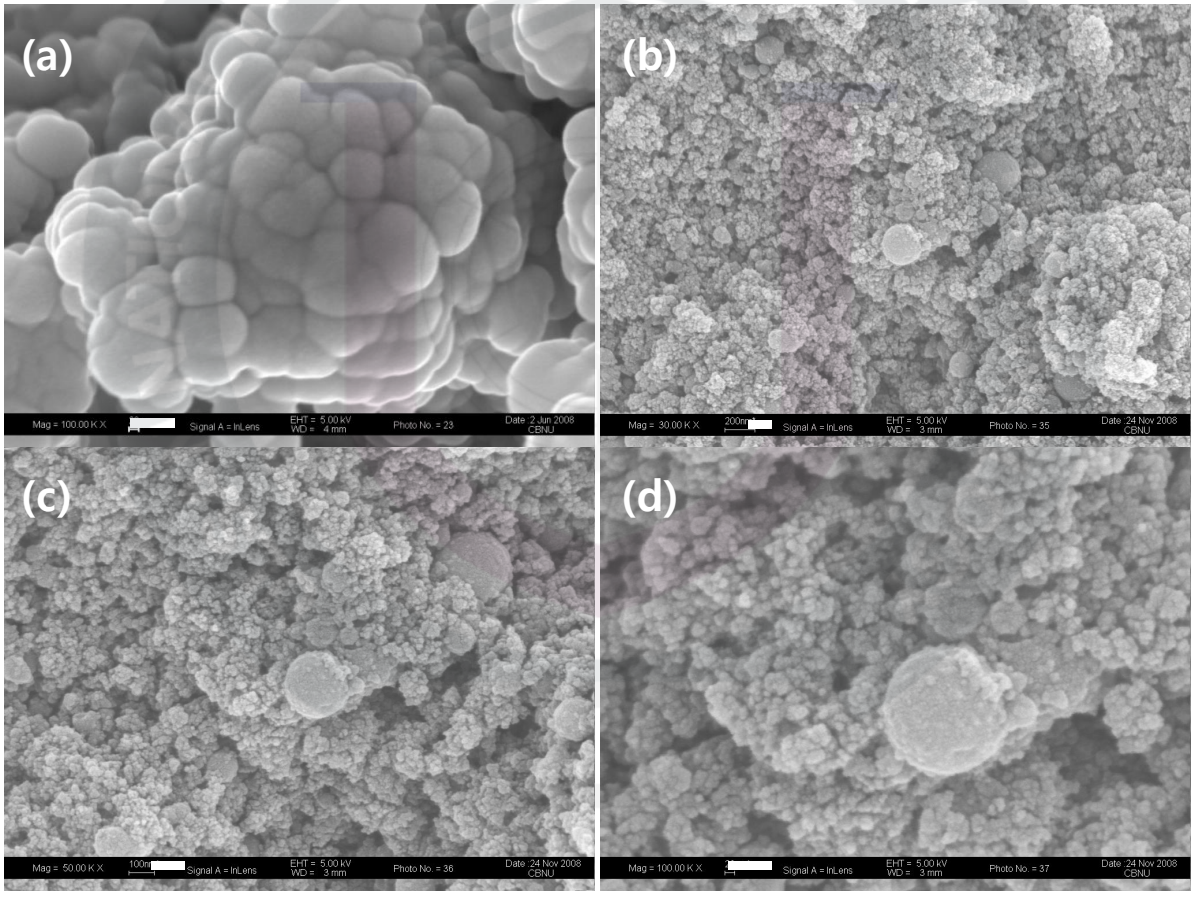

Figure 4. SEM images of (a) PDNP (100,000×); (b) TMPBA-g-PDNP(30,000×); (c) TMPBA-g-PDNP (50,000×); (d) TMPBA-g-PDNP (100,000×). Scale bars are: 100 nm.

3.3 Wide-Angle X-ray Diffraction (WAXD).

To monitor degree of crystallization and purity after PPA treatment, XRD scattering patterns were obtained powder samples without applied strain. The XRD pattern of the as-received DNPs show that the intensity of the characteristic diamond *d*-spacing (111) at 2.07 Å and *d*-spacing (220) at 1.26 Å as well as appears impure peaks at 2θ's =30.29, 35.17, 50.71, and 60.35° respectively (Figure 5a). On the other hand, the XRD pattern of the PDNP suggests that the characteristic diamond *d*-spacing (111) at 2.07 Å noticeably stronger and impure peaks fairly weaker than DNPs peaks (Figure 5a). Interestingly, we also know that PPA is non-destructed medium through figure 5b. While the XRD pattern of TMPBA-g-PDNP shows still perfect characteristic diamond *d*-spacing (111) and (220), the XRD pattern of TMPBA-g-DNP disappears characteristic diamond *d*-spacing (220) as well as remarkable decrease characteristic diamond *d*-spacing (110).

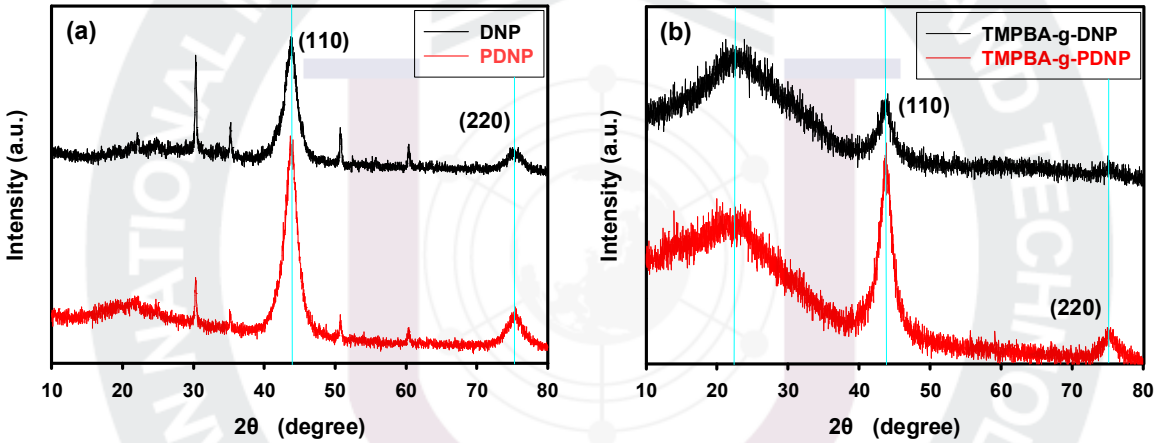

Figure 5. XRD patterns of samples: (a) DNPs and PDNP; (b) TMPBA-g-DNP and TMPBA-g-PDNP.

3.4 Surface area.

The BET surface areas of DNPs, PDNP, TMPBA-g-DNP and TMPBA-g-PDNP were 262.14, 234.67, 212.38 and 196.10 m^2/g, respectively. The surface area of PDNP was decreased approximately 11%, and The Pore volume of PDNP was decreased about 20% than DNPs which implied that PDNP should be more compact morphology due to higher crystallinity due to purification. Furthermore, the surface area of TMPBA-g-DNP was decrease approximately 19% than DNPs, also followed a certain trend between TMPBA-g-PDNP and PDNP. Together with FT-IR, WAXD and SEM results (see Figure 2, Figure 4a and Figure 5a), this result further supported that PPA played as both grafting and purifying. Table 2 shows that the pore size decreased after PPA-treatment but it was slightly increased after modification.

Table 2. BET surface area, micropore volume and average pore of samples.

	Surface Area (m^2/g)	Micorpore volume (ml/g)	Pore Size (Å)
DNP	262.14	1.12	171.14
PDNP	234.67	0.89	152.86
TMPBA-g-DNP	212.38	0.98	186.14
TMPBA-g-PDNP	196.10	0.76	156.71

3.5 UV-vis Absorption

UV-vis absorption and emission measurements were conducted to have information of interfacial interaction between TMPBA and DNP. Stock solution (0.01mol/L) of each sample was prepared in NMP. The UV-absorption of DNP and PDNP showed sharp peak at 259 nm (Figure 6a). And The UV-absorption of TMPBA-g-DNP and TMPBA-g-PDNP showed relatively broad peak at 284 nm. This implied that TMPBA should be successfully grafted onto the surface of DNP and PDNP, respectively. As can be seen, DNPs exhibit larger absorbance than PDNP (Figure 6a), due to taking into account the amorphous carbon electronic model. Reversibly, Figure 6b shows that TMPBA-g-PDNP exhibit lager absorbance than TMPBA-g-DNP. It's probably implied that double bond in TMPBA is more nicely show up during removed amorphous carbon. Fluorescent measurements were also conducted. The applied excitation wavelength was UV absorption maximum of each sample. The emission maxima of DNP and PDNP were at 369 and 392 nm, respectively. And the emission maxima of TMPBA-g-DNP and TMPBA-g-PDNP were at 446 and 480 nm, respectively.

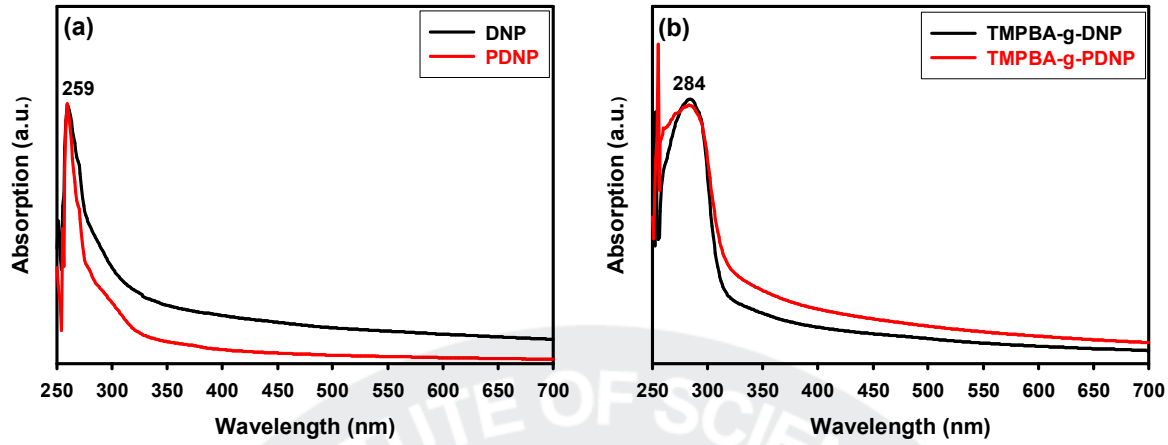

Figure 6. UV-Vis absorption spectra of samples: (a) DNPs and PDNP; (b) TMPBA-g-DNP and TMPBA-g-PDNP.

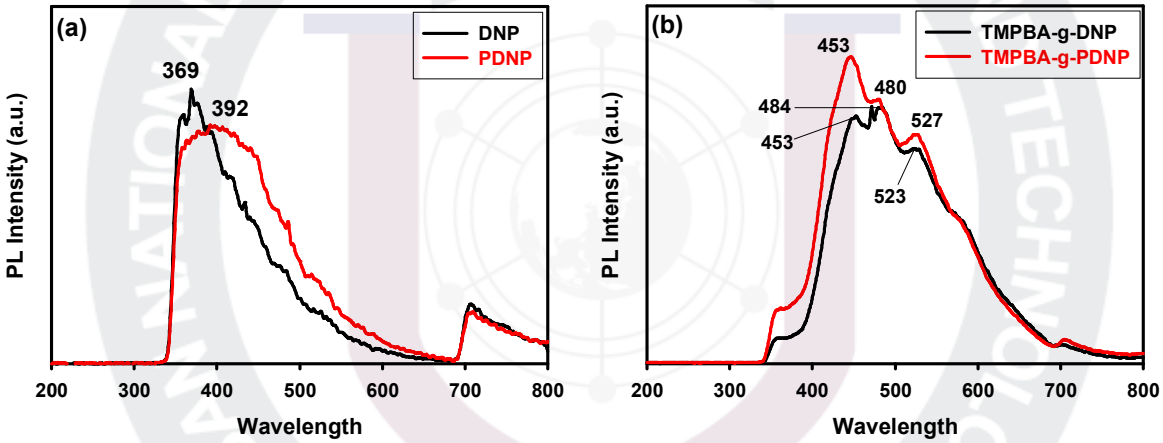

Figure 7.UV-Vis emission spectra of samples: (a) DNPs and PDNP; (b) TMPBA-g-DNP and TMPBA-g-PDNP.

3.6 XPS (X-ray photoelectron spectroscopy) ; C1s

The XPS spectra of the DNPs, PDNP, TMPBA, TMPBA-g-DNP, and TMPBA-g-PDNP were also measured (Figure 9, 10). The peak 287.8, 286.6, and 284.5eV was observed as shown in Figure 9 and the peak 287.4, 285, and 284.5eV was observed as shown in Figure 10. The center peak 287.8eV of DNPs is not correctly identity with PDNPs center peak 287.4eV due to probably oxidation by PPA (Figure 10). And the 284.5eV peak of TMPBA describes diphenylether. Interestingly, the peak position of TMPBA-g-DNP and TMPBA-g-PDNP were strikingly different (Figure 9, 10). While the TMPBA-g-DNP center peak (Figure 9) observed ambiguous data such as C-O, C=C, etc. at 286.6eV,

the TMPBA-g-PDNP center peak (Figure 10) appeared diamond peak at 285eV. These results suggest that TMPBA-g-PDNP has more desirable result as expected than TMPBA-g-DNP.

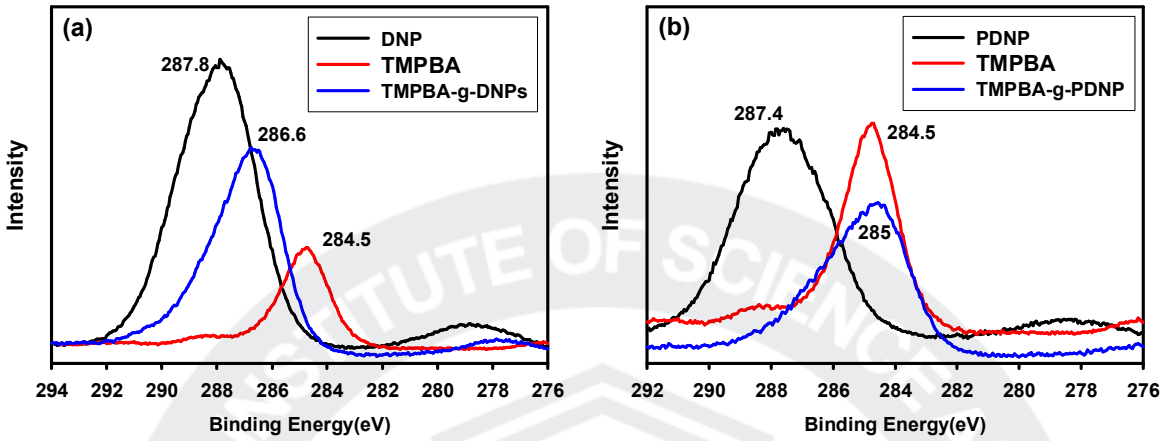

Figure 8: X-ray photoelectron spectroscopy: (a) DNPs, TMPBA and TMPBA-g-DNP; (b) PDNP, TMPBA and TMPBA-g-PDNP.

3.7 Thermal Properties

The samples were subject to thermogravimetric analysis (TGA) with heating rate of 10 °C/min in air. The PDNP are thermally more stable towards oxidative destruction than pristine DNPs. It is probably due to the removal of some inorganic impurities from the pristine DNPs during PPA treatment. This point out that PPA-treated purification method does not introduce carboxyl, aldehyde and other oxygen-containing functional groups on the surface. The DNPs, PDNP, TMPBA-g-DNP and TMPBA-g-PDNP showed that the temperature at which 5% weight loss ($T_{d5\%}$) in air was occurred at 578, 562, 411 and 468 °C, respectively. The char yield of pristine DNPs at 850 °C was ~0 %, while PDNP had the values approached to 5.15 %. Also, although char yield of TMPBA-g-DNP at 850 °C was ~0.80 %, PDNP had the values approached to 8.15 % (Table 1). Surprisingly, Inner shell is presumably not completely burn because PDNPs and TMPBA-g-PDNP have larger crystalline carbon particles than pristine DNPs during PPA treatment process (Figure 9). For this reason, Figure 9 shows that TMPBA-g-PDNP were also more thermal stability than TMPBA-g-DNPs.

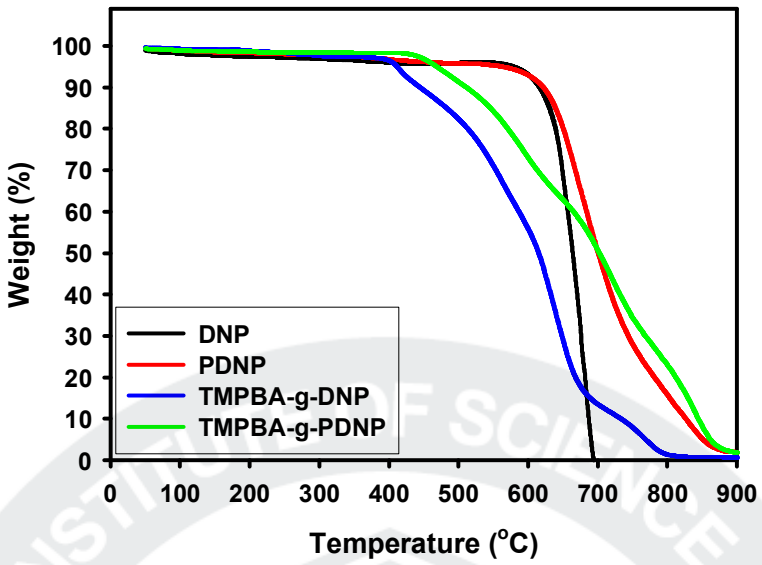

Figure 9. TGA thermograms obtained with heating rate of 10 °C/min in air.

Table 1. Thermogravimetric (TGA) and elemental analysis (EA) data of samples

Sample	TGA (in air)		Elemental Analysis			
	$T_{d5\%}$[a] (°C)	char[b] (%)		C (%)	H (%)	N (%)
DNP	578	~0	Calcd.	100	0.00	0.00
			Found	85.58	1.22	2.05
PDNP	562	5.15	Calcd.	100	0.00	0.00
			Found	85.44	1.61	1.89
TMPBA-g-DNP	411	0.80	Calcd.	89.71	3.30	0.00
			Found	83.58	3.06	1.36
TMPBA-g-PDNP	468	8.15	Calcd.	89.71	3.30	0.00
			Found	79.90	2.85	1.31

[a] The temperature at which 5% weight loss ($T_{d5\%}$) occurred on TGA thermogram obtained with heating rate of 10 °C/min.
[b] Char yield at 850°C.

4. Conclusion

We successfully developed a efficient and non-damage purification method by PPA-treatment and then, to make a comparative study also, carried out the chemical modification of pristine DNPs and purified DNPs (PDNP) with 4-(2,4,6-trimethylphenoxy)benzamide (TMPBA) to afford TMPBA-g-DNP and TMPAB-g-PDNP. The wide-angle X-ray diffraction (XRD) showed that the intensity of PDNP was fairly increased compared to that of pristine DNPs at 2.07 Å where *d*-spacing (111) of diamonds was characteristic. The morphologies of TMPBA-g-DNP and TMPAB-g-PDNP from scanning electron microscopy (SEM) were further affirmed the feasibility of chemical modification. And X-ray photoelectron spectroscopy (XPS) described that TMPBA-g-PDNP had a diamonds and diphenylether chemical bond energy at once. The results suggested that the reaction condition is indeed viable for the one-pot purification and functionalization of DNPs.

Carboxylic Acid-Terminated Hyperbranched Polybenzoxazole and Its Polyarm-Star Block Copolymers

Jong-Kwan Lim,[†] In-Yup Jeon,[†] Christopher B. Lyons,[‡] Michael C. Laufersweiler,[‡] Loon-Seng Tan,*[,§] and Jong-Beom Baek*[,†]

Ulsan National Institute of Science and Technology (UNIST), Ulsan 689-805, South Korea; Southwestern Ohio Council for Higher Education, Miami Valley Research Park, Dayton, Ohio 45420-4015; and Nanostructured & Biological Materials Branch, Materials & Manufacturing Directorate, Air Force Research Laboratory, AFRL/RXBN, Wright-Patterson Air Force Base, Dayton, Ohio 45433-7750

Received October 25, 2008; Revised Manuscript Received January 2, 2009

ABSTRACT: A new AB_2 monomer, 5-amino-4-hydroxyisophthalic acid hydrochloride, was synthesized and polymerized in poly(phosphoric acid) (PPA) to afford a carboxylic acid-terminated hyperbranched polybenzoxazole (HPBO). Taking advantage of the large number of peripheral carboxylic acid groups on HPBO, polyarm-star block copolymers, HPBO-*b*-*m*PEK and HPBO-*b*-*p*PEK, were conveniently prepared in the same reaction medium with additional amounts of phosphorus pentoxide (P_2O_5) via "direct" Friedel–Crafts acylation reaction with 3- and 4-phenoxybenzoic acids as AB monomers. All the resulting polymers displayed polyelectrolyte behaviors in solution due to the large number of carboxylic acid termini. The UV–vis absorption intensities, which increased as polymer concentration was increased, showed quasi-linear dependence in all sample solutions. The emission intensity drastically decreased as the concentration of HPBO core polymer was increased, while the block copolymers were not much affected by concentration variation. The emission behaviors of HPBO-*b*-*m*PEK and HPBO-*b*-*p*PEK should be inherent to the chromophoric inner HPBO cores, which were shielded by the outer linear PEK shells. The morphology study suggested that both proton conductivity and optical behaviors of HPBO might be greatly influenced by the globular core–shell architecture.

Introduction

Fused aromatic–heterocyclic polymers such as polybenzoxazoles (PBO), polybenzothiazoles (PBT), and polybenzimidazoles (PBI) continue to attract R & D interest mainly because of their high-temperature capabilities as well as their attractive mechanical, optical, and electronic properties,[1,2] more recently because of their potential for high-temperature fuel cell applications.[3] However, they have limited processability due to their insoluble nature and high softening temperature, which is generally above their degradation temperature. Structural modification on these materials has been necessary to improve their processability and specific property requirements. The traditional, linear structures of fused aromatic–heterocyclic polymers have been well studied for decades; arguably, the enhancement in their structural[4] and optoelectronic[5] properties has almost plateaued. Thus, the requirements of next-generation materials are driving the need to improve solubility for the better processability, and the consideration of three-dimensional structures as an alternative strategy to specific properties, which could not be fulfilled by traditional aromatic–heterocyclic rigid-rod polymers. For these combined requirements, materials with dendritic structures such as dendrimers and hyperbranched polymers have a great potential in the development of future materials.[6] Although there are numerous publications on dendrimers and hyperbranched polymers for the past 20 years or so,[6b] the reports on the syntheses and characterization of fused aromatic–heterocyclic dendritic polymers are fairly rare.[7] As an initial entry into this area, a novel hyperbranched polymer containing alternating quinoxaline and benzoxazole repeat units was prepared via an aromatic–heterocyclic-forming reaction in poly(phosphoric acid) (PPA).[8]

Herein we report the design and synthesis of a new AB_2 monomer containing reactive moieties to engage in benzoxazole-forming reaction in PPA to generate an all-aromatic hyperbranched polybenzoxazole (HPBO), which was used as the core block for star-branched block copolymers synthesized in the same medium with additional optimized amount of phosphorus pentoxide (P_2O_5). The characterization of resultant star-block polymers was also investigated, and the results are reported here as well.

Experimental Section

Materials. All chemicals and solvents including poly(phosphoric acid) (PPA, assay ≥83% P_2O_5 content) and phosphorus pentoxide (P_2O_5) were purchased from Aldrich Chemical Inc. and used as received, unless otherwise specified. The AB monomers, 3- and 4-phenoxybenzoic acids for linear poly(ether ketone)s (PEK), were purchased from Aldrich Chemical Co. They were purified by recrystallization from toluene/heptane (5/5, v/v) mixture to give shiny colorless needles (mp 147–148.5 and 162–164 °C, respectively).[9]

Instrumentation. Elemental analysis and mass spectral analysis were performed by System Support Branch, Materials & Manufacturing Directorate, Air Force Research Laboratory, Dayton, OH. The melting points (mp) of all compounds were determined on a Mel-Temp melting point apparatus and are uncorrected. Intrinsic viscosities were determined using Cannon-Ubbelohde No. 200 viscometer. Flow times were recorded for methanesulfonic acid (MSA) solution, and polymer concentrations were in the range of 0.5–0.1 g/dL at 30.0 ± 0.1 °C. Differential scanning calorimetry (DSC) was performed under a nitrogen atmosphere with heating and cooling rates of 10 °C/min using a Perkin-Elmer DSC7 equipped with TAC7 controller. The DSC thermograms were obtained on powder samples after they had been heated to 400 °C and cooled to 20 °C. Glass transition temperatures (T_g's) were taken

* Corresponding authors: Tel +1-937-255-9153, Fax +1-937-656-6327, e-mail Loon-Seng.Tan@wpafb.af.mil (L.-S.T.); Tel +82-52-708-7034, Fax +82-52-708-7010, e-mail jbbaek@unist.ac.kr (J.-B.B.).
[†] Ulsan National Institute of Science and Technology.
[‡] Southwestern Ohio Council for Higher Education.
[§] Air Force Research Laboratory.

10.1021/ma802401v CCC: $40.75
Published on Web 02/09/2009

as the midpoint of the baseline shift. Thermogravimetric analysis (TGA) was conducted both in air and nitrogen atmospheres with a heating rate of 10 °C/min using a Perkin-Elmer TGA7. Proton conductivity was evaluated using a two-point probe method with a Solartron 1260 ac impedance analyzer with an amplitude of 10 mV and a frequency range of 1−100 000 Hz at relative humidity of 50%. Each sample was fixed in a Teflon conductivity test cell consisting of a working and a reference Pt electrodes. The sample conductivity was determined by using $\sigma = (1/R)(L/A)$, where R is the resistance, L is the sample thickness, and A is the cross-sectional area. UV−vis spectra were obtained from a Perkin-Elmer Lambda 35 UV/vis spectrometer. Fluorescence studies were conducted with a Perkin-Elmer LS 55 fluorescence spectrometer. The applied excitation wavelength was the UV absorption maximum of each sample. The field emission scanning electron microscopy (FE-SEM) used in this work was LEO 1530FE. The energy-minimized structures were performed by the CS Chem3D Ultra computational package (version 8.0.3, CambridgeSoft Corp., Cambridge, MA 02140).

Dimethyl 4-Hydroxyisophthalate (1). Into a 250 mL three-necked round-bottom flask equipped with a magnetic stirrer, a condenser, and dropping funnel, a solution of 4-hydroxyisophthalic acid (15.0 g, 82.4 mmol) in 150 mL of dried methanol was charged. Freshly distilled thionyl chloride (75.0 g, 630.5 mmol) was then added dropwise for 30 min. The mixture was gently heated under reflux for 4 h. Upon cooling to room temperature, white flakes formed and were collected by suction filtration to give 16.3 g (94% yield); mp 93−94 °C. Anal. Calcd for $C_{10}H_{10}O_5$: C, 57.14%; H, 4.80%; O, 38.06%. Found: C, 56.89%; H, 4.72%; O, 38.15%. FT-IR (KBr, cm^{-1}): 3416, 3211, 2964, 1733, 1689. Mass spectrum (*m/e*): 210 (M^+, 100% relative abundance) 179, 151. ^1H NMR ($CDCl_3$; δ ppm): 3.90 (s, 3H, CH_3), 3.98 (s, 3H, CH_3), 6.98−7.01 (d, 1H, Ar), 8.08−8.12 (dd, 1H, Ar), 8.53−8.54 (d, 1H, Ar), 11.19 (s, 1H, OH). ^{13}C NMR ($CDCl_3$; δ ppm): 52.09, 52.61, 112.14, 117.78, 121.44, 132.47, 136.58, 165.09, 165.99, 170.10.

Dimethyl 4-Hydroxy-5-nitroisophthalate (2). Into a 250 mL three-necked round-bottom flask equipped with a magnetic stirrer, a condenser, and nitrogen inlet, dimethyl 4-hydroxyisophthalate (15.0 g, 71.4 mmol) was dissolved in acetic acid (150 mL). Nitric acid (10 mL) was then added dropwise. The mixture was warmed at 60 °C for 12 h. After cooling down, the mixture was poured into water. The light yellow precipitate was collected, air-dried, and recrystallized from ethanol to give 16.0 g (88% yield) of light yellow crystals; mp = 74.76 °C. Anal. Calcd for $C_{10}H_9NO_7$: C, 47.07%; H, 3.55%; N, 5.49%; O, 43.89%. Found: C, 47.75%; H, 4.01%; N, 5.44%; O, 43.51%; FT-IR (KBr, cm^{-1}): 3076, 2992, 1722, 1690. Mass spectrum (*m/e*): 255 (M^+, 100% relative abundance), 241, 237. ^1H NMR (DMSO-d_6; δ ppm): 3.89 (s, 3H, CH_3), 3.97 (s, 3H, CH_3), 8.46−8.47 (d, 1H, Ar), 8.55−8.56 (d, 1H, Ar). ^{13}C NMR ($CDCl_3$, δ ppm): 52.72, 53.38, 117.60, 120.19, 130.61, 135.31, 138.50, 156.13, 163.70, 166.87.

Dimethyl 5-Amino-4-hydroxyisophthalate (3). Into a 500 mL high-pressure bottle, dimethyl 4-hydroxy-5-nitroisophthalate (15.0 g, 58.8 mmol), palladium on activated carbon (10%, 1.0 g), and acetic acid (200 mL) were charged. The bottle was placed on the hydrogenation vessel. Hydrogen was charged and discharged five times and agitated at 60−65 psi for 24 h. After filtered through Celite 545 to remove catalyst, the solvent was removed on a rotavap. The orange residue was recrystallized from deoxygenated ethanol to give 12.1 g (91% yield) of brown needles; mp 161−163 °C, 205 °C (free amine, dec), 335 °C (hydrochloric acid salt, dec). Anal. Calcd for $C_{10}H_{11}NO_5$: C, 53.33%; H, 4.92%; N, 6.22%, O, 35.52%. Found: C, 53.40%; H, 4.88%; N, 5.92%, O, 35.57. FT-IR (KBr, cm^{-1}): 3484, 3384, 2966, 1707, 1668. Mass spectrum (*m/e*): 225 (M^+, 100% relative abundance), 193, 165, 162. ^1H NMR (DMSO-d_6; δ ppm): 3.91 (s, 3H, CH_3), 3.99 (s, 3H, CH_3), 8.20−8.22 (d, 1H, Ar), 8.29−8.30 (d, 1H, Ar), 9.90 (NH, and OH). ^{12}C NMR (DMSO-d_6; δ ppm): 52.63, 53.33, 114.02, 121.07, 123.06, 128.23, 129.45, 157.51, 165.63, 170.72.

5-Amino-4-hydroxyisophthalic Acid Hydrochloride (4). Into a 250 mL three-necked, round-bottom flask equipped with a magnetic stirrer, nitrogen inlet, and a condenser, dimethyl 5-amino-4-hydroxyisophthalate (11.0 g, 48.8 mmol) and concentrated hydrochloric acid (200 mL) were placed. The mixture was then heated under reflux with vigorous stirring until the solution became homogeneous. It took about 6 h. While the mixture was cooling down, white flakes formed and were collected by suction filtration and dried under the reduced pressure to give 7.1 g (74% yield) of off-white crystals; mp >300 °C (dec). Anal. Calcd for $C_8H_8ClNO_5$: C, 41.13%; H, 3.45%; Cl, 15.18%; N, 6.00%; O, 34.24%. Found: C, 40.81%; H, 3.40%; Cl, 15.26%; N, 5.56%; O, 33.50%. FT-IR (KBr, cm^{-1}): 1684 (carboxylic C═O), 2580, 2892 (COOH), 3406 (NH), 3396 (OH). Mass spectrum (*m/e*): 197 (M^+, 100% relative abundance). ^1H NMR (DMSO-d_6, δ ppm): 8.21−8.22 (d, 1H, Ar), 8.30−8.31 (d, 1H, Ar), 9.91 (broad s, COOH, NH, and OH). ^{13}C NMR (DMSO-d_6; δ ppm): 114.01, 121.01, 123.05, 128.26, 129.47, 157.52, 165.64, 170.74.

Hyperbranched Polybenzoxazole (HPBO, 5). Into a 250 mL resin flask equipped with a high-torque mechanical stirrer, nitrogen inlet, and outlet, PPA (60 g) was placed and stirred with dried nitrogen purging for 10 h. The monomer, 5-amino-4-hydroxyisophthalic acid hydrochloride (1.5 g, 6.4 mmol), was added, and the resulting mixture was dehydrochlorinated under reduced pressure (1 mmHg) at 60 °C for 24 h, 100 °C for 24 h, and 130 °C. Upon completion of the dehydrochlorination step, the mixture was gently heated to 160 °C for 4 h. When the temperature was approach 160 °C, the mixture became viscous. The mixture was further heated to ensure complete ring closure to 180 °C for 24 h. At the end of the reaction, water was added into the flask and poured into a Warring blender and the bundles chopped, collected by suction filtration, washed with diluted ammonium hydroxide and then Sohxlet-extracted with water for 3 days and methanol for 3 days, and finally dried under reduced pressure (1 mmHg) at 150 °C for 48 h to give 1.01 g (97.6% yield) of brown solids. An intrinsic viscosity of 0.42 dL/g (30 ± 0.1 °C in MSA) and 0.20 dL/g (30 ± 0.1 °C in NMP) were determined. Anal. Calcd for $C_8H_3NO_3$: C, 59.64%; H, 1.88%; N, 8.69%; O, 29.79%. Found: C, 53.86%; H, 2.73%; N, 7.65%; O, 33.74%.

Hyperbranched PBO-*block*-*m*PEK Star Block Copolymerization (6). Into a 100 mL resin flask equipped with a high-torque mechanical stirrer, nitrogen inlet and outlet, PBO 5 (0.10 g, 0.62 mmol) and PPA (20 g) were placed. The mixture was heated to 130 °C and stirred for 8 h until the mixture became homogeneous. The AB monomer, 3-phenoxybenzoic acid (1.0 g, 4.67 mmol), and P_2O_5 (5.0 g) were added. The temperature was maintained at 130 °C for 48 h. At the end of the reaction, water was added to the flask and poured into a Warring blender. After the polymer bundles had been chopped, collected by suction filtration, and washed with diluted ammonium hydroxide, it was Sohxlet extracted with water for 3 days and then methanol for 3 more days, and finally dried under reduced pressure (1 mmHg) at 150 °C for 48 h to give 1.00 g (98.4% yield) of deep purple solids. An intrinsic viscosity of 1.65 dL/g (MSA, 30 ± 0.1 °C) was determined. Anal. Calcd for $C_{12.41}H_{7.41}N_{0.12}O_{2.12}$: C, 77.23%; H, 3.85%; N, 1.02%; O, 17.89%. Found: C, 76.14%; H, 4.20%; N, 0.79%; O, 17.67%.

Hyperbranched PBO-*block*-*p*PEK Star Block Copolymerization (7). Into a 100 mL resin flask equipped with a high-torque mechanical stirrer, nitrogen inlet, and outlet, PBO 5 (0.10 g, 0.62 mmol) and PPA (20 g) were placed. The reaction conditions and work-up procedures were the same as those for 6 to give 0.98 g (96.5% yield) of light pink solids. An intrinsic viscosity of 0.55 dL/g (MSA, 30 ± 0.1 °C) was determined. Anal. Calcd for $C_{12.41}H_{7.41}N_{0.12}O_{2.12}$: C, 77.23%; H, 3.85%; N, 1.02%; O, 17.89%. Found: C, 77.04%; H, 4.01%; N, 0.88%; O, 17.72%.

Extraction of Free *m*PEK from HPBO-*b*-*m*PEK. *m*PEK is amorphous polymer, and it is readily soluble in methylene chloride (CH_2Cl_2), but HPBO-*b*-*m*PEK is not. Therefore, the purple powder sample of HPBO-*g*-*m*PEK (1.00 g) was dispersed in CH_2Cl_2 in a closed vial at room temperature for 24 h. The suspension was collected by filtration. It was repeatedly dispersed in fresh CH_2Cl_2 and collected by filtration until no sign of dark spot from filtrate (free *m*PEK in CH_2Cl_2) on a thin-layer chromatography (TLC) plate.

Scheme 1. Monomer Synthesis[a]

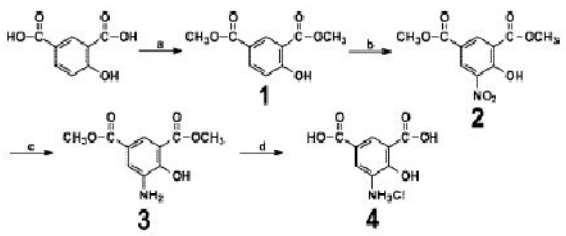

[a] a: $SOCl_2$/MeOH, reflux; b: HNO_3/AcOH, 60 °C; c: H_2 (65 psi), EtOH, rt; d: conc HCl, reflux.

The collected suspension was dried under reduced pressure (0.01 mmHg) to give 0.98 g of purple powder. The result indicated that the most of *m*PEK had been covalently attached onto HPBO.

Results and Discussion

AB_2 Monomer Synthesis. The AB_2 monomer for the hyperbranched benzoxazole parent polymer (HPBO), 5-amino-4-hydroxyisophthalic acid hydrochloride (**4**), was synthesized via a four-step sequence (Scheme 1). Thus, 4-hydroxyisophthalic acid was first converted to the corresponding bis(methyl ester), **1**, followed by nitration in glacial acetic acid to form the precursor, dimethyl 4-hydroxy-5-nitroisophthalate (**2**). Finally, the requisite AB_2 monomer was obtained in good yield after Pd/C-catalyzed hydrogen reduction of **2**, followed by treatment with concentrated HCl. All intermediates and the monomer were verified by conventional techniques such as melting point, proton and carbon nuclear magnetic resonance spectroscopy (^{1}H and ^{13}C NMR; see Supporting Information Figures S1a and S1b, respectively), Fourier-transform infrared spectroscopy (FT-IR), high-performance liquid chromatography (HPLC), and elemental and mass spectral analyses.

Polymerization of AB_2 Monomers. The polycondensation of the AB_2 monomer **4** to afford the parent polymer HPBO **5** was carried out at monomer concentration of 2.5 wt % and final reaction temperature at 180 °C in PPA (83% assay). We observed that soon after the reaction temperature had reached 160 °C, the mixture became very viscous, which was an indication of substantial molecular weight build-up. The mixture was further heated to 180 °C to ensure complete ring closure before work-up (Scheme 2). The final product was subjected to Soxhlet extraction with water for 3 days to completely remove residual PPA and methanol for an additional 3 days to remove any remaining low molecular mass impurities. The yield of product after complete work-up was almost quantitative, which was an indication of high conversion.

Star-Branched Block Copolymers. Because of the availability of large number of the carboxylic acid end groups of HPBO **5**, star-branched block copolymers could be prepared and utilized to tailor their physical properties for various applications. The average number of available reactive carboxylic acids on HPBO is equal to the degree of polymerization plus one (DP + 1), when the *o*-aminophenol focal point group is assumed to be intact. However, when the reactivity of functional group is high and the concentration of monomer is low (it was 2.5 wt % with reference to the amount of PPA used), the focal point would most likely react with one of peripheral carboxylic acids to form an intramolecular loop.[10] Hence, it is very likely that the number of available functional carboxylic acids on HPBO was equal to DP. By taking advantage of these reactive groups, polyarm-star block copolymers could be prepared by Friedel−Crafts acylation reaction using either 3- or 4-phenoxybenzoic acids as an AB monomer in the same pot with additional amount of phosphorus pentoxide (P_2O_5). The optimized reaction medium PPA/P_2O_5 can promote "direct" Friedel−Crafts acylation reaction, in which a carbocation ion ($-C^+=O \leftrightarrow -C\equiv O^+$, also known as acylium) could be generated directly from carboxylic acid instead of acid chloride as a polymer-forming reaction (Scheme 3).[11] Although one-pot syntheses of star block copolymers are possible by simply adding the corresponding monomers and additional P_2O_5 into the HPBO/PPA mixture right after homopolymerization, the parent polymer HPBO was isolated and completely worked up in this study in order to keep the molecular weight constant so that the resultant samples could be reasonably compared with each other. In this way, the isolated HPBO was redissolved in PPA, and then the corresponding AB monomer and the required amount of P_2O_5 was added. The resultant star block copolymers are denoted as HPBO-*b*-*m*PEK and HPBO-*b*-*p*PEK for HPBO-*block*-*meta*-poly(ether ketone) and HPBO-*block*-*p*-poly(ether ketone), respectively. The presence of free PEKs in the star block copolymers was indirectly determined by a simple extraction-and-weighing experiment on HPBO-*b*-*m*PEK (see Experimental Section for details). Considering possible loss during work-up routines, we estimated less than 2 wt % of free *m*PEK in the HPBO-*b*-*m*PEK. Thus, it could be assumed that most of PEKs were covalently linked to the HPBO.

Solution Properties. It has been established that hyperbranched polymers have generally higher solubility in a given solvent than their linear analogues with similar molecular weights.[12] Expectedly, the parent polymer HPBO 5 was found to be soluble in most of polar aprotic solvents (PAS) such as *N*,*N*-dimethylacetamide (DMAc), *N*,*N*-dimethylformamide (DMF), and *N*-methyl-2-pyrrolidinone (NMP), while its linear analogue, which is only soluble in strong acids such as sulfuric acid and methanesulfonic acid (MSA), is insoluble in these amide solvents.[13] However, we found that the extent of solubility of HPBO in PAS depended on the dryness of the sample. It was soluble in these solvents when the sample was not completely dry. Once the sample had been subjected to rigorous drying, it became much less soluble in PAS, but it could still dissolve quite well in strong acids such as trifluoroacetic acid (TFAA), sulfuric acid (MSA), and trifluoromethanesulfonic acid (TFMSA). While an in-depth investigation of this phenomenon was beyond the scope of this project, we could, however, theorize that the relationship between sample's solubility and dryness in common polar aprotic solvents is presumably due to the formation of strong intra- and intermolecular hydrogen bonding, which are driven by the large number of peripheral carboxylic acids. The proposed hydrogen-bonded structures are depicted in Scheme 4, and we offer a tentative explanation as follows. When the sample contains certain amount of water, the formation of intra- or intermolecular hydrogen bonding within a HPBO macromolecule or among a group of HPBO macromolecules, respectively, is hampered by water molecules (Scheme 4a), each of which can accept two hydrogen bonds and donate two hydrogen bonds as opposed to a COOH group, which can only accept a hydrogen bond and donate a hydrogen bond. For example, when its residual water content was more than 5 wt % by TGA, a HPBO sample was soluble in PAS, and there were no insoluble gels observed in the solutions. On the other hand, when the sample was completely dry (i.e., without water molecules act as some sort of plasticizer), intra- and intermolecular hydrogen bonding could be formed strongly among the HPBO macromolecules, which could be more tightly packed in a 3-dimensional fashion (Scheme 4b). As a result, completely dried HPBO showed limited solubility in PAS. To provide a proof for the above scenario, a HPBO sample was freeze-dried while it was still wet after Soxhlet extraction with water. The freeze-dried

Scheme 2. Synthesis of Hyperbranched Poly(Benzoxazole) (HPBO) 5 (Idealized Structure with *o*-Aminophenol as Focal Group and COOH as Terminal Groups)

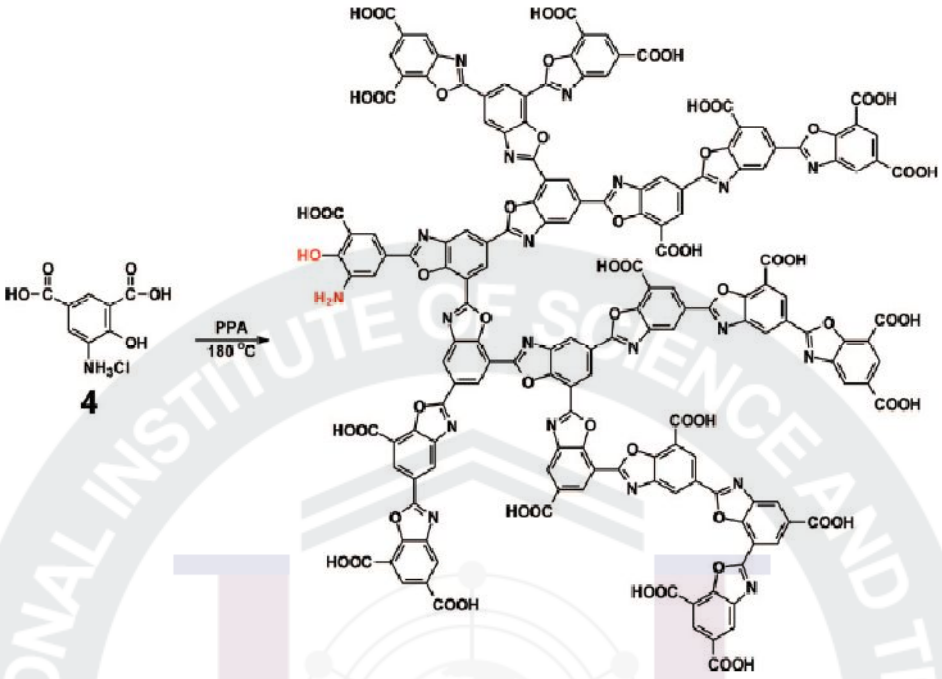

Scheme 3. Synthesis of Polyarm-Star Block Copolymers 6 and 7

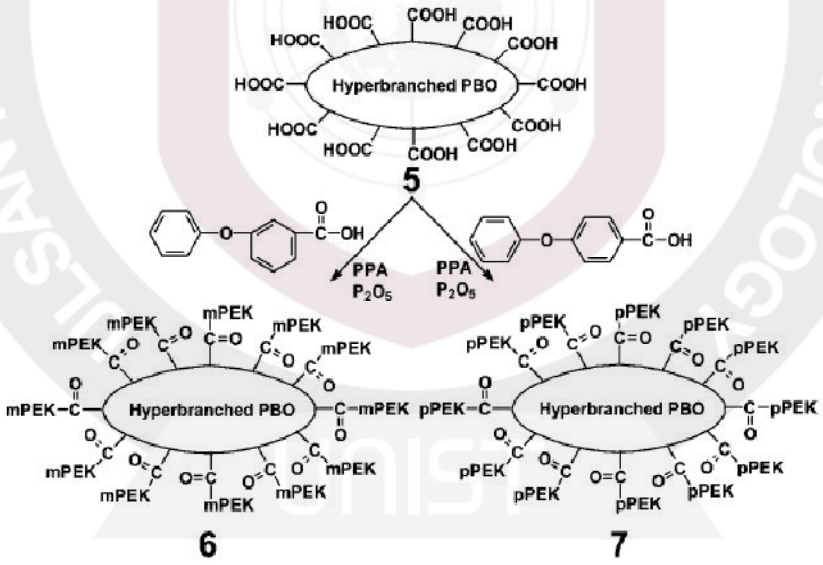

HPBO sample appeared to be much softer and fluffier, whereas another HPBO sample that had been dried in a vacuum oven under reduced pressure was rock hard. Furthermore, the freeze-dried sample was freely soluble in polar aprotic solvents. Thus, this empirical comparison together with the similar solubility behaviors that were observed and reported for the hydroxyl-terminated hyperbranched poly(phenylquinoxaline)[7a] and carboxylic acid-terminated hyperbranched poly(ether−ketone)s[10] could serve to buttress our explanation.

During the viscosity measurements, we observed that the HPBO parent polymer, which has numerous carboxylic acids on its periphery, displayed a strong polyelectrolyte behavior as a function of its concentration in both acidic (MSA) and basic (NMP) media (Figure 1). In the case of the HPBO in acidic solvent (MSA), both reduced and inherent viscosities were drastically increased. Since the carboxylic acids ($pK_a \sim 4.2$) on HPBO can act as proton acceptors in the presence of much stronger acid (in this case, MSA with a $pK_a \sim -2$), the resulting protonated HPBO became a polyelectrolyte (Scheme 5a). In the case of the HPBO sample in basic NMP solvent, the existence of polyelectrolyte effect is rather surprising because both NMP and carboxylic acid are not strong enough as a base and an acid to engage in a complete proton transfer process (i.e., salt formation). However, it is known that NMP can complex

Scheme 4. Schematic Representation of Proposed 3-D Hydrogen-Bonded Structures in HPBO: (a) Hydrated Sample; (b) Completely Dried Sample[a]

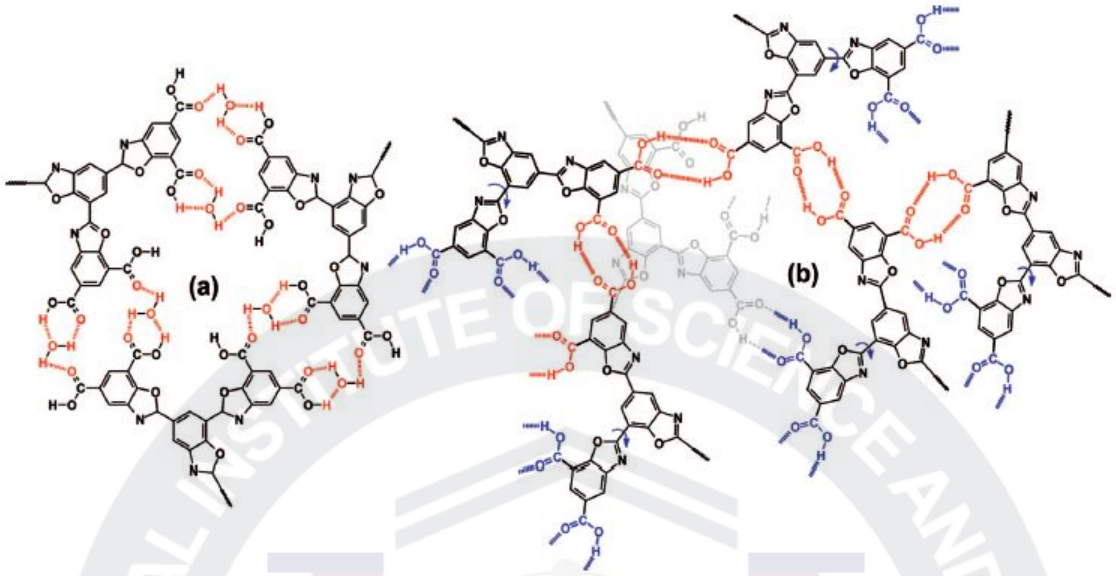

[a] The structural units shown in red are on the same plane while those shown in blue are out of the plane as a result of rotation around the C−C bond indicated by blue arrows.

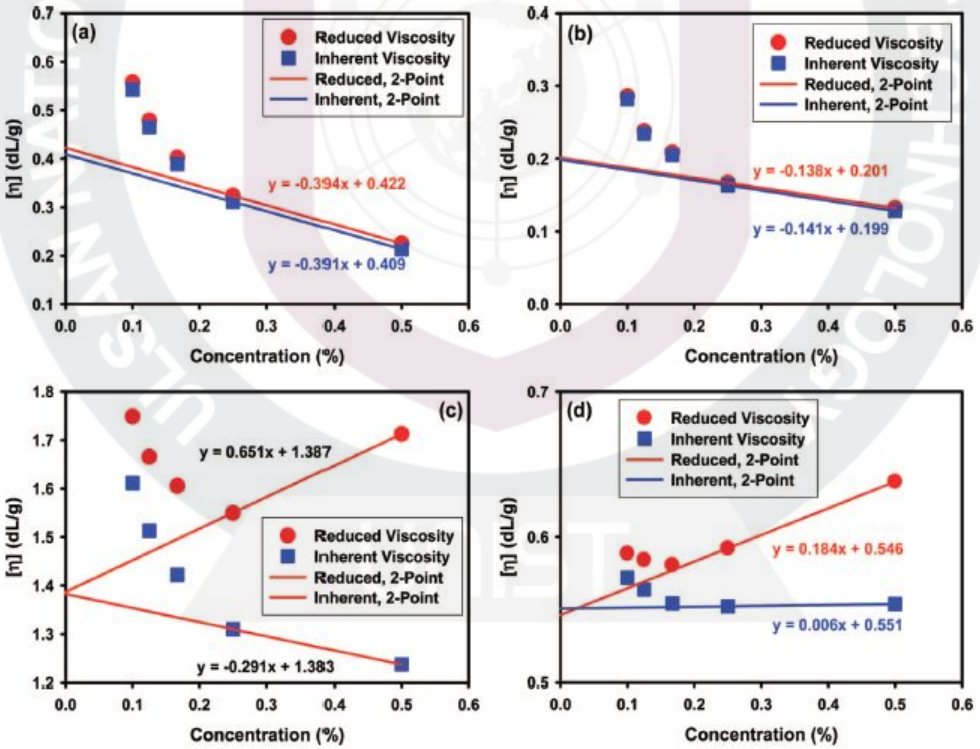

Figure 1. Solution behaviors of HPBO and its polyarm-star block copolymers: (a) HPBO in MSA; (b) HPBO in NMP; (c) HPBO-*g*-*m*PEK in MSA; (d) HPBO-*g*-*p*PEK in MSA.

strongly with an aromatic carboxylic acid via the combination of acid/base interaction and hydrogen bonding.[14] Such complexation (see Scheme 5b) is equilibrium-driven; i.e., the higher the NMP's number density (in other words, the more dilute HPBO concentration in NMP), the more complexes would form within each HPBO macromolecule, leading to more extended structure. Thus, we speculate that upon dilution HPBO macromolecules stretch out to greatly expand their hydrodynamic volumes, which results in the observed sharp increase in viscosity.

Scheme 5. Schematic Representation of Polyelectrolyte Structures: (a) Salt Formation in MSA Solution; (b) Proposed Complexation, Leading to Hydrodynamic Volume Expansion and Observed Polyelectrolyte Effect, in Dilute NMP Solution[a]

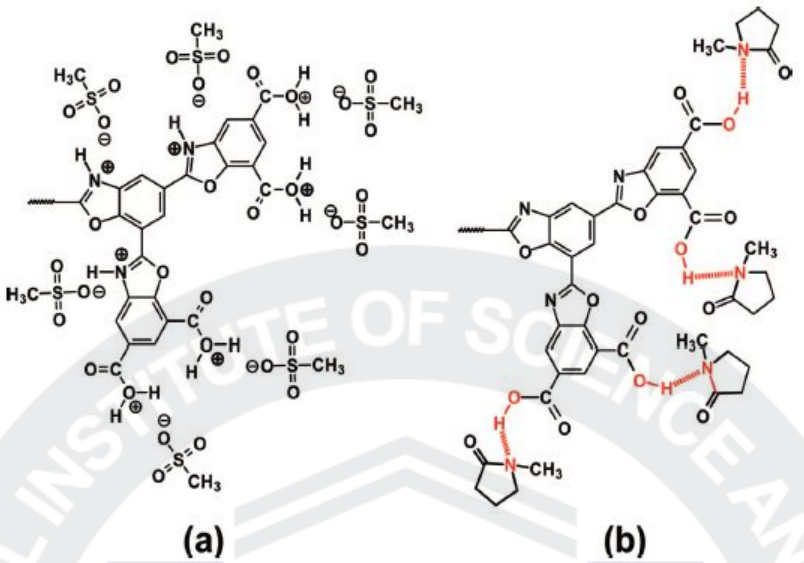

[a] Hydrogen bonds are highlighted in red.

Because of the polyelectrolyte effect, it was difficult to determine intrinsic viscosity ([η]) via the usual multipoint (five-point) measurement. Therefore, the approximate [η] values were obtained by extrapolating the initial two-point to zero concentration. HPBO had an intrinsic viscosity of 0.42 dL/g at 30 ± 0.1 °C in MSA solution and 0.20 dL/g at 30 ± 0.1 °C in NMP solution. The value obtained from the MSA solution is about 2 times higher than that obtained from the NMP solution. Furthermore, the slopes for the reduced and inherent viscosities are negative in both solutions. The latter result implies that the hydrodynamic volume of HPBO is getting larger as its concentration is lowered. With the caveat that the extrapolation to zero concentration might have overestimated the intrinsic viscosity values, this seems to suggest that in MSA solution the HPBO macromolecule is more "opened up" and chain-extended than when it is in NMP solution.

The star block copolymers, HPBO-*b*-*m*PEK and HPBO-*b*-*p*PEK, displayed much higher solution viscosities than the HPBO core due to the attachment of linear arms (Figure 1c,d). The copolymers had different reduced viscosity behavior compared to HPBO (Figure 1a). This implies that the molecular architecture of block copolymers has been changed. However, they still displayed polyelectrolyte effect because both block copolymers contained a large number of carboxylic acid chain ends. Another noteworthy point is that the viscosities of HPBO-*b*-*p*PEK (with stiffer *p*PEK chains) are lower than that of HPBO-*b*-*m*PEK (with more flexible *m*PEK chains). A plausible explanation for this otherwise surprising result is that the average molecular weight of *p*PEK chains could be significantly lower than that of *m*PEK as evidenced by our previous finding that the homopolymerization of 4-phenoxybenzoic acid and 3-phenoxybenzoic acid under the same conditions had led to *p*PEK with [η] = 0.69 dL/g and *m*PEK with [η] = 2.10 dL/g, respectively.[15] This is most likely because semicrystalline *p*PEK would start to fall out of the solution upon reaching certain molecular weight during polymerization.

Thermal Properties. HPBO is hygroscopic, stemming from the large number of carboxylic acids on its periphery and easily absorbs moisture even after having been dried under reduced pressure. Thus, it is not surprised that the outgassing of absorbed moisture featured prominently in the DSC thermogram of HPBO as a broad endotherm centered at 122 °C during the first heating scan (Figure 2a). Following immediately is another broad exotherm peaked around 223 °C, which would be attributed to the thermal relaxation of HPBO. It has been shown that the growing polymer molecules can store strain energy induced by viscosity and shear during polymerization in a viscous reaction medium such as PPA. Such stored strain energy would be released under appropriate thermal conditions.[15] The third endotherm was observed above 337 °C, assignable to the loss of carboxylic acids in the form of carbon dioxide. The glass transition temperature (T_g) was not detected in the range from room temperature to 400 °C in the second heating scan (Figure 2b). HPBO-*b*-*m*PEK displayed a T_g at 142 °C in the first heating scan, which was slightly increased to 144 °C during the second heating scan. Because *m*-poly(ether−ketone), *m*PEK, is an amorphous polymer, the HPBO-*b*-*m*PEK star block copolymer was also expected to be amorphous. The detected T_g value is ~7 °C higher than that of *m*PEK homopolymer (T_g = 137 °C) prepared under the same conditions.[11,15] This T_g increase could be because the rigid inner HPBO core was "holding" one end of each *m*PEK chain, restricting its mobility. In the case of HPBO-*b*-*p*PEK, it displayed melting endotherm peaked at 332 °C (heat of fusion, ΔH_f = 38 J/g) in the first heating scan (Figure 2a). This value is ~12 °C lower than that of *p*PEK homopolymer (T_m = 344 °C, ΔH_f = 33 J/g).[11,15] The melting point depression of HPBO-*b*-*p*PEK could be originated from the poorer chain mobility of *p*PEK from being tied to the rigid HPBO core. Hence, the *p*PEK chains in the star block copolymer should form less stable crystals (i.e., the degree of crystallinity is much reduced as compared to that of *p*PEK homopolymer). In the second heating scan (Figure 2b), HPBO-*b*-*p*PEK displayed T_g at 164 °C, which was comparable to that of *p*PEK homopolymer (T_g = 159 °C, first heating scan; T_g = 165 °C, second heating scan).[11,15] However, the T_m associated with a smaller endotherm detected during the second heating scan was 14 °C lower, at 318 °C, which might imply that the chain mobility of *p*PEK in HPBO-*b*-*p*PEK was also poorer, in addition to lower degree of crystallinity.

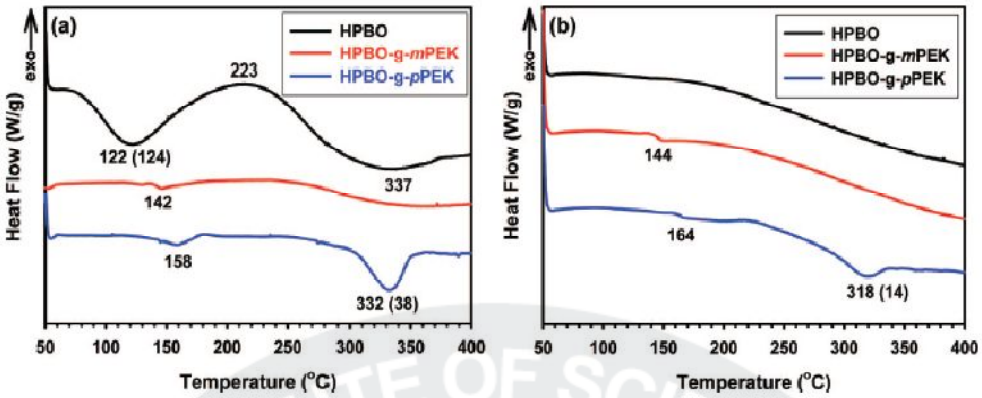

Figure 2. DSC thermograms of HPBO and its polyarm-star block copolymers: (a) first heating scan; (b) second heating scan.

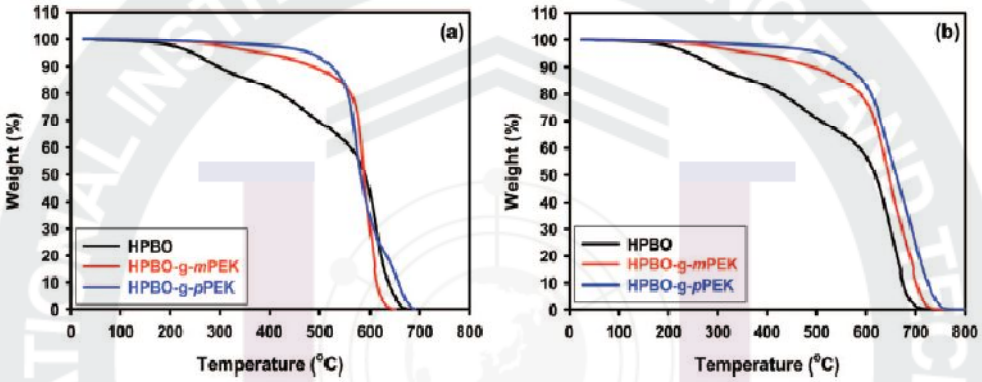

Figure 3. TGA thermograms of HPBO and its polyarm-star block copolymers: (a) in air; (b) in nitrogen.

Scheme 6. Idealized Structural Representation of Repeat Unit Segment in Two Liming Cases: (a) Fully Protonation of HPBO in MSA Solution; (b) Completely Neutral HPBO Structure in NMP Solution (See Scheme 5 Also)[a]

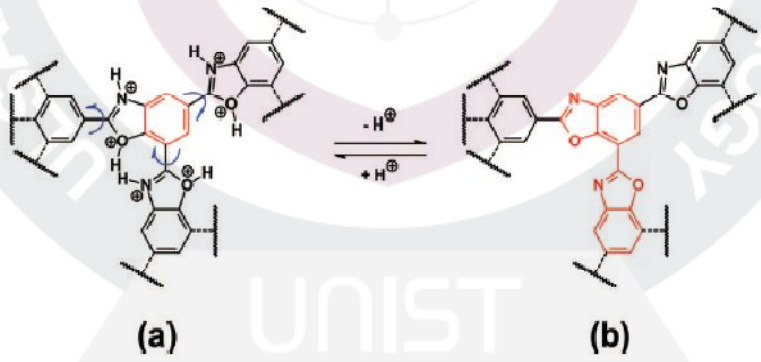

[a] In (a), the degrees of conjugation and aromaticity (shown in red) are reduced because of protonation and rotation around the C−C bonds (indicated by the blue arrows).

Thermo-oxidative and thermal stabilities of HPBO, HPBO-*b*-*m*PEK, and HPBO-*b*-*p*PEK were determined by thermogravimetric analysis (TGA). Since all the terminal groups (total number ~DP) of HPBO were hygroscopic carboxylic acids, HPBO displayed a stepwise weight-loss profile (Figure 3a). The early weight loss started around 200 °C when absorbed moisture outgassed. The discrepancy between the theoretical and experimental carbon numbers in the elemental analysis result (see Experimental Section) could be explained by this moisture uptake. The next weight loss around 380 °C was associated with the decomposition of carboxylic acid into carbon dioxide, which was also observed in a DSC study (see Figure 2a). The observed temperature for thermal CO_2 release agreed well with a previous study on the solid-state decomposition of benzoic acid derivatives.[16] The amount of carbon dioxide loss is ~27.0 wt %, which is in excellent agreement with the calculated value of 27.3 wt %.

The HPBO-*b*-*m*PEK and HPBO-*b*-*p*PEK samples were expected to be less hygroscopic because the number density of carboxylic acid groups in the star-block copolymer system is made smaller by the additional PEK repeat units. Hence, the TGA thermograms of both HPBO-*b*-*m*PEK and HPBO-*b*-*p*PEK do not show the early weight loss around 200 °C (Figure 3a). The 5 wt % weight loss temperatures ($T_{d5\%}$'s) of HPBO-*b*-*m*PEK

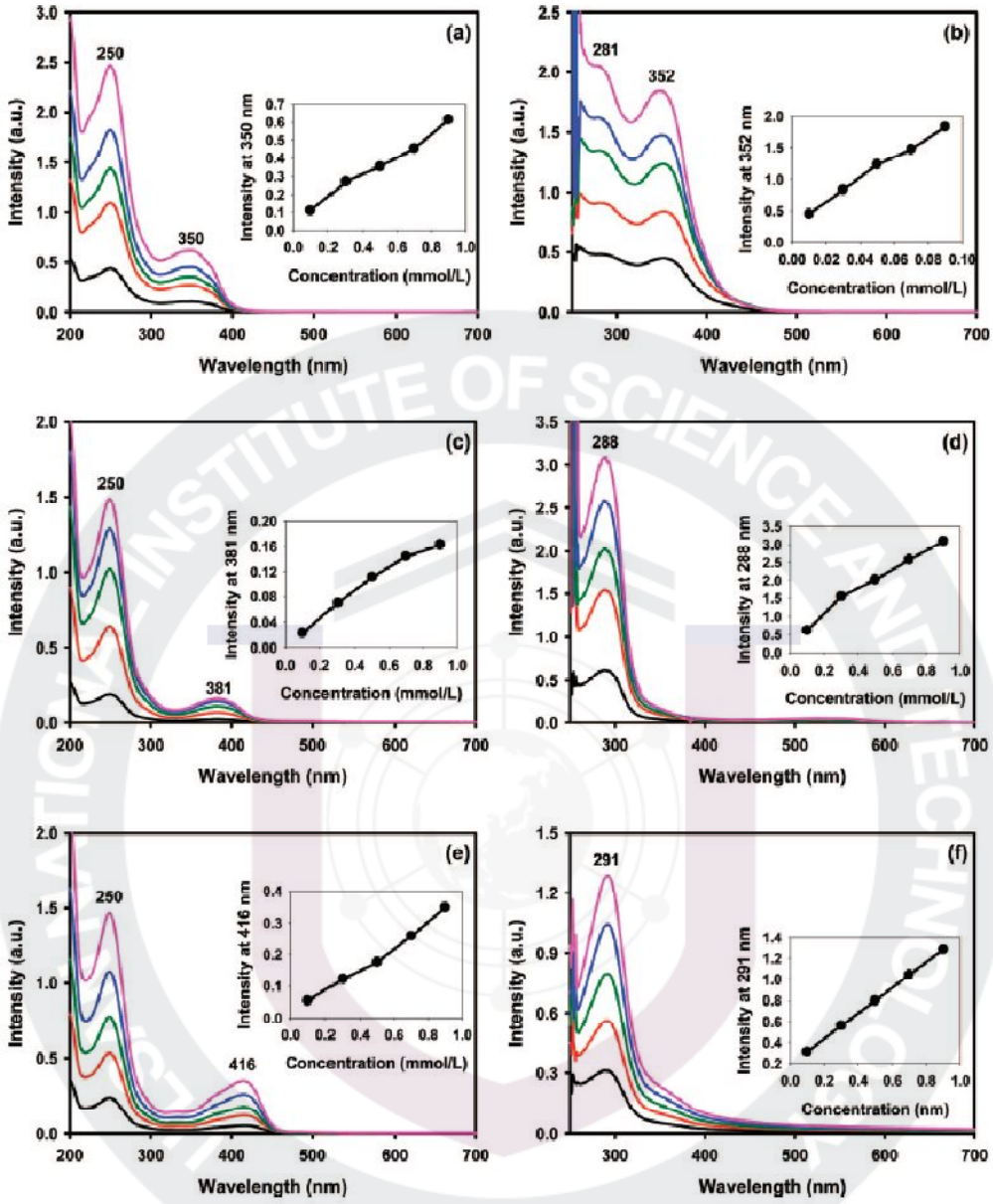

Figure 4. UV-absorption spectra of sample solutions: (a) HPBO in MSA; (b) HPBO in NMP; (c) HPBO-*g*-*m*PEK in MSA; (d) HPBO-*g*-*m*PEK in NMP; (e) HPBO-*g*-*p*PEK in MSA; (f) HPBO-*g*-*p*PEK in NMP.

and HPBO-*b*-*p*PEK were 380 and 480 °C in air, respectively. The $T_{d5\%}$'s of the samples in nitrogen were 368 and 510 °C, respectively (Figure 3b).

Optical Properties of HPBO. Since the linear analogues of HPBO, in particular rodlike poly(benzobisoxazole)s, are highly conjugated and therefore optically and electronically active,[17] it would be of special interest to assess how the hyperbranched architecture and the surface carboxylic groups influence HPBO's optical properties. Thus, the UV−vis absorption and fluorescence measurements of HPBO were conducted in both acidic MSA and basic NMP solutions. HPBO in acidic MSA solution displayed two strong absorption peaks in the UV region at 250 nm and the visible region at 350 nm (Figure 4a). HPBO in basic NMP solution showed those peaks at 281 and 352 nm, respectively (Figure 4b). In considering the environment effect, the wavelength values for the peaks in near-visible region were comparable, but for those in near-UV region there is a 31 nm span in the wavelength values between acidic and basic solutions. In addition, the intensity for the 250 nm peak is higher than that for the 350 nm peak in MSA, but the reverse is observed for the 281 and 352 nm peak in NMP. Furthermore, the intensity for the 350 or 352 nm peak was almost linearly dependent on HPBO concentrations in both solutions (see insets for Figure 4a,b), indicating that there was basically no concentration effect in the ground-state absorption of HPBO. We rationalize these results in terms of how the extents of coplanarity and conjugation length are adversely affected when the environment becomes highly acidic that all the lone-pair electrons are protonated, effectively hampering the delocalization process among the benzoxazole units, as shown in Scheme 6.

In the case of HPBO-*b*-*m*PEK in MSA solution (Figure 4c), the absorption maximum in the near-UV region remained

Scheme 7. Proposed Structure (b) for the "Interphase" Segment for Either HPBO-*b*-*m*PEK or HPBO-*b*-*p*PEK Where in MSA Protonation at the Imidazole Nitrogen or the Carbonyl and Imidazole Oxygens Leads to Two Types of Hydrogen-Bonded Six-Membered Ring Structures; Ring Structures Increase the Extent of Molecular Planarity (Highlighted in Red) in Comparison with the Neutral State, Idealized in Structure (a), Where Free Rotation around the C−C Bonds Indicated by Blue Arrows Would Disrupt Coplanarity of the Adjacent Benzoxazole Units

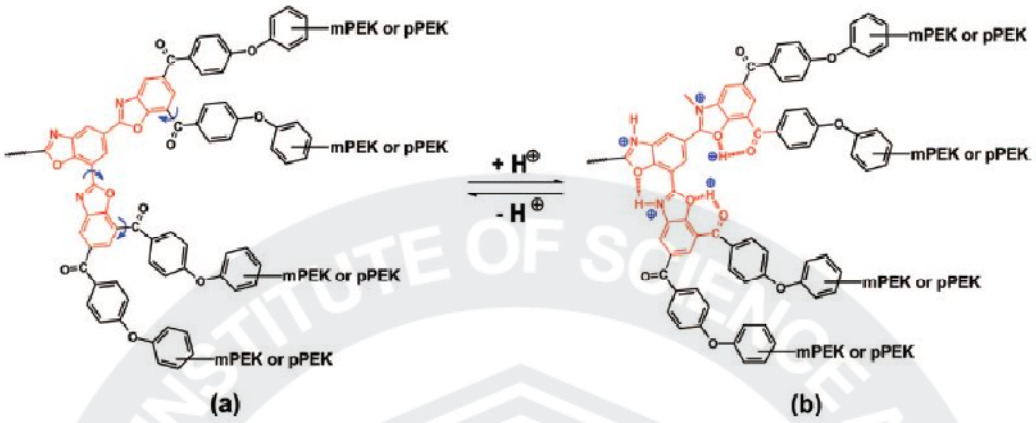

unchanged with respect to that of HPBO, but that in the near-visible region was red-shifted from 350 to 381 nm (Δ = 31 nm). However, in the NMP solution (Figure 4d), the near-visible absorption band of HPBO had practically vanished, while the near-UV absorption peak was slightly red-shifted from 281 to 288 nm (Δ = 7 nm).

In replacing *m*PEK with *p*PEK in the star block copolymer, we observed that the near-visible absorption band in MSA solution was red-shifted from 350 to 416 nm (Δ = 66 nm) in the visible region, while the near-UV absorption at 250 nm remained intact (Figure 4e). In switching from MSA to NMP, we found that the near-UV absorption was red-shifted from 281 to 291 nm (Δ = 10 nm). Similar to HPBO-*b*-*m*PEK in NMP, the near-visible band of HPBO at 352 nm had reduced to being a "shoulder" to the 291 nm band (Figure 4f).

In interpreting these results, we assume that the chromophoric component of the star block copolymers is the structural segments at the "interphase" where the peripheral COOH groups had made covalent linkages with the PEK chains. The assumption is reasonable because this is the location where the structural difference between HPBO and the star block copolymers could occur. The progressive shift of absorption maxima of HPBO, HPBO-*b*-*m*PEK, and HPBO-*b*-*p*PEK in both MSA and NMP solutions could be related to the geometry or conformation of HPBO's chromophoric component at the "inter phase" that is sensitive to protonation and, perhaps, other unknown processes as well. A noteworthy inference from these results is that numerous attachments of *m*PEK or *p*PEK to HPBO appear to promote greater electronic delocalization (i.e., an increase in the effective conjugation length or molecular planarity or both) in acidic MSA solution, while such mechanism is not accessible in basic NMP solution. We speculate that such mechanism is driven by the ability of MSA to protonate all lone-pair electrons and the consequential intramolecular hydrogen bonding leading to higher degree of coplanarity between the adjacent chromophoric benzoxazole units (see Scheme 7). Apparently, the para−para catenation of *p*PEK appears to be able to exert more bathochromic influence than the *m*PEK's meta−para catenation, judging from the wavelength shift between HPBO-*g*-*p*PEK (Δ = 56 nm) and HPBO-*g*-*m*PEK (Δ = 31 nm) of the HPBO absorption band at 350 nm.

Emission maxima of HPBO in MSA solution were in the blue region at 408 and 432 nm (Figure 5a). The peak intensity almost linearly decreased as concentration was increased due to an excimer quenching, which is favored by higher chromophore concentrations. The HPBO/NMP solution showed emission peak at 461 nm, which was 53 nm red-shifted as compared to that in MSA solution (Figure 5b). In conjunction with the results from UV−vis absorption study, the result also supports that the conformation of HPBO changes in different solvent systems (See Scheme 6). The shift should be attributable to the protonation to carboxylic acids and oxazole units on HPBO in strong acidic MSA. As in the case of MSA solution, NMP solution also displayed a decreasing trend in the emission intensity as the HPBO concentration was increased.

In the case of HPBO-*b*-*m*PEK, the emission peak in MSA solution was at 447 nm, which was red-shifted by 39 nm as compared to the HPBO/MSA solution (Figure 5c). The intensity was much less influenced by concentration variation and slightly decreased as the HPBO-*b*-*m*PEK concentration was increased. This was because the star block copolymer's chromophoric units were well shielded by the *m*PEK shell. The NMP solution of had an emission peak at 591 nm, which was 144 and 130 nm red-shifted as compared to the HPBO-*b*-*m*PEK/MSA solution and HPBO/NMP solution, respectively (Figure 5d). This indicates that the structure and properties of HPBO-*b*-*m*PEK's excited state are different from that of HPBO and also sensitive to solvent that is capable of engaging in specific interactions, e.g., acid−base equilibrium. It was noteworthy that the peak intensity drastically diminished as the star block copolymer's concentration was increased up to 0.7 mmol/L (Figure 5d, inset). But it reverted back to reach the highest intensity at 0.9 mM, and the result was reproducible. The origin of this behavior is presently unknown, but the result seems to imply that there is some kind of changeover in the polymer conformational dynamics in this specific concentration range.

The HPBO-*b*-*p*PEK/MSA solution displayed emission peak at 472 nm, which was 25 nm red-shifted as compared to that of HPBO-*b*-*m*PEK/MSA solution. The intensity also remained almost constant. Thus, similar to the results from the UV−vis absorption studies discussed above, the fluorescence results suggest that the conformation of the HPBO core would be somehow dependent on which type of PEK polymer was attached. Furthermore, if using its UV absorption behavior as a guide, this star block copolymer in NMP solution was expected to show more red shift in its fluorescence. However, as it turned out, the HPBO-*b*-*p*PEK/NMP solution displayed an emission maximum at 452 nm but with low intensity. This is because

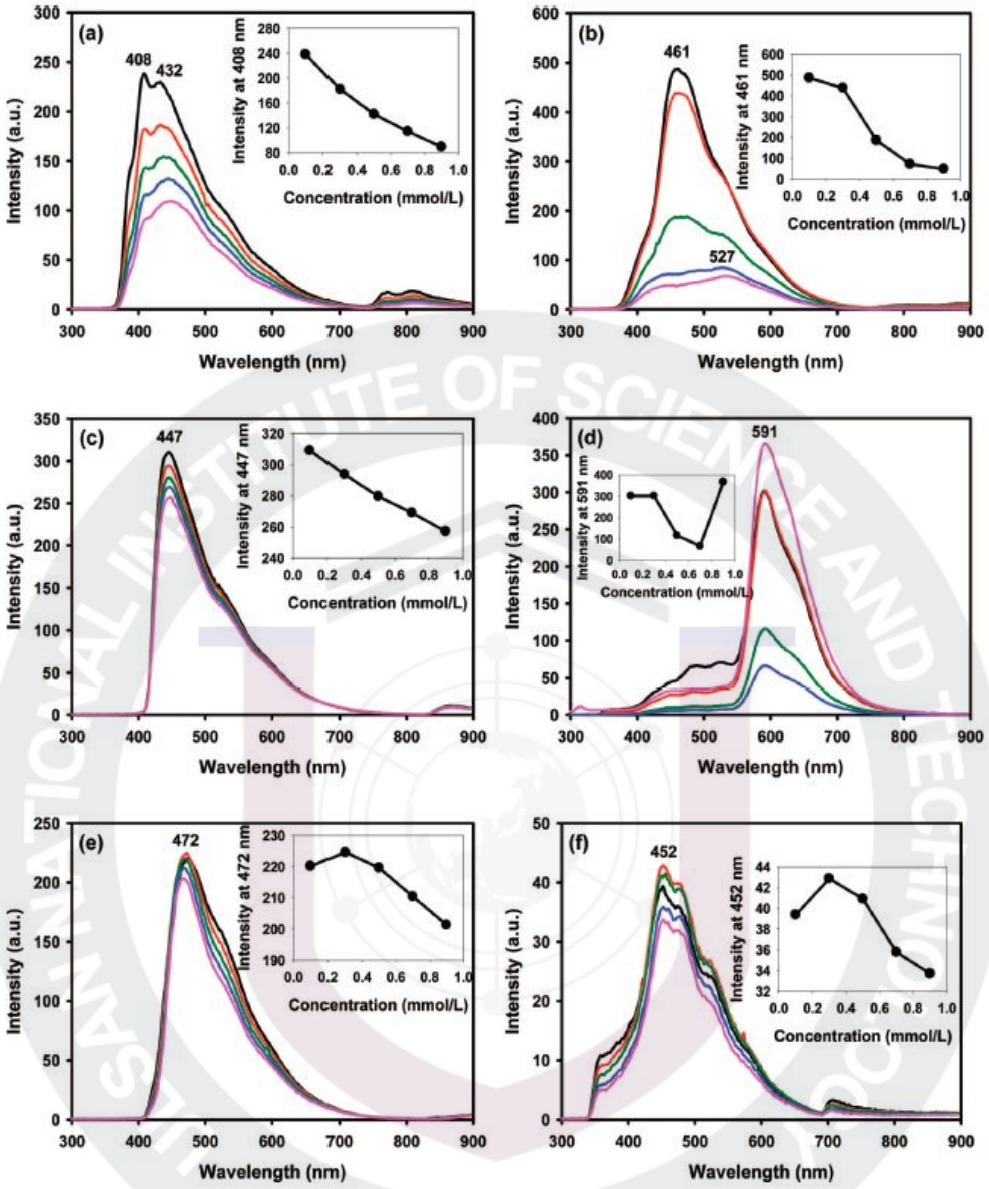

Figure 5. Fluorescence spectra of sample solutions: (a) HPBO in MSA; (b) HPBO in NMP; (c) HPBO-*g*-*m*PEK in MSA; (d) HPBO-*g*-*m*PEK in NMP; (e) HPBO-*g*-*p*PEK in MSA; (f) HPBO-*g*-*p*PEK in NMP.

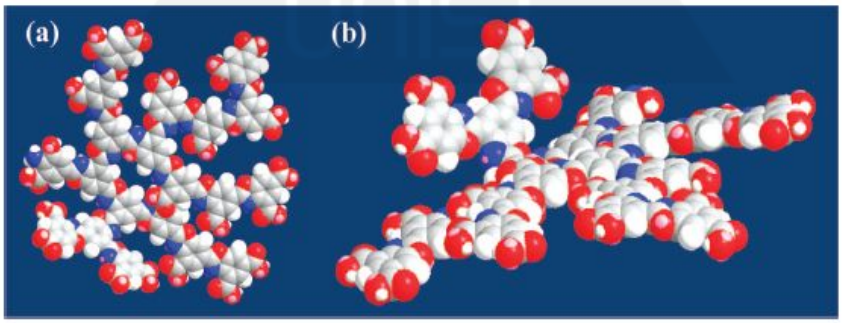

Figure 6. Energy-minimized space-filling structures of HPBO (CS Chem3D Ultra v8.0.3): (a) top view; (b) side view.

NMP is not a good solvent for semicrystalline *p*PEK.[18] Thus, the conformation of the star block copolymer must be in a greatly contracting mode in NMP, and thus, the HPBO's chromophoric units inside the block copolymers are being

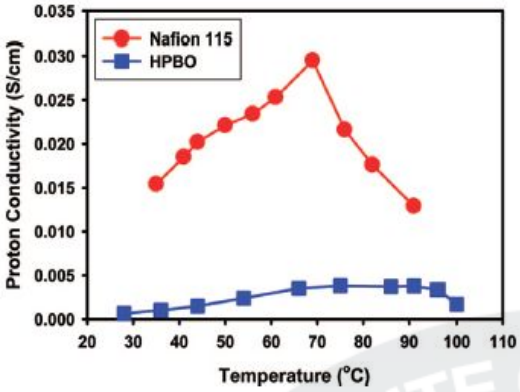

Figure 7. Proton conductivities of Nafion 115 and HPBO.

"squeezed" close to each other, promoting the intramolecular excimer quenching. In addition, the effective conjugation length/coplanarity of HPBO's chromophoric units in the block copolymer was also forced to be shorter than the chromophoric units in HPBO-*b*-*m*PEK.

On the basis of the results from the absorption and emission studies, it could be tentatively concluded that the protonation process in MSA significantly influences the excited state rather than the ground state of the chromophoric units located near the periphery of HPBO and at the "interphase" segment of the star block copolymers. However, while similar results with fluorescence Stokes shifts as a function of solvent polarity and the shielding effect of dendrimers[19] and dendrons[20] toward excimer quenching have been reported, the observed emission behaviors of our hyperbranched and star block systems are quite unique in a *strongly acidic* environment.

An energy-minimization computation study was conducted with a model HPBO molecule consisting of 20 repeating units. Although high molecular weight hyperbranched polymer is expected to have a globular architecture, an energy-minimized, space-filling molecular model shows that the structure of HPBO with 20 repeating units is quite planar (Figure 6). From this result, we could surmise that the degree of HPBO conjugation would be high enough to promote emitting light in the blue region as presented in the Figure 5.

Proton Conductivity of HPBO and Its Star Block Copolymers. Since there are numerous surface carboxylic acids present on the HPBO polymer, the proton conductivity was measured with two-point probe conductivity measurement at the relative humidity of 50% (Figure 7). For benchmarking, Nafion 115 was also evaluated under the same measuring conditions and found to display higher proton conductivity. However, the conductivity of Nafion 115 was dropping drastically when the temperature was raised above 70 °C. On the other hand, HPBO showed an initial value of 6.6×10^{-4} S/cm at 28 °C, which gradually increased as temperature was increased up to 90 °C before the decay started. Expectedly, the relatively lower proton conductivity of HPBO as compared to Nafion 115 could be explained in terms of their large acidity difference. The pK_a values of Nafion 115 and HPBO are ca. −6[21] and 4.2,[22] respectively. Thus, their pK_a difference is approximately ~10 to 11 orders of magnitude, but the difference in their proton conductivities is approximately an order of magnitude. It appears that in HPBO there is a nonlinear relationship between the acidity (at the molecular level) and proton conductivity (in the bulk state), and rather surprisingly at first, there is less temperature dependence in its proton conductivity. We suspect that the unique dendritic features of HPBO, namely (i) a large number of carboxylic acids per molecules and (ii) most of carboxylic acids would be present at the periphery of HPBO (see Figure 8b), may be the contributing factors. Further, since the dissociation of proton from carboxylic group is a function of temperature as opposed to the complete ionization of sulfonic group at room conditions (provided that enough water are present), it is reasonable to assume that the concentration of mobile protons in HPBO would increase with an increase in the surrounding temperature. Tentative explanations aside, this intriguing result has prompted us to further pursue a HPBO modified with sulfonic acid termini

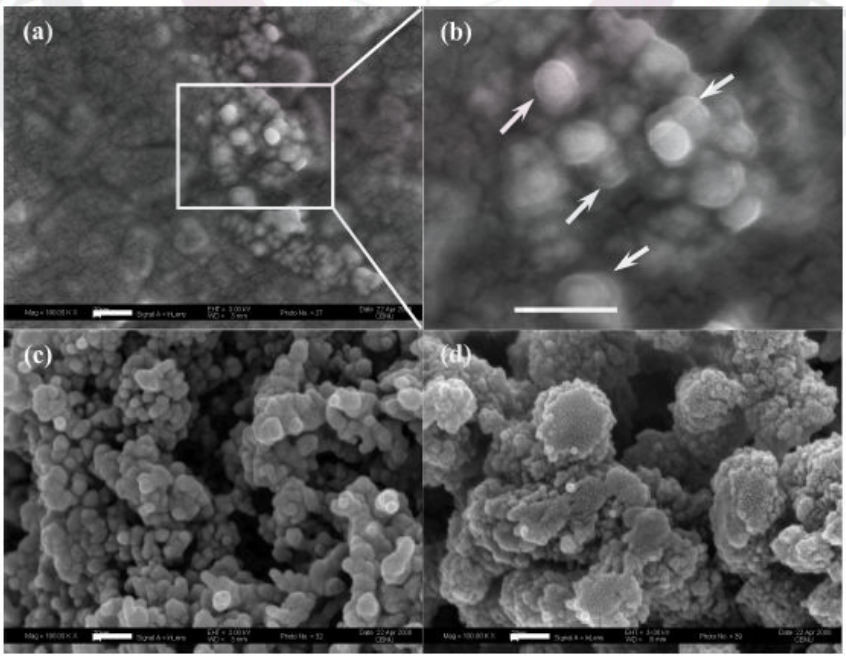

Figure 8. SEM images of samples: (a) HPBO (×100 000); (b) magnified image of (a); (c) HPBO-*g*-*m*PEK (×100 000); (d) HPBO-*g*-*p*PEK (×100 000). Scale bars are 100 nm.

to validate or refute our hypothesis. The synthesis and characterizations of such sulfonic acid-terminated HPBO are currently underway.

The proton conductivities of HPBO-*b*-*m*PEK and HPBO-*b*-*p*PEK were out of detection limit, since the number of carboxylic acids in copolymers was diluted by PEK units.

Scanning Electron Microscopy (SEM). The SEM images were obtained from powder samples. The morphology of HPBO appears to be made up of aggregating nanospheres (Figure 8a). Interestingly, these nanospheres could be discerned by two parts: a dense inner hard core is covered by fluffy outer shadow-like shell (Figure 8b, arrows). The diameters of the nanospheres are in the range of 10−40 nm. The inner hard part could be assigned to aromatic benzoxazole rings, and the fluffy outer shell could be mostly dominated by the carboxylic acids based on the fact that the electron density of inner aromatic benzoxazole rings is much higher than that of carboxylic acids. The SEM analysis visually supported the scenario in terms of the macromolecular architecture and surface chemistry at the molecular level to explain the higher than expected proton conductivity (see Figure 7) because of the relatively low acidity of the carboxylic acid and the observed optical behaviors of HPBO (see Figures 4 and 5).

The SEM image of HPBO-*b*-*m*PEK reveals that HPBO is well surrounded by *m*PEK (Figure 8c). The morphology is also dominated by the aggregations of nanospheres with diameter range of 10−40 nm. However, the interface between HPBO and *m*PEK could not be discerned since both are consisted of aromatic rings. The difference in the electron density between HPBO and *m*PEK may not be distinguishable. Thus, the morphology provides an indication that *m*PEK is grafted to the surface of HPBO. In the case of HPBO-*b*-*p*PEK (Figure 8d), the diameter dimension is much smaller than that of HPBO-*b*-*m*PEK apparently because *p*PEK is a semicrystalline polymer and, therefore, more compact. Overall, the particulate aggregates appear to be in much larger dimensions (>200 nm), while the individual particle dimension is 10−20 nm.

Conclusion

The AB_2 monomer, 5-amino-4-hydroxyisophthalic acid hydrochloride, was successfully synthesized and polymerized to afford high molecular weight hyperbranched polybenzoxazole (HPBO). The resultant HPBO was used as the core block for the subsequent synthesis of polyarm-star block copolymers. All the isolated polymers displayed polyelectrolyte behaviors in dilute solutions due to the presence of carboxylic acids on their peripheries. Specifically, since HPBO had the highest number of hydrophilic carboxylic acids per given weight, it clearly displayed stepwise weight-loss profile due to the bounded water and carboxylic acid decomposition. The UV−vis absorption behaviors for all samples with respect to the concentration were pseudo-linear dependence. However, the emission characteristics were significantly different between the HPBO parent polymer and the star block copolymers. While the emission intensity drastically decreased as the concentration of HPBO parent polymer was increased due to excimer quenching, the star-block copolymers were more or less unaffected by similar polymer concentration changes. This is apparently because in these star block copolymers the chromophoric units of the HPBO core were well protected from excimer quenching by their outer linear PEK shells in a good solvent. The unusual proton conductivity and emission behavior might have come from the morphology at the molecular level. The SEM image of HPBO showed that globular core−shell architecture of the HPBO in solid state. The high concentration of carboxylic acids on the surface of HPBO could be a reason why HPBO showed higher proton conductivity. While various hyperbranched polymers have been specifically synthesized for proton conductivity applications, as far as we know, the proton conductivities of these polymers are not based on carboxylic acid groups. Although the proton conductivity of our carboxylic acid-based hyperbranched polymer (HBPO) is still quite inferior, the observation that it is less temperature-dependent than Nafion provides some important insight for the design of improved high-temperature proton-conducting polymers.

Acknowledgment. We are grateful to Jeong Hee Lee (SEM) of Chungbuk National University and Dr. Yeong-Suk Choi (Proton Conductivity) of the Samsung Advanced Institute of Technology (SAIT) for obtaining data. This project was supported by funding from US Air Force Office of Scientific Research, Asian Office of Aerospace R&D (AFOSR-AOARD) and Korea Science and Engineering Foundation (R01-2007-000-10031-02).

Supporting Information Available: ^1H and ^{13}C NMR spectra of AB_2 monomer 4, 5-amino-4-hydroxyisophthalic acid hydrochloride (Figure S1). This material is available free of charge via the Internet at http://pubs.acs.org.

Note Added After ASAP Publication. This article was published ASAP on February 9, 2009. In the thirteenth paragraph of the Results and Discussion section, a value for Δ has been changed. The correct version was published on February 12, 2009.

References and Notes

(1) (a) Zhou, C.; Wang, S.; Zhuang, Q.; Han, Z. *Carbon* **2008**, *46*, 1232. (b) Liu, Z.; Wang, S.; Zhuang, Q.; Li, X.; Li, F.; Wu, P.; Han, Z. *Chem. Mater.* **2007**, *19*, 1164. (c) Wang, S.; Chen, Y.; Zhuang, Q.; Li, X.; Wu, P.; Han, Z. *Macromol. Chem. Phys.* **2006**, *207*, 2336. (d) Wang, S.; Wu, P.; Han, Z. *J. Mater. Sci.* **2004**, *39*, 2717. (e) Tan, S. C.; Bai, Z.; Sun, H.; Mark, J. E.; Arnold, F. E.; Lee, C. Y. C. *J. Mater. Sci.* **2003**, *38*, 4013. (f) Cerruti, P.; Maglio, G.; Palumbo, R.; Tortora, M. *Macromol. Chem. Phys.* **2002**, *203*, 484. (g) Tan, L.-S.; Simko, S. R.; Bai, S. J.; Vaia, R. A.; Taylor, B. E.; Houtz, M. D.; Alexander, M. D., Jr.; Spry, R. J. *J. Polym. Sci., Part B: Polym. Phys.* **2001**, *39*, 2539.

(2) Reviews on polybenzobisazoles: (a) So, Y.-H. *Polym. Int.* **2006**, *55*, 127. (b) Huang, W.; Yin, J. *Polym. Bull.* **2006**, *57*, 269. (b) Lane, R. A. *AMPTIAC Q.* **2005**, *9* (2), 3. (c) Hu, X.-D.; Jenkins, S. E.; Min, B. G.; Polk, M. B.; Kumar, S. *Macromol. Mater. Eng.* **2003**, *288*, 823. (d) Sikkema, D. J.; Northolt, M. G.; Pourdeyhimi, B. *MRS Bull.* **2003**, *28*, 579. (e) Komarova, L. G.; Rusanov, A. L. *Russ. Chem. Rev.* **2001**, *70*, 81. (f) Adams, W. W., Eby, R. K., McLemore, D. E., Eds.; *The Materials Science and Engineering of Rigid-Rod Polymers*; MRS Symp. Proc. Vol. 134; Materials Research Society: Pittsburg, PA, 1989. (h) Wolfe, J. F. In *Encyclopedia of Polymer Science and Technology*, 2nd ed.; Mark, H. F., Kroschmitz, J. I., Eds.; Wiley: New York, 1988; Vol. 11, pp 601−635.

(3) (a) Li, Q.; Jensen, J. O. *Membr. Technol.* **2008**, *2*, 61. (b) Li, J.; Yu, H. *J. Polym. Sci., Part A: Polym. Chem.* **2007**, *45*, 2273. (c) Li, J.; Lee, C. H.; Park, H. B.; Lee, Y. M. *Macromol. Res.* **2006**, *14*, 438. (c) Lee, C. H.; Jung, C. H.; Lee, Y. M.; Rhim, J. W.; Nam, S. Y. *Desalination* **2006**, *200*, 664. (e) Harrison, W. L.; Hickner, M. A.; Kim, Y. S.; McGrath, J. E. *Fuel Cells* **2005**, *5*, 201.

(4) Reviews on structural applications: (a) Young, R. J.; Eichhorn, S. J. *Polymer* **2007**, *48*, 2. (b) Chae, H. G.; Kumar, S. *J. Appl. Polym. Sci.* **2006**, *100*, 791. (c) Northolt, M. G.; den Decker, P.; Picken, S. J.; Baltussen, J. J. M.; Schlatmann, R. *Adv. Polym. Sci.* **2005**, *178*, 1. (d) So, Y.-H. *Prog. Polym. Sci.* **2000**, *25*, 137. (e) Schartel, B.; Wendorff, J. H. *Polym. Eng. Sci.* **1999**, *39*, 128.

(5) Reviews on opto-electronic applications of rigid-rod polymers: (a) Kraft, A.; Grimsdale, A. C.; Holmes, A. B. *Angew. Chem., Int. Ed.* **1998**, *37*, 402, and references therein. (b) Alam, M. M.; Jenekhe, S. A. *Chem. Mater.* **2002**, *14*, 4775, and references therein For specific examples of all-aromatic rigid-rod polymers for LED applications, see: (c) Kanbara, T.; Inoue, T.; Sugiyama, K.; Yamamoto, T. *Synth. Met.* **1995**, *71*, 2207. (d) Thelakkat, M.; Schmidt, H.-W. *Polym. Adv. Technol.* **1998**, *9*, 429. (e) Bettenhausen, J.; Greczmiel, M.; Jandke, M.; Strohriegl, P. *Synth. Met.* **1997**, *91*, 223.

(6) For general reviews on dendritic macromolecules, see: (a) Gao, C.; Yan, D. *Prog. Polym. Sci.* **2004**, *29*, 183. (b) Jikei, M.; Kakimoto, M. *Prog. Polym. Sci.* **2001**, *26*, 1233. (c) Kim, Y. H. *J. Polym. Sci., Part A: Polym. Chem.* **1998**, *36*, 1685. (d) Hult, A.; Johansson, M.; Malmström, E. *Adv. Polym. Sci.* **1999**, *143*, 1. (e) Inoue, K. *Prog.*

Polym. Sci. 2000, *25*, 453. (f) Voit, B. *J. Polym. Sci., Part A: Polym. Chem.* **2000**, *36*, 2505. (g) Hult, A.; Malmström, E.; Johansson, M. In *Polymeric Materials Encyclopedia*; Salamone, J., Ed.; CRC Press: Boca Raton, FL, 1996; Vol. 5 H-L, p 3171.

(7) Aromatic heterocyclic hyperbranched polymers: (a) Baek, J.-B.; Harris, F. W. *Macromolecules* **2005**, *38*, 297. (b) Baek, J.-B.; Harris, F. W. *Macromolecules* **2005**, *38*, 1131. (c) Baek, J.-B.; Tan, L.-S. *Macromolecules* **2006**, *39*, 2794. (d) Gong, Z.-H.; Leu, C.-M.; Wu, F.-I.; Shu, C.-F. *Macromolecules* **2000**, *33*, 8527.

(8) Baek, J.-B.; Simko, S. R.; Tan, L.-S. *Macromolecules* **2006**, *39*, 7959.

(9) (a) Baek, J.-B.; Tan, L.-S. *Polym. Prepr.* **2002**, *43* (1), 533. (b) Baek, J.-B.; Tan, L.-S. *Polym. Prepr.* **2002**, *43* (1), 514.

(10) Choi, J.-Y.; Tan, L.-S.; Baek, J.-B. *Macromolecules* **2006**, *39*, 9057.

(11) Baek, J.-B.; Tan, L.-S. *Polymer* **2003**, *44*, 4135.

(12) For general reviews on hyperbranched polymers: (a) Fréchet, J. M. J. *Science* **1994**, *263*, 1710–1715. (b) Majoral, J. P.; Caminade, A. M. *Chem. Rev.* **1999**, *99*, 845–880. (c) Matthews, O. A.; Shipway, A. N.; Stoddart, J. F. *Prog. Polym. Sci.* **1998**, *23*, 1–56. (d) Bochkarev, M. N.; Katkova, M. A. *Russ. Chem. Rev.* **1995**, *64*, 1035–1048. (e) Tomalia, D. A.; Hedstrand, D. M.; Wilson, L. R. In *Encyclopedia of Polymer Science & Engineering*, 2nd ed.; Wiley and Sons: New York, 1990; p 46. (f) Burchard, W. *Adv. Polym. Sci.* **1983**, *48*, 1–124. (g) Turner, S. R.; Voit, B. I.; Mourey, T. H. *Macromolecules* **1993**, *26*, 4617–4623.

(13) Krause, S. J.; Haddock, T. B.; Vezie, D. L.; Lenhert, P. G.; Hwang, W. F.; Price, G. E.; Helminiak, T. E.; O'Brien, J. F.; Adams, W. W. *Polymer* **1988**, *29*, 1354.

(14) (a) Yu, J.; Ree, M.; Shin, T. J.; Wang, X.; Cai, W.; Zhou, D.; Lee, K. W. *J. Polym. Sci., Part B: Polym. Phys.* **1999**, *37*, 2806. (b) Kim, S. I.; Pyo, S. M.; Ree, M. *Macromolecules* **1997**, *30*, 7890. (c) Dauengauer, S. A.; Shibaev, L. A.; Sazanov, Y. N.; Stepanov, N. G.; Bulina, T. M. *J. Therm. Anal.* **1987**, *32*, 807.

(15) Baek, J.-B.; Park, S. Y.; Price, G. E.; Lyons, C. B.; Tan, L.-S. *Polymer* **2005**, *46*, 1543.

(16) Wesolowski, M.; Konarski, T. *J. Therm. Anal. Calorim.* **1999**, *55*, 995–1002.

(17) (a) *Handbook of Conducting Polymer*; Skotheim, T. A., Ed.; Marcel Dekker: New York, 1986, Vol. 2. (b) Burroughes, J. H.; Bradley, D. D. C.; Brown, A. R.; Marks, R. N.; Mackay, K.; Reiend, R. H.; Burns, P. L.; Holmes, A. B. *Nature (London)* **1990**, *347*, 539. (c) Osaheni, J. A.; Jenekhe, S. A. *Macromolecules* **1993**, *26*, 4726. (d) Jenekhe, S. A.; Osaheni, J. A. *Science* **1994**, *265*, 765.

(18) Bishop, M. T.; Karasz, F. E.; Russo, P. S.; Langley, K. H. *Macromolecules* **1985**, *18*, 86.

(19) Ceroni, P.; Bergamini, G.; Marchioni, F.; Balzani, V. *Prog. Polym. Sci.* **2005**, *30*, 453, and references therein.

(20) Wu, C.-W.; Sung, H.-H.; Lin, H.-C. *J. Polym. Sci., Part A: Polym. Chem.* **2006**, *44*, 6765, and references therein.

(21) (a) Kreuer, K. D. *J. Membr. Sci.* **2001**, *185*, 29. (b) Pathapati, P. R.; Xue, X.; Tang, J. *Renewable* **2004**, *30*, 1. (c) Ryder, A. G.; Power, S.; Glynn, T. *J. Appl. Spectrosc.* **2003**, *57*, 73.

(22) pK_a = 4.19 (25 °C). *The Merck Index*, 14th ed.; Merck & Co.: Whitehouse Station, NJ, 2006; p 180.

MA802401V

Acknowledgements

First and foremost I offer my sincerest gratitude to my supervisor, Dr. Jong-Beom Baek, who has supported me throughout my thesis with his patience and knowledge whilst allowing me the room to work in my own way. I attribute the level of my Masters degree to his encouragement and effort and without him this thesis, too, would not have been completed or written. One simply could not wish for a better or friendlier supervisor. And Professor Hyun-Kon Song and Byeong-su Kim have offered much advice and insight throughout my work.

In my daily work I have been blessed with a friendly and cheerful group of fellow students. Firstly, Ph.D. Dong-Wook Jang and master In-Yup Jeon, as well as favorable personality, has provided good arguments about purification process. Sang-Wook, Ji-Ye and Hyun-Jung has been a companiable classmate for about three years as well as a colleague and possesses the greatest quality in a friendship. Thanks also to my junior and friend: Gyoung-Su, Seo-Yoon, Yeon-ran, Gyoung-Ju, Ki-Hwan, Jeong-Su, Dong-Wook, Jae-Myeong, Heung-Seok, Young-Hun, Min-Ho, Jong-Ki and Ki-Gwang. I like to say if you work hard you will achieve everything you want! And life in UNIST with you has unforgettable memories for us.

Last but not the least, the one above all of us, the omnipresent God, for answering my prayers for giving me the strength to plod on despite my constitution wanting to give up and throw in the towel. Finally, I thank my parents for supporting me throughout all my studies at UNIST, Let me take this opportunity to say a word, I always love my family and thank you so much!